Investigations on the dynamics of excess electrons in pyrrolidinium bistriflimide and diacyanoamide RTILs

A THESIS

SUBMITTED TO THE FACULTY OF THE GRADUATE SCHOOL

OF THE UNIVERSITY OF MINNESOTA

BY

Francesc Molins i Domenech

IN PARTIAL FULFILLMENT OF THE REQUIREMENTS

FOR THE DEGREE OF

PhD

David A Blank

May, 2015

Abbreviations Used:

AC	Autocorrelation
BBO	β Barium borate.
BDE	Bond dissociation energy
Bistriflimide	Bis(trifluoromethane)sulfonimide
CTTS	Charge transfer to solvent
ΔOD	Change in optical density
DOS	Density of states
DQ	Duroquinone
DSS	Dynamic Stokes' shift
EPR	Electron paramagnetic resonance
HOMO	Highest occupied molecular orbital
FH	Fourth harmonic
FWHM	Full width at half max (of a gaussian function)
IL	Ionic liquid.
IRF	Instrument response function
LUMO	Lowest unoccupied molecular orbital
MD	Molecular Dynamics
QY	Quantum yield
SFG	Sum frequency generation.
RMSD	Root mean square deviation
RTIL	Room temperature ionic liquid
SHG	Second harmonic generation.
SH	Second harmonic
SVD	Singular value decomposition
TA	Transient absorption
TH	Third harmonic
UV	Ultraviolet

$[\mathbf{Py}^+_{1,3}][\mathbf{NTf}^-_2]$	1-methyl-1-propyl-pyrrolidinium bis(trifluoromethylsulfonyl)amide
$[\mathbf{Py}^+_{1,4}][\mathbf{NTf}^-_2]$	1-methyl-1-butyl-pyrrolidinium bis(trifluoromethylsulfonyl)amide
$[\mathbf{Py}^+_{1,6}][\mathbf{NTf}^-_2]$	1-methyl-1-hexyl-pyrrolidinium bis(trifluoromethylsulfonyl)amide
$[\mathbf{Py}^+_{1,10}][\mathbf{NTf}^-_2]$	1-methyl-1-decyl-pyrrolidinium bis(trifluoromethylsulfonyl)amide
$[\mathbf{Py}^+_{1,4}][\mathbf{N(CN)}^-_2]$	1-methyl-1-butyl-pyrrolidinium dicyanoamide

Acknowledgements

A number of people have made this work possible in different ways. I am indebted to Dr Andrew Healy, from whom I have learned and relearned both the basics and all sorts of tricks to obtain a stable laser. He also machined the first aluminum holder for the spin cell, which allowed the experiments to be performed earlier than otherwise. Help of all kinds I have also gotten from the other group members: Thanks are due to Phillip Goff for the help troubleshooting all kinds of problems and for taking such good care of the glove box. To Dr Tom Pundsack for all the indispensable help with LabView and in particular with setting up the InGaAs array detector. Thank you to Dr Benjamin Caplin for all I have learned from conversations with him during the little time we have overlapped. Thank you to Dr Toni Sanchez for his enthusiasm and the help setting up the probe line.

I am very thankful to our collaborators Gary Baker and James Wishart for supplying us samples of $[Py^{+}_{1,3}][NTf^{-}_{2}]$, $[Py^{+}_{1,6}][NTf^{-}_{2}]$, $[Py^{+}_{1,10}][NTf^{-}_{2}]$ and $[Py^{+}_{1,4}][N(CN)^{-}_{2}]$.

I would like to thank Prof. Sanford Lipsky for his attention and interest, scientific and personal, and for his advice, which I almost always failed to take. Finally, greatly indebted I am to Prof. David Blank, for all I have learned from him, for his patience, help and great generosity. Thank you for everything.

Moltes gràcies al meu germà Domènec i als meus pares, Carme i Josep Maria, per tot el suport i llibertat que m'heu donat al llarg dels anys. Moltes gràcies al Toni per haver-me introduït a en Burriel i a en March, que em van fer interessar per què passa dins de les coses. I un record per a l'àvia Teresa, que segur que se n'alegraria per mi, i als avis Carme i Ciscu que també se n'alegraran.

Ganz besonders danke ich auch Katrin Grau. Ohne ihre Hilfe und Freunschaft wäre alles viel schwieriger gewesen und es hätte sich auch weniger gelohnt.

Dedication

"Frederick, was ist die Natur?"

"Nichts leichter als das," antwortete Frederick, "komm mit..."

Abstract

Ionic liquids (IL), or salts that are liquid near room temperature, are finding an ever increasing range of applications. Many of these involve environments where redox and photochemical processes play a key role, such as in dye sensitized solar cells, or the treatment of spent nuclear fuel. Yet little is still known about the details of the fast processes and fate of excess electrons in these materials, and this work attempts to further our understanding of such dynamics in this diverse class of substances.

After the Introduction and Experimental sections, the first chapter reports our first photodetachment experiments in the $[Py^+_{1,4}][NTf^-_2]$ ionic liquid. Although we later found out that upon further purification this IL does not absorb at the excitation energy that we used, 4.67 eV, and thus the signals we observed could not be due to electrons ejected from the liquid itself but must have originated from some impurity, the transient absorptions and their quenching with an electron scavenger still offer valuable information and is thus presented.

Next, the same kind of experiment but at a higher energy was performed on a homologous series of the same type of liquids: $[Py^+_{1,3}][NTf^-_2]$, $[Py^+_{1,6}][NTf^-_2]$ and $[Py^+_{1,10}][NTf^-_2]$. Purification of these liquids has shown that the onset of absorption is above ~ 5.8 eV, and we have had to use 6.2 eV laser pulses. Following absorption of one photon, the characteristic near-IR transients of electrons in these liquids appear and their ultrafast

relaxation is followed. Evidence is found that the NTf_2^- anion undergoes an ultrafast dissociative electron attachment reaction, as it has been predicted theoretically. Ultrafast quenching in the presence of electron scavengers indicates the existence of early very delocalized states of the ejected electron. A competition between electron capture by the NTf_2^- anions on the one hand, and solvation in some kind of cavity on the other, is proposed as a way to explain the observations.

The injection of electrons into the liquid from another electron donor, I^-, is then investigated. It is found that within the accuracy of our experiments the cleavage of the NTf_2^- anions is suppressed, and that a completely different electron cooling pathway to the same final solvation state is followed. Mechanisms to explain these findings are discussed.

Finally, a set of results performed on a liquid with an anion resistant to reductive cleavage, $[Py_{1,4}^+][N(CN)_2^-]$, are presented which raise interesting questions on the interpretation of the results in the $[Py_{1,x}^+][NTf_2^-]$ liquids.

Each of the series of experiments mentioned above have also been performed on $[Py_{1,4}^+][NTf_2^-]$, but the results were not in agreement with the trends shown by the other members of the series. We have reasons to believe that the $[Py_{1,4}^+][NTf_2^-]$ liquid contained some impurities that our purification method could not eliminate. Because of this, the results for this liquid are presented in the appendices.

Contents

List of Tables

List of Figures

Chapter 1

Introduction: Excess electrons in Ionic Liquids

We will begin by briefly introducing some relevant aspects regarding the general properties, structure and dynamics of Ionic Liquids which will be used throughout this work. After that, we will review with some more attention the work already done by other groups on excess electrons in several Ionic Liquids, the conclusions which can be drawn from their results, and the many questions that remain unanswered.

1.1 General Properties of Ionic Liquids

Ionic Liquids are liquids whose constituents are ions. Yet the term is limited in its use to those that are fluid at or near room temperature, so that the molten simple

inorganic salts are excluded from this definition. To put more emphasis on this idea, they are often also referred to as *Room Temperature Ionic Liquids* (RTILs), and we will use both expressions interchangeably.

The history of ionic liquids dates back to late 1880's [142], but their physical properties did not begin to be extensively investigated until the early 1910's, with Paul Walden's work on ethylammonium nitrate, (mp 13 °C) [135]. Since then, and especially during the last 15 years, RTILs have found an already enormous and still growing array of chemical and industrial applications, such as phase transfer catalysts, extraction agents, green solvents in industrial processes, supercapacitors, nuclear waste processing, solvents for dye-sensitized solar cells or coolants in nuclear plants amongst others. [9,20,30,31,36,43,50,63,77,87,96,98,123,124,127,140,141,144,150]This expanding interest is shown, for example, in the number of publications that include the term "ionic liquid" in its title each year, as shown in Figure 1.1.

The usefulness of these liquids in such diverse areas is mostly due to their negligible vapor pressures up to temperatures of hundreds of Celsius (ranging in the tens to hundreds of pPa), combined with the great tunability of their physico-chemical characteristics that the modification of the constituent ions allows. In contrast to the broad applicability of these liquids, a detailed understanding of their physical properties and how these relate to their molecular composition, is much more limited, although this situation has begun to change during the last ten years, when an interest in the chemical physics of these liquids has surged.

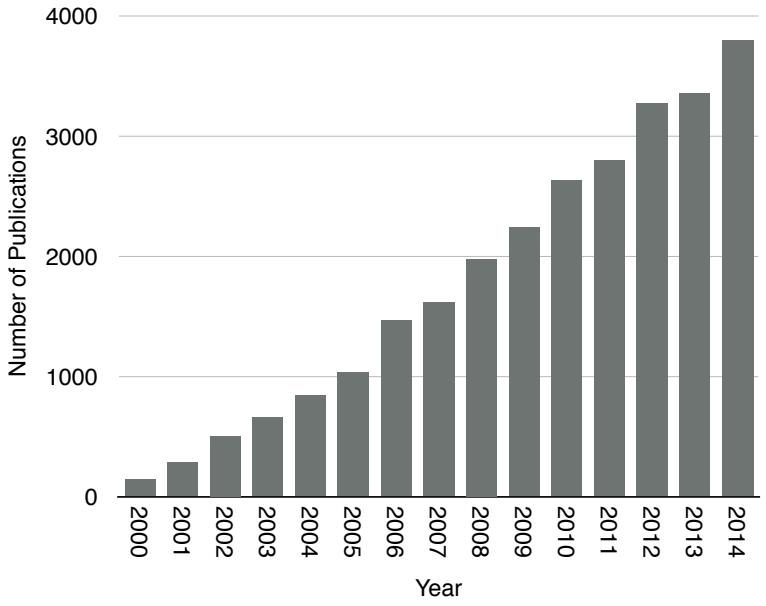

Figure 1.1: Evolution of the number of publications including the term "ionic liquid" in their title, over the last 15 years. Source: Web of Science.

In order for an ionic material to be fluid at room temperature, the electrostatic attraction between its positive and negative ions as well as the ability of these to pack efficiently into a crystal needs to be diminished. The Coulomb attraction is typically limited by the use of cations that are made effectively large by the addition of bulky substituents, as well as its delocalization in aromatic systems. A prototypical example of this is the alkyl substituted imidazolium cation. And on the other hand, anions are used in which the negative charge is very much delocalized over electron withdrawing groups, the hexafluorophosphate (PF_6^-) or the bistriflimide ($(CF_3SO)_2N^-$) anions being typical in this regard, although RTILs also exist with simple halide anions. Further, the ability of the ions to pack efficiently is hindered by the relative size of both ions as well

as their structural asymmetry. Besides, the same groups (typically relatively large alkyl chains) that make the cations large, provide conformational flexibility that entropically favors the liquid state. [75]

	Value (at 298 K)	
Vapor pressure	100 pPa	[97]
Electrochemical Window	-2 to 2.5 V (vs. SCE)	[98]
Electrical Conductivity	144 mS m^{-1}	[62]
Viscosity	270 cP	[1]
Dielectric Constant	11.4	[134]
n_D	1.4094	[151]

Table 1.1: Values for relevant properties of the common ionic liquid $[Im_{14}^+]$ $[PF_6^-]$

From such a characterization of ILs it must follow that there potentially exist a very large number of such liquids[1] , and that by tuning the composition of the two ions this set of materials can exhibit a very broad spectrum of physical and chemical properties. As a class, however, ILs are generally characterized by low flammability, extremely low vapor pressures, a very large range of temperature under which they remain liquid, moderate solvating power but which can be broadly tuned by design (thus for example, there exist both strongly hydrophobic ILs as well as strongly hydrophylic ILs. [8])

In order that the general reader may have an idea of the properties of a typical RTIL, Table 1.1 gives some relevant physical properties N,N'-butylmethylimidazolium hexafluorophosphate, $[Im_{14}^+]$ $[PF_6^-]$.

Many of the fields of application of RTILs that we have mentioned above, have radiolytic, red-ox, and photolytic processes at its heart, and thus provide motivation

[1] Combining all pairs of cations and anions currently used in ILs, one obtains a number of 10^6 possible binary liquids. This compares to the roughly 10^3 organic solvents [98]

to better understand ionization processes and the subsequent dynamics and reactivity associated with injected or detached electrons.

1.2 The Structure of RTILs

The question of the structure of the liquid phase of RTILs has been a subject of vigorous activity during the last decade, with plenty of experimental reports [7,12,18,18, 41,44,48,49,78,104,109,128,130,131,147], computational, [4,16,17,22,33,65,78,82,109, 122,132,136,137] and several good reviews. [24,25,48,68,72,82,139] Additionally, some special issues have recently been devoted to the chemical physics of ILs [39,58,101].

The main structural characteristics that differentiate ILs from common (molecular) liquids is the presence of *structuring*. That is, the presence of different types and ranges of spatial correlations in the arrangement of the constituent ions. One such type of organization is *charge ordering*. In common with molten simple inorganic salts, the radial distribution functions of ILs, computed from X-ray and neutron scattering experiments [32,41,49] as well as from simulations [47,72,111], show a strong association of each ion with those of opposite charge, albeit with somewhat less sharp features, accounted for by the fluxionality imparted by the alkyl substituents on the cations.

Another kind of structuring that has been reported in several aliphatic RTILs is the presence of domains of *interdigitation* of the alkyl chains on the cations. For example, Triolo *et al.* have suggested that their X-ray scattering measurements on a series

of alkyl-methylpiperidinium bistriflimides can be explained in terms of regions of interdigitating alkyl chains that have sizes of around 10 $\mathring{A}$, when alkyl = pentyl, hexyl, heptyl. [129] Similarly Pott *et al.* have suggested the presence of a smectic A phase in alkyl-trimethylammonium bistriflimides. [99]

A different kind of structuring exhibited by some RTILs is often called *Polarity Alternation*, and it refers to the formation of segregated aliphatic and ionic domains. That is, domains rich in the (large) alkyl chains usually found on the cations, separated from regions rich in both the more purely cationic and anionic parts of the constituent ions. The existence of this kind of structuring is supported by numerous X-ray and neutron diffraction measurements, [44, 65, 66, 78, 99, 110, 147], NMR srudies [88] as well as molecular dynamics simulations. [4, 23, 33, 54, 64, 85, 132]. Although there remains some controversy about the interpretation of the scattering experiments on some of the liquids, it is now broadly accepted that in several IL whose anions contain long alkyl chains, regions rich in the charged parts of the constitutent ions and regions rich in the neutral (and usually aliphatic) parts of the ions, segregate from each other forming nano-domains of differently polar environment.

Most relevant to the ILs that we have studied, is the experimental work by the Castner group, who have performed Small Angle X-Ray Scattering on a series of $[Py^{+}_{1,x}][NTf^{-}_{2}]$ liquids, where the subscript x specifies the length of a n-alkyl chain and equals 3 ,4, 5, 6, 7, 8 and 10. [66, 110] Staring at x = 7 a peak at a q ≈ 0.4 $\mathring{A}^{-1}$ that grows as x

increases is interpreted with the aid of the MD simulations as a evidence for the existence of polarity alternation in these liquids, and consequently, the lack thereof when the n-alkyl chain is shorter (x = 3, 4, 5), the threshold being at x=6. These experimental results have been reproduced by MD simulations by the Margulis group, and the interpretation peaks at low values of q as indication of the segregation of ionic vs. aliphatic groups is also brought about by their analysis. On the other hand, in contrast to the pyrrolidinium bistriflimide ILs just described, MD simulations have suggested that in imidazolium bistriflimides, polarity alternation starts playing a role starting at x = 4. [23]

A somewhat controversial aspect regarding the structure of ILs, is the presence of cavities, that is of significant empty spaces due to the poor packing of the constituent ions. This possibility has been suggested by the very small partial molar volume of CO_2 dissolved in $[Im_{14}^+]$ $[PF_6^-]$ as compared to common organic solvents. [21] However MD simulations of the same IL [56], showed that the probability of pre-existent cavities with radii equivalent to even the Van der Waals radius of a C atom (ca. 1.5 $\mathring{A}$) is vanishingly small, although smaller cavities with radii up to approx. 1 $\mathring{A}$ are not as rare (eg, they find: $\sim$1.5 cavities of 0.4 $\mathring{A}$ radius per ion pair; $\sim$0.1 cavities of 1 $\mathring{A}$ per ion pair). The authors find however, that small angular rearrangements of the anions which do not affect the cation-anion radial distribution function allows the CO_2 to be incorporated, mostly interacting with the quadrupole moment of the PF_6^- aninon. That is, there are no pre-existent cavities in this liquid ready to accommodate a CO_2 molecule, but plenty

of smaller ones that can be combined into a large enough one by means of small angular rearrangement of the anions with respect to the cations.

1.3 Solvation Dynamics in RTILs

We should perhaps emphasize that given the multitude of kinds of ILs that can be designed by choice of cation and anion and choice of substituent groups -especially in the cation-, one can hardly speak of a solvation dynamics truly characteristic of the of ILs. We will here introduce several aspects that we will use in later on, preferentially considering systems that are more relevant to ours, that is, the pyrrolidinium bistriflimides.

A fundamental aspect to take into account when considering the solvation dynamics in ILs is that of *dynamic heterogeneity*. In a fluid with a heterogeneity of environments, it is expected that the same transformation occurring in the different environments will have different energetics and constraints imposed on it, and as a result it will exhibit different lifetimes in the different "pockets". This will be so, however, only if the lifetime of the transformation considered is faster than the inter-conversion of the (meta-stable) environment pockets. When such is the case and a transformation is monitored, one measures the ensemble average of time constants over the probed volume and this results in dispersive kinetics, ie exhibiting non-exponential behavior. This phenomenon has long been known and well studied in super-cooled liquids, and good reviews are available [34, 37, 100]. Dynamic heterogeneity has also been detected

and measured in ILs, [59, 60, 83, 93, 106–108], as well as predicted by means of MD simulations [5, 54, 55]. As an illustrative example, the Maroncelli group has measured the dependence of the lifetime and emission spectrum on the excitation wavelength of DMN[2] in the RTIL [$NMe_2Pr^iPr^+$] [NTf_2^-]. [59] DMN has a fluorescence lifetime of about 8 ps, which is much faster than much of the solvation response of the IL used (after 10 ps about 50 % of the solvation response has not yet occurred).

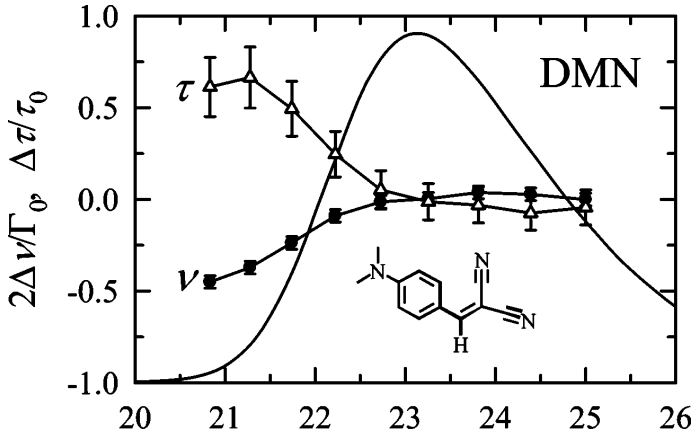

Figure 1.2: Fluorescence of DMN at different excitation wavelengths. The solid line shows the normalized absorption spectrum. The triangles, show the fluorescence lifetime as a function of excitation wavelength relative to the lifetime when exciting at the average wavelength of the absorption band. The solid circles show the first moment of the emission band relative to that when excited at the average wavelength of absorption, analogously to the lifetimes. Figure adapted with permission from reference [59]. Copyright 2007, American Chemical Society.

Figure 1.2, shows how the lifetime of emission as well as the position of the emission of DMN in [$NMe_2Pr^iPr^+$] [NTf_2^-] (see Figure caption for details) is dependent on the excitation wavelength. These results can be explained if one imagines that the different

[2] DMN refers to p-(dimethylamino)benzylidenemalonitrile, whose structure is shown in Figure 1.2

excitation wavelengths excite different sub-populations that have different environments. Because the response of the IL to the sudden dipole change of the solute is significantly slower than the emission from the dye, the different sub-populations emit from still different environments and thus with different lifetimes and frequencies.

A typical characteristic of the solvation dynamics of RTILs is its highly bi-modal character, with a relatively large amplitude sub-ps component followed by much a slower dispersive component with time-averaged lifetimes from the hundreds to thousands of ps for common ILs, which is similar to the dynamics observed in super-cooled liquids and glasses. In comparison, solvation dynamics in common organic solvents such as CH_3CN are also biphasic but the complete dynamics take on the order of a few ps. [102]

Experimental studies on the solvation dynamics in ILs have focused on the study of Dynamic Stokes shifts, as the work by Maroncelli described above, that is, the spectral evolution of the fluorescence as a function of time after the excitation. These studies are the more relevant, because it appears that the response of the solvent to the change of electronic distribution brought about by the excitation of the dye is relatively independent of the specific dye.

In one of the most recent and exhaustive investigations of dynamic Stoke shifts in RTILs [152], the emission spectrum from the coumarin dye C153 was followed from 50 fs to 20 ns after the excitation in a series of ILs. In the two types of the ILs investigated, imidazolium and pyrrolidinium bistriflimides, the dynamics were highly biphasic. For the pyrrolidinium ILs, the τ's of the fast component ranged from 0.4 ps for $[Py^{+}_{1,3}]$ to 1.1

ps for $[Py^+_{1,10}]$ and the τ's for the slow component ranged from 290 ps for $[Py^+_{1,3}]$ to 1500 ps for$[Py^+_{1,10}]$. Very interestingly, the fast τ for each liquid correlated with the reduced mass of Cation-Anion pair, thus suggesting an impulsive translational response, whereas the slower τ correlated the viscosity of the IL, thus suggesting diffusive rearrangement. These results are in agreement with molecular dynamics simulations of model systems which show that the sub-ps component of solvation is due to small amplitude, inertial, collective, translational motions of ions in the first solvation shell, and involving only small amounts of rotational motions. [70, 71, 103, 114, 115] Given the weight that these inertial sub-ps components contribute to the solvation response of the IL (values from 20 % to 40 % are typical for imidazolium and pyrrolidinium ILs), it appears that minor translations of the first shell of ions around the perturbed solute are enough in order to provide much of the necessary rearrangement to solvate the new dipole moment of the solute. On the other hand, the slower component is found in MD simulations to correspond to larger scale collective relaxation of a diffusive character. [114]

Relevant to our problem is also the work of Castner and Shirota, who have reported the optical Heterodyne Detected Raman Induced Kerr Effect Spectroscopy measurements on a series of $[Py^+_{1,x}]$ $[NTf^-_2]$, $[Br^-]$ and $[N(CN)^-_2]$ ILs. [116] The sub-ps relaxation that they observe are almost identical for all of the bistriflimide ILs and is dominated by beats corresponding to intramolecular vibrations of the NTf^-_2 anion. Beyond 1 ps the dynamics of all of the NTf^-_2 ILs are also similar and shows clearly non-exponential kinetics with reasonable fits obtained using 3 exponentials. τ_1 and τ_2 are very similar for these

liquids, with values of ∼2 ps and ∼20 ps, respectively. τ_3, ranging from 160 ps to 600 ps, does differ for the 3 liquids and agrees well with the (diffusive) Sotkes-Einstein-Debey reorientational dynamics model, especially when the volume of the diffuser is taken to be the sum of anion and cation volumes. The involvement of both the cation and anion in the diffusional part of the relaxation is also born out by MD simulations [73,85]. The spectrum corresponding these slower motions did not allow the authors to identify their nature, although they are supposed to be libration-like.

To summarize, we have seen that solvation dynamics in this class of RTILs are markedly dispersive, involving time scales from tens of fs to tens of ns, and resemble those of glasses. Excitation wavelength dependent time resolved fluorescence provides good evidence for the existence of dynamically different environments in the liquid. Beside the breadth of the relaxation time scales, an important mechanistic difference in dipolar solvation between RTILs and common molecular liquids, is the involvement of translational degrees of freedom that can account for an important part of the response on the sub-ps regime.

1.4 Excess electrons in RTILs

Here we review the current knowledge on the nature of excess electrons in RTILs. We do not however consider those ILs whose cations (such as imidazolium and pyridinium) rapidly attach the excess electron since in those liquids the dynamics are dominated by the chemistry of the reduced species, [117, 119, 120, 125] in which we are less interested.

Thus we limit ourselves to the behavior of excess electrons in ILs with *aliphatic* cations, of which the most investigated have been several tertiary ammonium, pyrrolidinium and phosphonium salts.

Excess electrons were first indirectly detected in ILs by means of Pulse Radiolysis studies of ILs with several electron scavengers combined with identification of the resulting reduced scavenger species [2, 14, 15, 45, 46, 84]. Shortly afterwards, they were spectrally characterized by Neta and Wishart, also radiolytically, in a tetraalkylammonium bistriflimide IL. [146]

In ILs without active functional groups, such us those that can form hydrogen bonds (eg. hydroxy groups and protonated amine cations), or those that can attach the solvated electron (eg. ILs with pyridinium and imidazolium cations), the spectral signature of the excess electron is a broad absorption band peaking in the near-IR, typically between 1100 nm and 1400 nm [67,125,145,146]. The molar absorptivity of the fully relaxed excess electron in these aliphatic ILs appears to be very similar to that in common molecular solvents such as water, having values close to 20000 M^{-1} cm^{-1} [11, 67, 146]. The lifetime of the excess electrons generated radiolytically in these ILs is of the order of a few hundreds of ns [74, 125, 145, 146], although only a limited meaning can be given these lifetimes because the purification of these ILs is challenging, and only lower bounds to their purity can be given.

These near-IR transients are affected by the addition of electron scavengers. The decrease of this TA at varying concentrations of scavenger, and in some cases, the

corresponding rise of the known spectral signature of the reduced form of the scavenger, provide very strong evidence that the near-IR TA is due to the excess electron. Further evidence for the solvated electron being responsible for the near-IR TA, comes from electron paramagnetic resonance (EPR) studies if irradiated cold IL glasses. Thus, Feldman and coworkers have found that irradiated glassy $[Py^{+}_{1,4}][NTf^{-}_{2}]$ exhibits a sharp singlet, compatible with a trapped electron, which is bleached when exposed to light with wavelengths above 600 nm. [105]

There have been some preliminary attempts to tackle the question of the origin of the broadness of the near-IR absorption of the excess electron. For example, Takahashi *et al.* used UV flash-photolysis to photodetach an electron from I^{-} in $[N^{+}_{1113}]$ $[NTf^{-}_{2}]$, and 200 ns after the UV pulse the sample was exposed to a 532 nm pulse. The spectral bleach in the TA induced by this last pulse was found to strongly depend on the wavelength between 500 nm and 1000 nm, indicating that the TA is at least partially inhomogeneously broadened, and thus providing evidence that excess electrons in this IL reside in a distribution of different environments. [126]

One of the most enlightening studies to date on the dynamics of excess electrons in pyrrolidinium RTILs, is a pulse radiolysis study on neat $[Py^{+}_{1,4}][NTf^{-}_{2}]$ by Wishart and coworkers, with a time resolution of *ca.* 15 ps [145]. Figure 1.3 shows the induced broad transient absorption between 600 nm and 1600 nm that undergoes a blue shift with an average time constant of 120 ps, the TA peak converging to a wavelength about 1050 nm. A singular value decomposition allowed to reconstruct the full spectral evolution

using only two spectral components, one peaking at around 1000 nm and attributed to a final sate of solvation of the electron, and another one peaking beyond 1500 nm, whose decay in amplitude renders the blue shift. The fact that their earliest data at ∼15 ps time delay, already contains a weight of *70* % for the final solvated electron component, indicates that a great deal of reorganization has occurred within these first 15 ps.

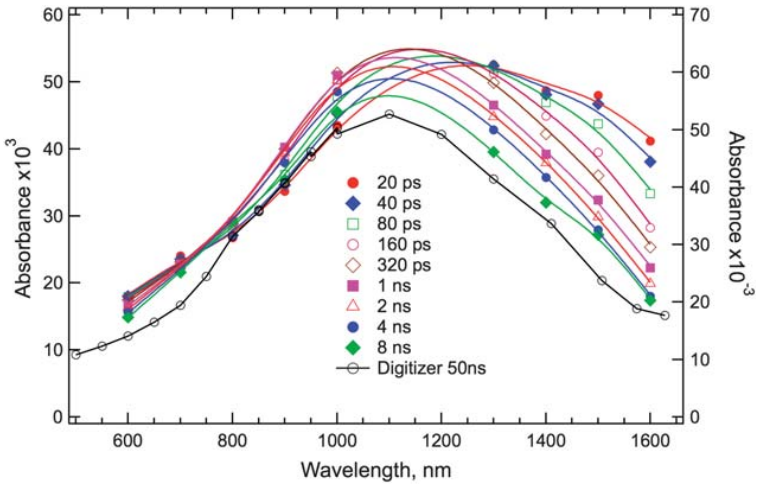

Figure 1.3: Time evolution of the reconstructed TAs from Pulse Radiolysis of $[Py^{+}_{1,4}][NTf^{-}_{2}]$. Figure adapted with permission from reference [145]. Copyright 2007, American Chemical Society.

Knowledge about the sub 10 ps dynamics of the excess electron in aliphatic ILs is still very limited. The few experiments done to date are limited to the UV photolysis of some neat ILs as well as 266 nm photodetachment of I^{-} solutions. [19,26–28,94]. As far as ILs with aliphatic cations, they have investigated the neat phosphonium IL $[P^{+}_{6,6,6,14}]$ $[NTf^{-}_{2}]$ as well as the$[Py^{+}_{1,4}][NTf^{-}_{2}]$ IL saturated with I^{-} as an electron donor. Both of these liquids were excited at 266 nm (4.7 eV) and transients in the VIS and near-IR were

detected, but only a reconstructed spectrum for the phosphonium salt, at a delay of 250 fs, was produced. Although the results of Unterreiner's experiments qualitatively agree with those from PR, they suffer from low purity of the liquids employed and the fact that the liquids are not flowed during the photolysis experiment, which as the authors themselves show in the case of imidazolium halide ILs, leads to the rapid accumulation of photoproducts [19].

Some important insight on the behavior and fate of excess electrons in aliphatic RTILs has been provided by DFT simulations by the Margulis group. [86, 148] They have found that in $[Py^{+}_{1,4}][NTf^{-}_{2}]$ the very early excess electron is delocalized on several *anions*. This initial delocalized state collapses on a time scale of 50 fs onto a single $[NTf^{-}_{2}]$ anion, yielding the $[NTf^{2-}_{2}]$ dianion, which impulsively fragments across the N–S bond into a radical anion - anion pair. The dissociation fragments in the solvent cage continue to exhibit optical transitions of an intermolecular charge transfer type in the VIS and near-IR, but the cross section for these transitions decay on a sub-ps time scale as the fragments reorient inside the solvent cage. These results seem to be stark contradiction with the long-lived near-IR transients, which because of the extensive evidence that we have discussed above, are assigned to a solvated excess electron.

The main goal of our work has been to study these transient absorptions in a homologous series of the pyrrolidinium bistriflimides liquids, hoping that the dependence of the absorptions and their dynamics on the liquid structure will provide useful information regarding the nature of the absorbing species.

In summary, we have seen that there is extensive evidence in favor of the existence of long lived solvated electrons in aliphatic cation bistriflimide RTILs. This evidence comes mostly from radiolysis studies, in which near-IR TA are detected that react with electron scavengers to produce the known spectral signature of the reduced form of the scavenger. Although still not abundant, there is also evidence from EPR studies that have found signals attributable to the physically trapped electron in these RTILs. We have also seen the *ns* photolysis studies of several electron donors in these liquids lead to TAs with similar characteristics. Preliminary photobleaching studies have shown that the absorption of the electron extends to at least down to ∼600 nm. Pulse radiolysis with a time resolution of about 15 ps has shown that as in common molecular solvents, the relaxation of the electron is accompanied by a blue shift of its TA, and in $[Py^{+}_{1,4}][NTf^{-}_{2}]$in particular, this blueshift has a lifetime of $\sim$ 250 ps.

As we have mentioned above, this broadly accepted interpretation of the experimental facts is challenged by the simulations of the Margulis group, which predict that electrons attach to the NTf^{-}_{2} anion on sub-ps time scales. An important goal of this work will be to provide information that is useful to this question. Additionally, there is still very little reliable experimental data regarding the dynamics of excess electrons on time scales faster than 10 ps. This is in great part due to the viscosity of these liquids, which makes the necessary flow to avoid the accumulation of photoproducts very complicated.

Chapter 2

Instrumentation and Experimental

2.1 Introduction and Pump-Probe Spectroscopy

The work presented here makes use of a technique called Pump-Probe Spectroscopy, also referred to as Transient Absorption Spectroscopy. This technique is based on the following idea: a first short laser pulse (the *Pump Pulse*) induces a dynamic process in the material; then after some variable time delay, another much weaker short laser pulse (the *Probe Pulse*) measures the induced changes. This sequence is repeated many times at different time delays, and thus the time evolution of the induced process can be followed as a function of time. The challenge for the laser spectroscopist is to relate the signals and their evolution to the physical processes that cause them. The property

that is measured as a function of time delay between the Pump and Probe pulses is the change in optical absorption of the sample induced by the Pump pulse, referred to "delta OD" and written: ΔOD. This quantity is determined as follows: with the sample fully relaxed, a probe pulse of some wavelength λ is sent through the sample. The transmitted Intensity is recorded in a detector:

$$I_{np}(\lambda) = \text{Intensity when no Pump} \tag{2.1}$$

where np stands for "no pump". Then the sample is refreshed, and the pump pulse excites the sample. After a controlled and variable time delay Δt, another probe pulse is sent through the same sample spot that was exposed to the pump and the transmitted intensity is recorded again: [1]

$$I_p(\lambda, \Delta t) = \text{Intensity with Pump} \tag{2.2}$$

Then at each λ and Δt, ΔOD is computed as follows:

$$\Delta\, OD(\lambda, \Delta t) = \log \frac{I_p(\lambda, \Delta t)}{I_{np}(\lambda)} \tag{2.3}$$

Thus, as is invariably the case in the experiments reported in this work, if the Pump pulse induces the formation of some species that absorbs light at wavelength λ, ΔOD is a positive number. It is from this spectral dependence of ΔOD and its evolution with time, that the nature of the species responsible for the absorption and their dynamics are studied.

[1] This Δt is typically much less than 1 ns, so that the sample has not had time to move any significant amount.

In what follows, we give a more detailed description of how these experiments are carried out.

2.2 Ultrafast Laser System

The ultrafast laser system consists of an Oscillator, Pulse Stretcher, Regenerative Amplifier and Pulse Compressor. The oscillator is Kerr-lens mode-locked and produces ultrafast pulses centered at 820 nm with a repetition rate of ∼83 MHz and a power of ∼200 mW. These pulses are then sent through the stretcher, where the time width of the pulse is increased, so that when it is later amplified in the Regenerative Amplifier the field does not damage the optics. The Regenerative Amplifier consists a Ti:Sapphire laser cavity pumped by a Nd:YLF laser (Evolution-30) and produces 1.1 mJ pulses centered at a wavelength of 800 nm at a repetition rate of 1 kHz (The power is thus 1.1 W). After being sent through the compressor, an autocorrelation in a 0.1 mm β Barium Borate crystal yields a pulse width of ∼60 fs (fwhm, gaussian).[2] These pulses are then sent to the set of optics that constitute the setup of the experiment, where ultraviolet Pump pulses and broad band Probe pulses are generated. The basics to understand these processes and a description of the set up for their realization are described in what follows.

[2] fwhm stands for full width at half the maximum, and is the width of a symmetrical peak at a height of half its maximum

2.3 UV Pulse Generation

Our laser system delivers near-IR pulses that need to be converted into the UV in order to resonantly excite the IL. This is done by means of sum frequency generation (SFG) in non-linear optical materials, most commonly β Barium Borate (BBO). Here we briefly go over the fundamentals of the phenomenon and then describe the setups used so as to generate the UV frequencies that we have used in these experiments.

If two photons are to disappear for another one to appear, energy needs to be conserved:

$$\hbar\omega_1 + \hbar\omega_2 = \hbar\omega_3 \quad \text{ie} , \quad \omega_1 + \omega_2 = \omega_3 \tag{2.4}$$

where ω is the angular frequency of the laser field and $\hbar$ is the reduced Planck constant. Momentum must also be conserved:

$$\hbar\boldsymbol{k}_1 + \hbar\boldsymbol{k}_2 = \hbar\boldsymbol{k}_3 \tag{2.5}$$

where $\boldsymbol{k}_i$ is the wave-vector of each laser field. Let's first consider the case where the two propagating beams, 1 and 2, do so collinearly. Then, momentum conservation along the propagation direction requires that:

$$k_1 + k_2 = k_3 \tag{2.6}$$

and since $k = \frac{\omega n(\omega)}{c}$, where $n(\omega)$ is the refractive index of the material at the angular frequency ω, it follows that momentum conservation requires that:

$$\omega_1\, n(\omega_1) + \omega_2\, n(\omega_2) = \omega_3\, n(\omega_3) \tag{2.7}$$

Let's further consider the case where ω_1 and ω_2 are the same, that is we are trying to double the frequency. Then:

$$2\omega_1 = \omega_3 \quad \text{and,} \quad 2\omega_1\, n(\omega_1) = \omega_3\, n(\omega_3) \tag{2.8}$$

For the two equations to be satisfied it is needed that $n(\omega_1) = n(\omega_3)$. But this cannot hold since n depends on ω. A clever way to solve this difficulty is to use the fact that in a birefringent crystal, $n(\omega)$ also depends on the relative orientation of the photon polarization with respect to the optical axis of the crystal, so that by turning the crystal an orientation can be found such that $n(\omega_1) = n(\omega_3)$ (where we are not making explicit that $n(\omega_1)$ and $n(\omega_2)$ depend on this orientation, and differently so because of the different relative orientations of the two polarizations).

The simplest case is when the crystal only has one optical axis. The optical axis, denoted by $\boldsymbol{z}$, is the direction along which both polarizations experience the same index of refraction n. If the beam propagation direction, given by $\boldsymbol{k}$, is not along the optical axis, but at an angle θ with it, then one of the polarizations experiences an n that is independent of θ, and the other polarization another n that does depend on θ. This is so because n for a given polarization depends only on the angle between the polarization vector and the optical axis $\boldsymbol{z}$. This can be seen in Figure 2.1, where for any direction $\boldsymbol{k}$ constrained to the same plane with $\boldsymbol{z}$, the angle between the polarization vector perpendicular to the plane and $\boldsymbol{z}$ is unchanged. This polarization vector is called *ordinary*, and it is the vertical one in the figure. The polarization vector orthogonal to the ordinary one is called *extraordinary*, and it is the horizontal one in the figure.

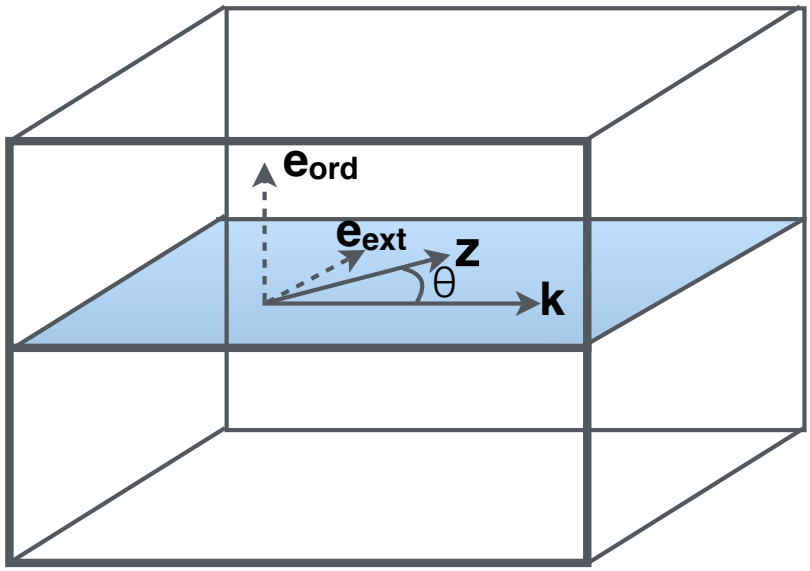

Figure 2.1: Sketch showing in the orientation of the *ordinary* and *extraordinary* polarization vectors with respect to the beam propagation vector $\boldsymbol{k}$ and the optical axis $\boldsymbol{z}$ of a uniaxial crystal. See the text for an explanation.

The index of refraction $n_{ext}(\theta, \omega)$ of the extraordinary polarization of a beam propagating at an angle θ with respect to $\boldsymbol{z}$ can be shown to be expressed by: [35]

$$n_{ext}(\theta, \omega) = n_{ord}(\omega) \sqrt{\frac{1 + \tan^2 \theta}{1 + \dfrac{n_{ord}^2(\omega)}{n_{ext}^2(\omega)} \tan^2 \theta}} \tag{2.9}$$

where $n_{ext}(\omega)$ and $n_{ord}(\omega)$ are the extraordinary and ordinary index of refraction when θ is 90°, and the ordinary index of refraction when θ is 0°. This can be rewritten:

$$\frac{1}{n_{ext}^2(\theta, \omega)} = \frac{\cos^2 \theta}{n_{ord}^2(\omega)} + \frac{\sin^2 \theta}{n_{ext}^2(\omega)} \tag{2.10}$$

Given some ω, there are uniaxial nonlinear materials for which $n_{ord}(\omega) > n_{ext}(\omega)$, and are called *negative* materials, and others for which $n_{ext}(\omega) > n_{ord}(\omega)$, and are called

positive. Usually $n(\omega) < n(2\omega)$ and thus in order for it to be possible to achieve $n(\omega) = n(2\omega)$ at two different polarizations, the 2ω beam must correspond to the axis with lower n, and the ω beam must correspond to the axis with higher n. BBO is a negative material, and thus in order to achieve SFG, the ω beam must be parallel to the ordinary axis and the 2ω beam to the extraordinary axis. This kind of wave mixing is called Type-I, and it is the one used in each of the various SFG processes described below.

2.3.1 Third Harmonic Pulse Generation

The generation of the Third Harmonic (TH) from the fundamental is achieved generally speaking by first doubling the fundamental to generate the second harmonic and then adding the residual fundamental with this second harmonic. To achieve this, the timing and polarizations of the beams need to be controlled and modified.

The method and setup that we have used to generate the third harmonic is based on the inline design reported by Henrik Enqvist [40]. The setup is shown in Figure 2.2. The first optical element, labeled SHG, is a 1 mm BBO crystal that doubles the frequency of part of the incoming fundamental, shown in red as $\times$ because its polarization is perpendicular to the plane of the paper. The resulting second harmonic (SH) is shown in blue and has polarization perpendicular to the original (and remaining) fundamental. Both the SH and remaining fundamental are still overlapping in time. The second element consists of a $CaCO_3$ crystal which delays the fundamental pulse with

respect to the SH. This is done because in the next step, the use a $\frac{\lambda}{2}$ waveplate to make the polarization of fundamental and SH parallel will also affect their timing; and thus the role of the $CaCO_3$ crystal is to correct for the time delay that the waveplate will induce. After the waveplate, the fundamental and second harmonic are timed up and with parallel polarizations, so that they can be added in the last piece of optics which is a BBO to generate the third harmonic (TH).

When the fundamental is compressed to 70 fs fwhm, and its chirp is fine-tuned in the compressor, 350 μJ fundamental pulses produce 8 μJ of the third harmonic. This constitutes a $\sim$2.3 % energy conversion.

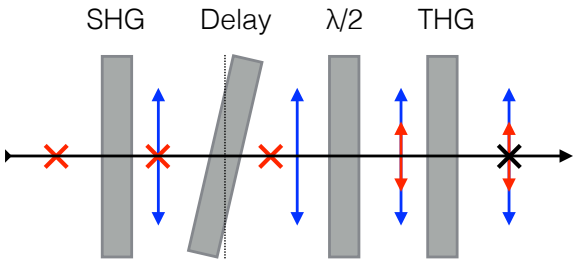

Figure 2.2: Sketch showing, seen form above, the optical elements of the setup used to generate the 266 nm (4.6 eV) pulses. The fundamental travels left to right and its polarization, indicated by $\times$ is perpendicular to the plane of the paper. Double arrows indicate polarization parallel to the plane of the paper. Red indicates the fundamental frequency ω, blue frequency 2ω, and black frequency 3ω. Further explanation is in the text.

2.3.2 Fourth Harmonic Pulse Generation

The generation of the Fourth Harmomic (FH) involves the addition of the fundamental to the TH. This is done as shown in Figure 2.3. The TH is separated from both the SH and the fundamental by means of a 266 nm dichroic mirror (DM1), and then residual fundamental and SH are further removed by reflection on two additional 266 nm dichroic mirrors (DM2 and DM3 in Fig. 2.3). The fundamental and SH that go through DM1 are reflected on an 800 nm dichroic mirror (DM4), so that the SH is transmitted and thus gotten rid of, whereas the fundamental is bounced back to be picked up by a square gold mirror (GM1). DM4 stands on a translation stage so that the fundamental and TH may be properly timed. After GM1 the fundamental is sent through a $\frac{\lambda}{2}$ waveplate to make its polarization parallel to that of the TH. Both beams then go through the same plano convex lens to be focused on the FHG BBO crystal (Type I, 0.1 mm thick, cut for 5,8° beam crossing). The angle between the incoming beams at the FHG BBO is about 6°. Because the three beams after this last crystal are not collinear, the FH can be spatially isolated from the fundamental and TH.

Under the same conditions described above, that is, 800 nm fundamental pulses with 70 fs fwhm and an energy per pulse of 350 μJ, a FH can be produced with an energy of 1.5 μJ per pulse. Thus, with this setup, the energy conversion from fundamental to FH has and efficiency of $\sim$0.4%.

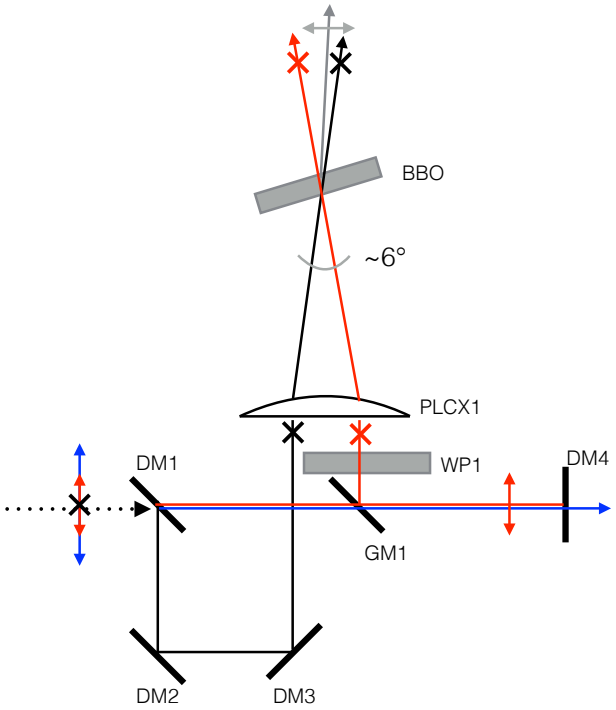

Figure 2.3: Setup used to generate the 200 nm (6.2 eV) pulses. The combined fundamental, SH and TH coming out from the setup above travel to the right. The same polarization and frequency notation is used as above. See the text for a detailed explanation.

2.4 Supercontinuum Generation

In order to be able to probe wide regions of the spectrum at the same time, a source of ultrafast broadband pulses is required. Such broad band pulses can be achieved by focusing a monochromatic laser pulse into a material, and this process is often referred to as *supercontinuum generation*. It is the result of several nonlinear effects. One that plays an important role although does not directly generate the supercontinuum is *self-focussing*: Due to the Kerr-effect, the refractive index in different radial positions of the

laser beam is not the same. For a Gaussian beam, where the intensity decays radially from the center of the beam as a Gaussian function, the index of refraction at the center is larger than elsewhere. As a result, the propagation of light at the center is slower than outer in the beam, and analogously to a convex lens, this results in focusing of the beam, thus further increasing the non-linear effects. At the high irradiance induced by the self-focussing, several non-linear effects can contribute to the spectral broadening, which one happens to dominate being a function of the energy, wavelength of the fundamental and duration of the laser pulse. [35]

As the nonlinear material for the supercontinuum generation we have used a 2 mm thick Sapphire disk. On this substrate, using 70 fs (gaussian, fwhm) fundamental pulses (800 nm), a continuum spanning the spectral region from 430 nm to 1350 nm is easily obtained.

2.5 Experimental Setup

A scheme of the setup used in the experiments reported in this work is shown in Figure 2.4. The $\sim$600 μJ of fundamental in the main red line are split at BS1, 15% being reflected to the probe system branch to generate a supercontinuum, and the rest transmitted to the UV generation system. The power in either branch is controlled by means of a $\frac{\lambda}{2}$ waveplate – polarizer pair attenuator.

The pump branch is modulated at half the laser repetition rate, 500 Hz. After reflection on the computerized delay stage the fundamental is directed to the inline

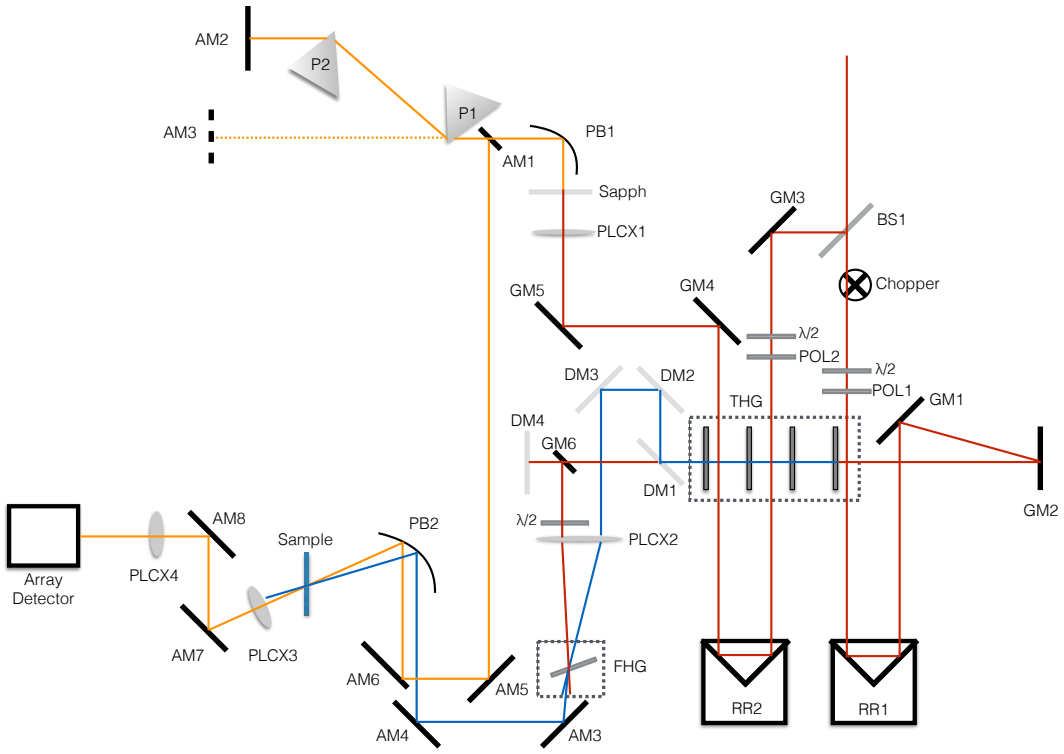

Figure 2.4: Scheme of the laser table setup used. GM: Au Mirror. AM: Al mirror. DM: Dichroic mirror. RR: Retroreflector stage. PLCX: Plano convex lense. PB: Parabolic Mirror. P: Prism. POL: Thin Polarizer.

THG system described above and then to the FHG system. The resulting 200 nm pulses are then focused on the sample by means on an off-axis parabolic mirror (1" focal length). The pump beam is focused to a spot diameter of 450 μm on the sample. It was found that the power of the 200 nm pulse was extremely sensitive to alignment, and so it was decided not to move the pump stage.

In the probe branch, the fundamental is focused near the exit window of the 2 mm Sapphire plate, by translating the plate back and forth till the position is found

which requires the least fundamental power. The diverging white light (and excess fundamental) are collimated by means of an off-axis parabolic mirror. Depending on whether the VIS (1.26 eV – 2.76 eV, 450 nm – 980 nm) or near-IR (0.92 eV – 1.38 eV, 900 nm – 1350 nm) parts of the spectrum are to be investigated the white light is treated differently. In the case of near-IR detection, the collimated continuum is simply sent along a delay line and through a long-pass filter (FGL1000, Thorlabs) to remove the visible components and excess fundamental, and to flatten the spectrum. For visible detection, the collimated beam is sent through a prism line to compensate for chirp and to allow filtering of the 800 nm fundamental by placing a metal block in the spectrally dispersed light. The two paths are made precisely equal (taking into account the presence of the longpass filter when the near-IR is used) so that by translating the P1, shown in Fig. 2.4, out of the beam path, it is possible to switch easily between to two probing modes. In both cases the probe light was focused with a diameter of 50 μm on the sample. The probe stage was moved to scan the time delays.

For the experiments in the visible region, the probe light transmitted through the sample was dispersed with a grating (150 lines/mm, 500 nm blaze) and detected using a 256 linear pixel silicon diode array (Hamamatsu S3901-256Q). For the near-IR experiments, the transmitted probe light was dispersed with a grating (150 lines/mm, 1.2 μm blaze) and detected with a 256 linear pixel InGaAs diode array (Hamamatsu G9213-256S).

2.6 Sample Translation

One of the challenges of these experiments was to translate the liquid exposed to the pump laser quickly enough so as to prevent the accumulation of photoproducts in the area where the liquid is exposed to the pump laser. The constraints to overcome have been the limited amount of ILs at our disposal, and the high viscosity of these liquids.

We have designed and built a spinning cuvette that consists of two fused silica windows (Corning Grade 7980, Sydor), 1.00 mm in thickness, 50.8 mm in diamater, which sandwich a PTFE ring spacer (Alfa Chemicals), 1.6 mm in thickness, and which has two perforations in the radial direction, (1.25 mm diameter) which allow for the injection of IL, and of quenchers during the experiment. These parts are held together by two 3D-printed plastic pieces (material: digital ABS: RGD 515 + RGD 535) designed to fit and press the cell parts, which are pressed by 8 nylon screws. A scheme with the detailed measures of the parts is included in the Appendix. The precaution is taken to include an O-ring (50 mm ring diameter, 1.5 mm thickness) between each window and plastic ring holder so that the pressure applied is homogeneous in the fused silica windows. The cell accepts a volume of 1.9 mL of liquid. On the back of the cell, a 1/4 ” collar with a set screw is glued to the center of the window by means of Scotch (3M) double sided tape. The cell is attached to the spinning shaft through this collar.

The cell is spun by a high torque 12 V DC geared motor with a max speed of 300 rpm. See Figure 2.6 for a picture of the setup. Additionally, the cell is translated horizontally back and forth driven by a computerized stage at a speed of 1 mm/s and with an

Figure 2.5: Front and back view of the 3-D printed cell.

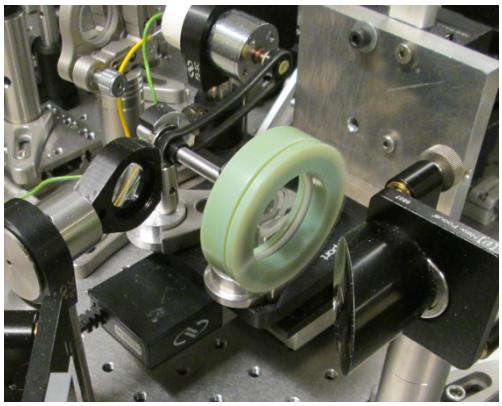

Figure 2.6: View of the spinning cell in the sample holder.

amplitude of 6 mm (from extreme to extreme), so as to maximize the volume of liquid that is exposed to the laser. The cell was aligned with respect to the laser so that the outermost part of the liquid was exposed to the light, again so as to maximize the volume of liquid exposed and also so that the liquid irradiated would move as fast as possible with respect to the beam crossing spot. Typically the laser spot would (relatively) translate between 5 mm and 5 + 6 = 11 mm from the outer edge of the cell window.

That is, between 20 mm and 14 mm from the center of the cell. Thus (ignoring the much slower translation motion), when the beam crossing is in the outermost situation, it is moving with respect to the IL sample:

$$20\text{mm} \times 2\pi \times \frac{300 \text{ rev}}{60\text{s}} = 630\frac{\text{mm}}{\text{s}} = 630\frac{\mu\text{m}}{\text{ms}} \tag{2.11}$$

and when closest to the center:

$$14\text{mm} \times 2\pi \times \frac{300 \text{ rev}}{60\text{s}} = 440\frac{\text{mm}}{\text{s}} = 440\frac{\mu\text{m}}{\text{ms}} \tag{2.12}$$

Thus for a pump spot size of 400 μm or lower, at our repetition rate of 1 KHz, ie, 1 ms between probe shots on the sample, we are sure that each shot finds fresh IL.

2.7 Ionic Liquid Purification

The series of ILs that we have used have two distinct origins: the $[Py^+_{1,3}][NTf^-_2]$, $[Py^+_{1,6}][NTf^-_2]$ and $[Py^+_{1,10}][NTf^-_2]$ were synthesized and kind made available by Gary Baker [61]. The $[Py^+_{1,4}][NTf^-_2]$ liquid was purchased from Iolitec (99.5 %, IL-0035-UP-0050).

In our ongoing attempts to further clean the ILs, we tried to stir the neat liquids with solid cleaning agents, *without the addition of any solvent.* This has the disadvantage that very thick mixtures are formed which are time-consuming to filter, but has the advantage that no external impurities from the solvent are added. The procedure consisted in stirring overnight the crude IL with 2 to 5% mass the cleaning agent. After stirring,

the black solid was separated by filtering under vacuum through a small fritted glass funnel (ChemGlass, F) into a tared vial. For volumes of IL greater than approx. 2 mL, recovery ratios of 95 % were typical. The effectiveness of the purification method was evaluated by UV-VIS absorption. A 1 mm Suprasil cuvette, blanked with respect to the empty cuvette, that is, full with air, was used. The index of refraction of the IL caused a negative shift in the thus blanked UV-VIS spectrum, which is compensated by subtracting the constant baseline value where no absorption is present. All these steps were done with no precautions as to exposure to air.

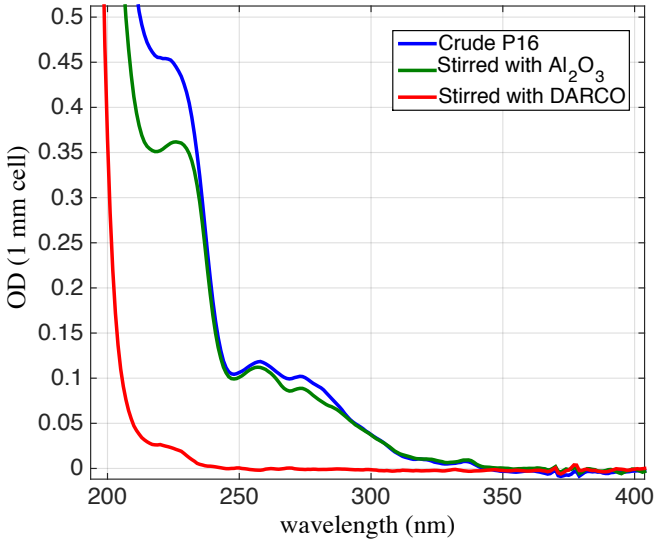

Figure 2.7: UV-VIS absorption spectra of preliminary cleanings of the $[Py^{+}_{1,6}][NTf^{-}_{2}]$ ionic liquid.

Activated Alumina (Brockman Grade I) and activated charcoal (DARCO grade, Sigma-Aldrich) were used in preliminary trials on several crudes. It was found that DARCO consistently gave much better results. See figure 2.7 for an example. Stirring

with DARCO overnight at 80° vs. stirring at room temperature was found to have identical results. Application of other solid agents on the samples already cleaned with DARCO also gave negative results: Solid ground $AgNO_3$ in an attempt to extract halides, K_2CO_3 in an attempt to extract acidic impurities, NaH_2PO_4, in an attempt to extract basic impurities; all produced absorption spectra equal or worse than those of the original sample. Thus, the cleaning procedure was limited to repeated cleaning with DARCO activated charcoal, until the OD would not further decrease. See Figure 2.8 for an example.

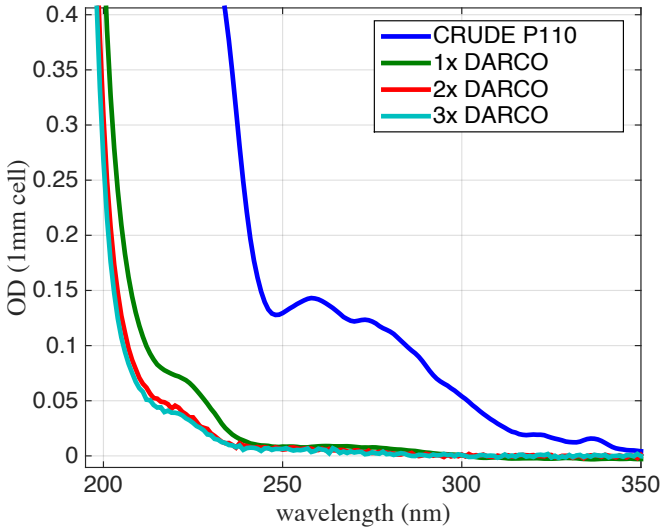

Figure 2.8: Evolution of UV absorption spectra of $[Py^+_{1,10}][NTf^-_2]$ with successive DARCO cleanings.

The absorption spectrum of the cleanest IL samples obtained for $[Py^+_{1,3}][NTf^-_2]$, $[Py^+_{1,4}][NTf^-_2]$, $[Py^+_{1,6}][NTf^-_2]$ and $[Py^+_{1,10}][NTf^-_2]$, are shown in Figure 2.9.

The purified liquids where introduced in a desiccator with a sand at 85° and kept

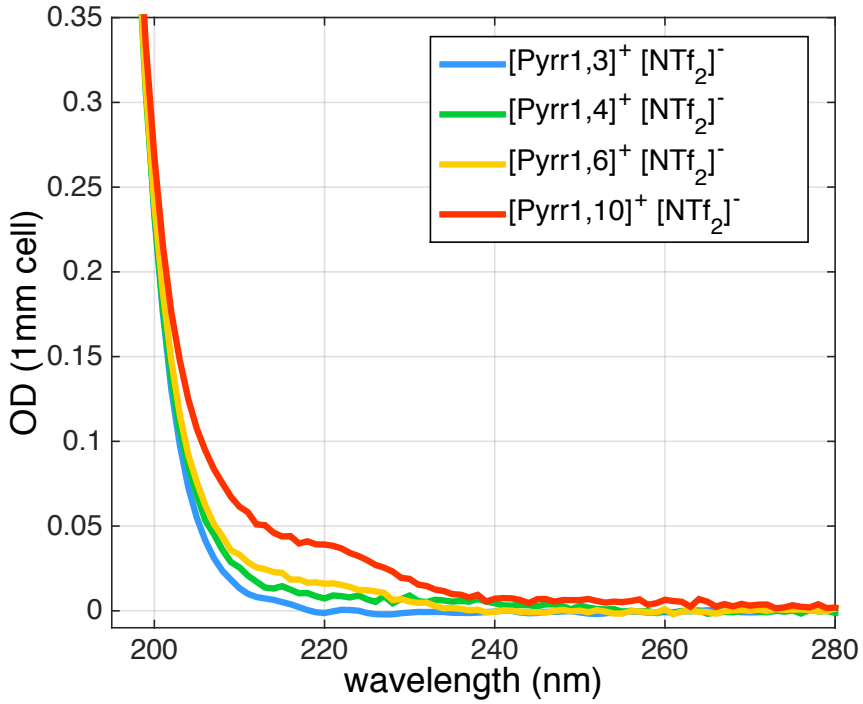

Figure 2.9: UV absorption spectra of the cleanest samples of each IL obtained.

under vacuum for 6 days. The desiccator was then refilled with N_2, the samples removed and taken into the glove box, where they were kept henceforth.

2.8 Sample Handling

Prior to a photodetachment experiment, the sample was treated thus: the assembled, clean spinning cell was kept in an oven at 50° and introduced into the glove box while still warm. The corresponding IL or solution was then injected into the cell up to approx. 90% of the volume. This empty volume is important because it is used, in case some chemical is introduced into the cell later on, to mix the contents. This is done,

once the cuvette is mounted on the spinner, by spinning at a (slow) speed such that the bubble sit on a fixed position between the center and outer extreme of the cell, so that the liquid is forced to go around the fixed bubble.

With the cuvette thus filled, two stainless steel screws with a small Tygon O-ring around them are screwed into the radial perforation in the PTFE spacer. The full and closed cell is then removed from the glove-box and the experiment started.

Chapter 3

Photodetachment and electron reactivity in $[Py^{+}_{1,4}][NTf^{-}_{2}]$

3.1 Introduction

Published examples using photolysis to probe electrons in RTILs to date are currently limited to the pump-probe experiments of Unterreiner and coworkers. [19, 26, 27] The only absorption spectrum reported was reconstructed for trihexyltetradecylphosphonium bistriflimide, $[P^{+}_{6,6,6,14}][NTf^{-}_{2}]$, less than a picosecond after photoionization. [26] The absorption was most intense in the visible and declined rapidly at wavelengths longer than 1000 nm. Individual wavelength probes found decays at all wavelengths in the visible and near-IR. Inconsistency with respect to radiolysis experiments could stem

from fundamental differences between the ionization processes. However, these photolysis studies all used a static sample and contamination in the signals from build up of photoproducts offers another viable explanation. In a later manuscript the authors actually highlight how rapidly secondary photoproducts contaminate the photoionization studies of [aromatic$^+$][halogen$^-$] RTILs, "The results suggest that the development of flow-cell systems for highly viscous ionic liquids is urgently needed to quantitatively investigate their ultrafast dynamics." [19] In this manuscript we show that rapid accumulation of photoproducts interferes with photolytic experiments on aliphatic RTILs and we avoid these problems using a sealed flow system. This is only the second photoionization study we are aware of on RTILs where such interference was avoided, the first being the recently submitted investigation of imidazolium bromide by Musat *et al.*. In this study we characterize the transient absorption (TA), spectrum following photodetachment in neat [$Py^+_{1,4}$][NTf^-_2] on ultrafast time scales and measure sub-ps reaction dynamics of the pre-solvated electron. The results are considered in the context of recent radiolysis studies and computational predictions.

3.2 Experimental

Time-resolved pump-probe: Our experimental setup starts with a home-built, regeneratively amplified, Ti:sapphire laser system producing 1 mJ, 58 fs pulses (Gaussian, FWHM) at a repetition rate of 1 kHz and centered at 800 nm. A portion of the light was split off to create excitation pulses at 266 nm using a series of three inline BBO

crystals as described in the Experimental Chapter. Focusing a portion of the 800 nm light into a 2 mm thick sapphire plate produced the continuum probe. The collimated parallel pump and probe beams were focused and crossed in the sample using an off-axis parabolic aluminum mirror. The 266 nm pump pulse was 140 fs (Gaussian, FWHM) and had a waist of 11 μm ($1/e$) at the sample. A small fraction of the 266 nm pump light was diverted to a UV monochromator (Jarrel Ash 82-410, 300 nm blaze), measured with a PMT (Hamamatsu R636-10), and calibrated against the irradiance at the sample using a power meter (Molectron EPM-1000). The setup continuously monitored the incident pump irradiance during the experiments. The pump power was adjusted using a half-wave plate followed by a polarizing beam splitter at the entrance to the third harmonic generator. All presented data correspond to a pump irradiance of 1.1 TW/cm^2, except measurements of the signal dependence with respect to pump irradiance.

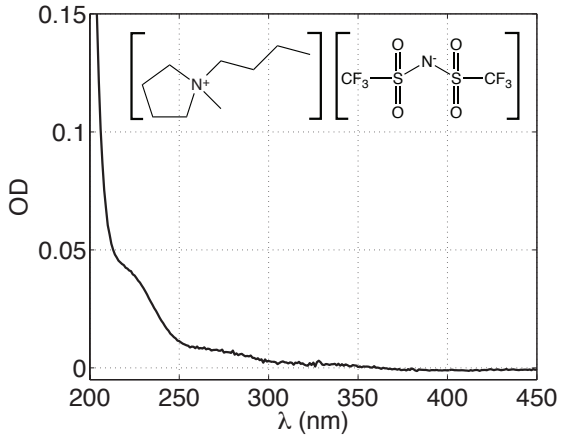

Figure 3.1: Absorption spectrum of $[Py^+_{1,4}][NTf^-_2]$ in a 1 mm path cuvette. The inset shows the molecular structure of the Ionic Liquid.

Ionic liquid samples: The $[Py^+_{1,4}][NTf^-_2]$RTIL was prepared as described in reference [59]. Samples were stored and handled in a glove box and were dried in a vacuum oven immediately prior to use. During the experiments 3 mL of sample was placed in a sealed flow system consisting of a small reservoir, peristaltic pump, low volume tubing, and a 1 mm optical path length flow cell with Spectrosil windows (Starna). The entire flow system was kept in a vacuum oven for at least 12 hours prior to use. The flow rate was 0.09 mL/s. Given the 0.1 cm^2 cross sectional area of the flow cell, the average vertical velocity in the cell was 9 μm/ms. As a result, the sample in the excitation volume was replaced at a rate roughly comparable to the laser repetition rate. The reservoir was continuously purged with dry nitrogen. Water content was determined by Karl-Fisher titration (Coulometric, Denver Instruments). The $[Py^+_{1,4}][NTf^-_2]$ samples typically had water content of 110 ppm at the start of the experiment, with an increase in water content of <1% per hour in the flow system. Absorption spectra were measured in a 1 mm path length cell using a Cary 14 running the OLIS Golbalworks software and a representative spectrum is shown in Fig. 3.1. The samples were visibly clear, with the absorption limited to wavelengths shorter than 350 nm and increasing rapidly below 220 nm. The OD in a 1 mm sample cell at the excitation wavelength of 266 nm was 0.008. Quenching experiments were conducted using perchloric acid as an electron scavenger (70% $HClO_4$, Aldrich, used as received). The amplitudes of all measurements were corrected for dilution relative to the neat RTIL assuming additive volumes. This was a small correction in all cases, with the maximum $HClO_4$ addition

representing less than 2% of the total sample volume.

3.3 Results

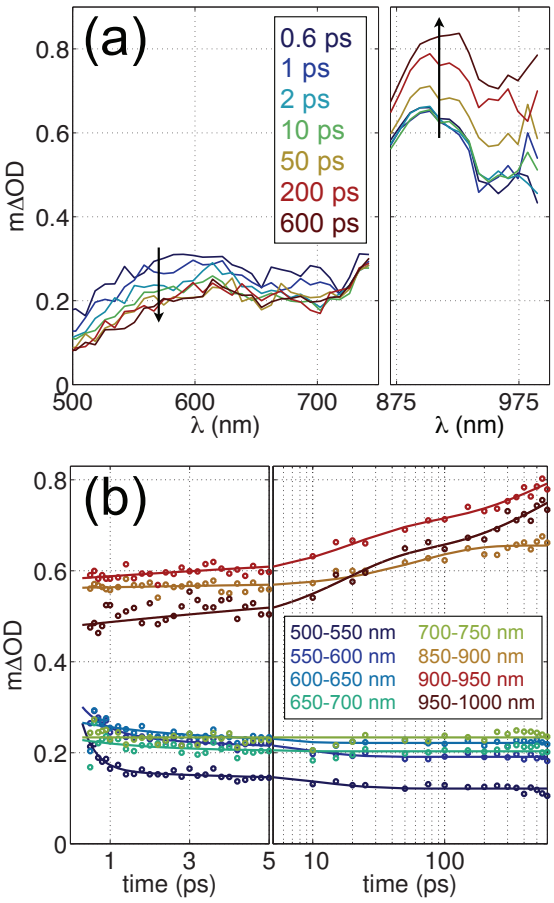

Figure 3.2: **(a)** Change in the probe spectrum after excitation at 266 nm. **(b)** Time dependence for 50 nm wide regions.Fits as described in the text. Optimized parameters are listed in Table 3.1.

The pump-probe spectra are shown in Fig. 3.2(a). The change in the optical density is positive at all wavelengths and delay times measured, and there is no detectable fluorescence following 266 nm excitation (4.7 eV). As a result, all observed changes are

considered to be pump-induced transient absorption. The dependence of the TA signal at 980 nm on the pump irradiance at a delay of 500 ps is shown in Fig. 3.3. Optimization of a linear fit to the data produced a slope of 0.99 ± 0.16 indicating that the observed TA is the result of one-photon process at 4.7 eV. A linear dependence of the TA on the pump irradiance was also found at a pump-probe delay of 1 ps. There was no discernible change in the shape of the TA spectrum over the range of pump irradiance shown in Fig. 3.3. All other data was taken at a pump irradiance of 1.1 TW/cm^2, indicated by the arrow in Fig. 3.3.

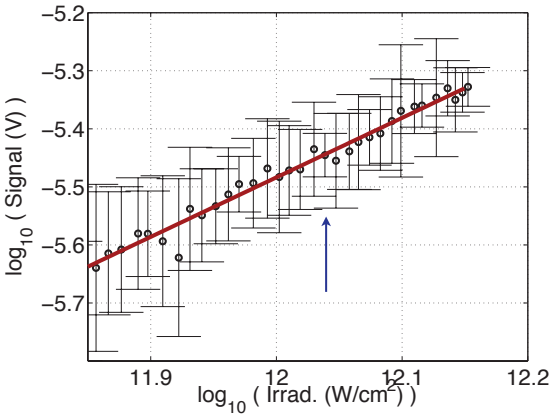

Figure 3.3: Signal at 980 nm and at a delay of 500 ps as a function of the 266 nm pump irradiance. The arrow indicates the pump irradiance used for all other presented data. The line is the fit with a slope of 0.99 ± 0.16, and error bars span a total of two standard deviations in the signal.

Rapid accumulation of photoproducts was observed during the absence of sample translation. Figure 3.4 depicts the increase in TA in the first three minutes after a flowing sample is stopped. Initially the amplitude of the TA spectrum increases linearly in time without large changes in shape, suggesting build-up of primary photoproducts.

However, after 30 minutes of exposure to the 266 nm pump laser, static samples show changes in both their time integrated absorption and TA spectra. To avoid interference from accumulation of photoproducts, the RTIL samples were flowed in all other data presented.

wavelength (nm)	τ_1 (ps)	a_1 (mOD)	τ_2 (ps)	a_2 (mOD)	H (mOD)
	– decay –			**– decay –**	
500–550	0.37	0.24	11	0.039	0.121
	(0.28, 0.46)	(0.15, 0.33)	(6.7, 15)	(0.034, 0.045)	(0.0119, 0.123)
550–600	0.68	0.10	7.9	0.046	0.191
	(0.43, 0.92)	(0.08, 0.13)	(4.5, 11)	(0.036, 0.057)	(0.189, 0.193)
600–650	–	–	2.9	0.049	0.222
			(2.0, 3.9)	(0.040, 0.058)	(0.218, 0.225)
650–700	–	–	2.0	0.029	0.203
			(0.6, 3.3)	(0.016, 0.041)	(0.200, 0.206)
700–750	–	–	–	–	0.234
					(0.232, 0.236)
	– rise –			**– rise –**	
850–900	–	–	64	0.093	0.562
			(52, 75)	(0.089, 0.097)	(0.560, 0.565)
900–950	19	0.11	550	0.15	0.582
	(14, 23)	(0.09, 0.12)	(38, 1050)	(0.08, 0.22)	(0.578, 0.586)
950–1000	18	0.14	500	0.16	0.491
	(12, 25)	(0.11, 0.16)	(–140, 1120)	(0.072, 0.26)	(0.484, 0.497)

Table 3.1: Fitting parameters for the time dependent changes in optical density shown in Fig. 3.2(a). The exponential time constants are τ_n, the exponential weighting factors are a_n, and H is the amplitude of the Heaviside function. Below each value is the 68.2% confidence interval from the nonlinear fitting when all variables are simultaneously optimized.

The TA spectra in Fig. 3.2(a) appear bimodal and there is a clear wavelength dependence to the time evolution. The most obvious contrast is between the relatively

rapid decline found for shorter wavelengths compared with a somewhat delayed increase at longer wavelengths. This spectral dependence of the TA evolution is highlighted in Fig. 3.2(b), where the time evolution is shown for individual 50 nm wide windows of the probe. These transient signals were fitted with a sum of exponential decays, $S_{\mathrm{TA}}(t) = a_n e^{-t/\tau_n}$, exponential rises, $S_{\mathrm{TA}}(t) = a_n(1 - e^{-t/\tau_n})$, and a Heaviside function representing a static change in absorption on the time scale that our experiments probe. The sums were convoluted over the instrument response and the optimized fitting parameters are reported in Table 3.1. A minimum number of functions was used in each fit, with additional functions added only when statistically significant changes in the fit residual resulted following optimization. The combination of ∼150 fs time resolution and the low signal levels caused interference around the time origin (*i.e.* when the pump and probe pulses are time coincident), including cross-phase modulation, to contaminate the signals. For this reason, all fitting was limited to time delays larger than 400 fs. Overall, the TA has a rapid sub-ps decay around 500 nm that slows as the probe moves to longer wavelengths. Around 700 nm the TA becomes time independent, even on the shortest time scales probed, and at wavelengths longer than 900 nm the TA has a bimodal rise with time constants of 20 ps and ∼500 ps. As reported in Table 3.1, there is significant uncertainty in the determination of time constants that are comparable to the maximum measured time delay. However, the addition of a roughly 500 ps delay did improve the fit quality at wavelengths longer than 900 nm, and a rise beyond 100 ps is clearly evident in Fig. 3.2(b).

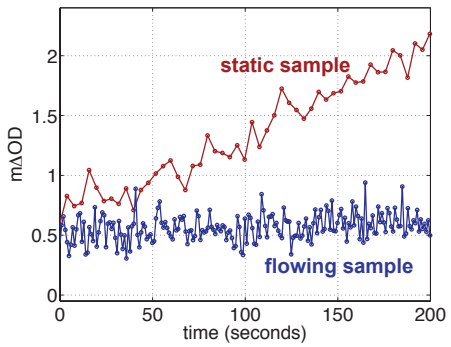

Figure 3.4: Change in signal at 925 nm after excitation at 266 nm and at a delay of 1 ps as a function of real time. The first data point is roughly 10 seconds after the shutter opened to illuminate the sample.

Perchloric acid was added as an electron scavenger, and the influence of $HClO_4$ on the TA is shown in Figs. 3.5 and 3.6. To isolate the decay caused by reaction with the acid from the TA dynamics in the neat IL, the data are plotted as the fraction of the TA in the absence of $HClO_4$. In Fig. 3.5 the TA decay at 980 nm is shown as a function of $HClO_4$ concentration. These data were fitted with a sum of exponential decays, and the optimized fitting parameters are reported in Table 3.2. At all $HClO_4$ concentrations there is a 300 fs decay that increases in amplitude with increasing concentration and a slow (>1 ns) decay that is not accurately determined but improves the fit quality in all cases. At the two highest concentrations the fits are also improved by the addition of a ∼10 ps decay. Figure 3.6 shows how the addition of $HClO_4$ changes the entire probe spectrum. Although the signal to noise in these spectrum ratios is limited, it can be seen that there is decay of the TA at all probe wavelengths, and that the amount of decay depends on the wavelength. These results are considered in more detail below.

$[HClO_4]$ (10^{-3} M)	τ_1 (ps)	a_1	τ_2 (ps)	a_2	τ_3 (ps)	a_3	$(a_1+a_2+a_3)$
	– decay –		**– decay –**			**– decay –**	
42	0.38	0.05	–	–	5900	0.91	0.96
	(-0.93, 1.7)	(-0.04, 0.14)			(290, 12000)	(0.87, 0.94)	(0.86, 1.06)
76	0.38	0.084	–	–	4300	0.85	0.93
	(-0.38, 1.15)	(0.0, 0.17)			(1100, 7500)	(0.82, 0.89)	(0.84, 1.02)
111	0.27	0.15	–	–	3300	0.79	0.94
	(-0.02, 0.56)	(0.061, 0.24)			(1400, 5200)	(0.76, 0.82)	(0.85, 1.04)
179	0.28	0.19	7.5	0.076	3200	0.66	0.93
	(-0.093, 0.66)	(0.08, 0.30)	(-19, 34)	(-0.03, 0.19)	(-220, 6600)	(0.58, 0.73)	(0.76, 1.1)
347	0.31	0.39	8.8	0.11	1700	0.47	0.97
	(0.11, 0.51)	(0.27, 0.50)	(-15, 32)	(0.00, 0.22)	(190, 3100)	(0.39, 0.54)	(0.83, 1.14)

Table 3.2: Fits to the quenching data shown in Fig. 3.5. The exponential time constants are τ_n and the exponential weighting factors are a_n. Below each value is the 68.2% confidence interval from the nonlinear fitting when all variables are simultaneously optimized.

3.4 Discussion

3.4.1 The transient absorption spectra

Analogous to many common solvents, the absorption spectrum of an excess electron in a room-temperature ionic liquid is typically dominated by a broad band in the near-IR. [42, 67, 143, 145] The absorption peaks at wavelengths longer than 1000 nm, and commonly around 1100 nm for pyrrolidinium RTILs. Time resolved radiolysis studies demonstrated that the spectrum is time dependent over a much broader dynamic range than most common solvents, with the spectrum shifting to shorter wavelengths as the electron is solvated. Electron solvation is multifaceted and extends to the ns time regime. [145] In neat, $[\text{aliphatic}^+][NTf_2^-]$ RTILs the lifetime of the electron is >100 ns, and additional dynamics are limited to spectral diffusion associated with solvation. In

some cases a much smaller band in the visible portion of the spectrum has also been observed. [74, 143] This band can exhibit different lifetime kinetics than the major band in the near-IR, and Wishart suggested that it might involve some absorption from the hole left behind in the detachment.

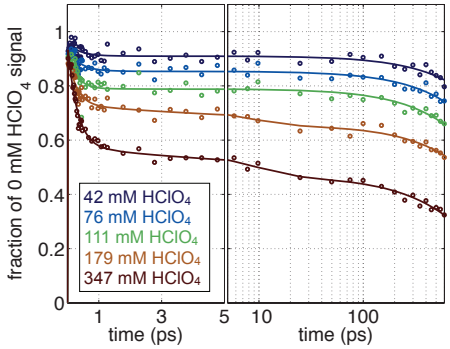

Figure 3.5: Fraction of the remaining signal at 980 nm in the presence of $HClO_4$. Fits as described in the text. The associated fitting parameters are listed in Table 3.2.

Unterreiner and coworkers reconstructed the transient spectrum 250 fs after UV photo-excitation of $[P^+_{6,6,6,14}][NTf_2^-]$. [26] To our knowledge, this is the only published report of an ultrafast time-resolved, photo-initiated experiment on a neat, aliphatic RTIL. In contrast with the transient radiolysis spectra, the photoionization TA was most intense in the visible portion of the spectrum, spectrally flat for wavelengths shorter than 900 nm, and fell off rapidly at wavelengths longer than 1000 nm. The spectrum in the photoionization experiment at 250 fs should precede a large fraction of the solvation. All other experiments indicate that the pre-solvated spectrum is shifted to longer wavelengths than the solvated spectrum, presenting even greater contrast between photolysis and radiolysis reports for $[\text{aliphatic}^+][NTf_2^-]$ RTILs. One possible

explanation is the difference in the cation. However, the TA spectra for a number of different cations have been measured using radiolysis, and all aprotic, aliphatic examples peak at wavelengths longer than 1000 nm. An alternative explanation is signal contamination from the build up of photoproducts. Unterreiner and coworkers subsequently observed rapid accumulation of interfering signals in static samples of the more reactive imidazolium halides. [19] We have shown in this work that the same problems are present in pump-probe measurements on static samples of an [aliphatic$^+$][NTf_2^-] RTIL.

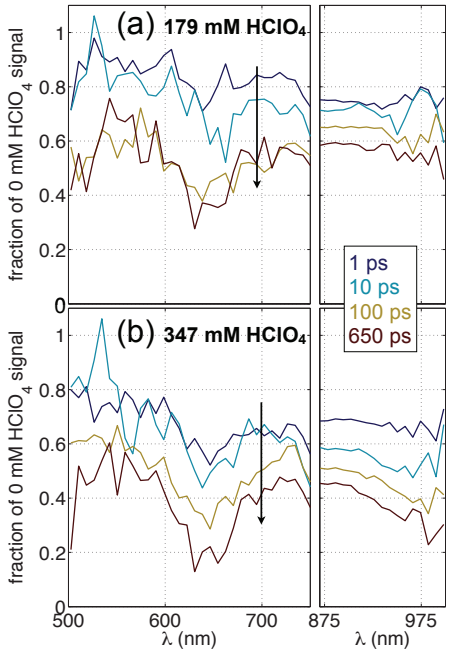

Figure 3.6: Change in probe spectrum following excitation at 266 nm in the presence of **(a)** 179 mM $HClO_4$ and **(b)** 347 mM $HClO_4$. The data are presented as the fraction of the signal in the absence of $HClO_4$.

The TA spectra in Fig. 3.2(a) are limited to $\lambda < 1000$ nm, and therefore lack

enough coverage in the near-IR (where the electron absorption peaks) to use the spectra themselves as definitive evidence that the absorber is the electron. However, qualitative agreement with radiolysis results in the spectral range covered and the concentration-dependent quenching probed at 980 nm presented in Fig. 3.5 both indicate that the electron is the majority contributor to the observed absorption. Figure 3.6 demonstrates that there is dependence of the quenching on the wavelength probed. Quenching is more efficient around 650 nm and at wavelengths longer than 900 nm. At a delay time of 650 ps and the highest quencher concentration measured, the spectrum ratio in Fig. 3.6 appears bimodal with maxima at roughly 500 nm and between 750 nm and 850 nm. Spectral dependence of the quenching indicates that, in terms of reactivity with the acid, there is more than one absorbing species in the TA.

Measuring lifetimes inaccessible to our current experiments, $t > 1$ ns, Wishart observed different decay rates in the visible and near-IR for TA in neat $[P^+_{1,4,4,4}][NTf^-_2]$ and posed the possibility that there were additional contributions at visible wavelengths from the hole absorption. [143] Recently, Margulis *et al.* calculated the electronic structure in a set of small RTILs and the absorption spectrum for both the dry excess electron and the dry excess hole in the aliphatic cation trimethylpropylammonium, $[N^+_{1,1,1,3}][NTf^-_2]$. [86] They found that the HOMO and LUMO *both* reside on the anions. The HOMO/LUMO gap in the liquid was roughly 5 eV, which is consistent with the one-photon ionization at 4.5 eV reported here for $[Py^+_{1,4}][NTf^-_2]$. Using the computational predictions as a guide, we tentatively assign the nascent photodetached electron

in $[Py^+_{1,4}][NTf^-_2]$ to a state delocalized over the NTf^-_2 anions. The calculated absorption spectrum for the dry excess electron in $[N^+_{1,1,1,3}][NTf^-_2]$ is bimodal, with the largest peak in the near-IR and a smaller peak on the blue side of the visible. The calculated spectrum for the hole is also bimodal, has lower intensity, and overlaps with the electron spectrum but is offset to shorter wavelengths. The measured quenching ratios presented in Fig. 3.6 are consistent with the prediction of overlapping, offset bimodal absorption spectra for the electron and hole. Assuming that reaction with the quencher is dominated by the electrons, at long delay and high quencher concentration the spectrum ratio in Fig. 3.6 reflects the residual hole absorption. The maximum quenching around 640 nm corresponds to a minimum in the hole absorption, and the hole absorption falls off at wavelengths longer than 900 nm.

Recently, the TA in $[Py^+_{1,4}][NTf^-_2]$ was measured with 15 ps time resolution and 100 nm wavelength resolution following radiolysis. [145] The spectra were broad with a single maximum that shifted from 1300 nm to 1100 nm over the first few hundred picoseconds. The TA spectra in Fig. 3.2(a) agree with the radiolysis results in many respects. Both experiments show an increase in absorption with time for 870 nm $< \lambda <$ 1000 nm, a decrease in absorption for $\lambda <$ 700 nm, and time independence of the absorption near 700 nm. However, the shape of the TA is different. Although the spectral resolution in the radiolysis experiments is lower, the bimodal shape shown in Fig. 3.2(a) is not apparent in the radiolysis TA. Single value decomposition, SVD, of the radiolysis spectra resulted in two dominant components. The one with smaller

amplitude shows the same bimodal structure as the TA spectra presented in Fig. 3.2(a), including an apparent shoulder around 900 nm. This SVD component was associated with a trapped, pre-solvated electron. The majority spectral component in the SVD analysis was nearly identical to the spectrum at 50 ns with a single maximum at 1100 nm and was assigned to the solvated electron. Given only the shorter wavelengths available in Fig. 3.2, quantitative evaluation of the relative contribution from the fully solvated component is not possible. The shape, however, with a resolved maximum around 620 nm, indicates that the fully solvated electron spectrum is a smaller contributor to the photolysis TA. The qualitative difference in the two experiments highlights that lower energy ionization via photodetachment leads to a different initial population of electrons and holes than radiolysis. Greater spectral coverage into the near-IR for the photodetachment experiments is needed to better understand the contrast between the different methods.

3.4.2 Geminate recombination and solvation

At first blush, the lack of decline in amplitude for the TA in Fig. 3.2 at wavelengths longer than 750 nm might suggest an absence of geminate recombination or any other dynamics. However, this conclusion is difficult to reconcile given the known solvation dynamics, associated spectral diffusion, and substantial reactivity of the electron at early times that is discussed in detail in the next section. [10, 145] The long wavelength side of Fig. 3.2 resides on the high-energy shoulder of the primary electron absorption.

TA in this region increases as the band shifts to shorter wavelength with solvation of the electron. Radiolysis studies demonstrated that there must be electron solvation on time scales shorter than 15 ps, [145] and dipolar solvation measured in $[Py^{+}_{1,4}][NTf^{-}_{2}]$ identified significant sub-ps contributions. [10] It might seem unlikely that there would be near perfect cancellation between the spectral diffusion rise and geminate recombination fall in the first 10 ps. However, as we outline in the next section, reactivity of the electron is mediated by solvation. As a result, the reaction rate of the electron at early time is, in fact, the solvation rate. With both reactivity and spectral diffusion controlled by the same solvation rate, the conclusion of near perfect cancellation between the oppositely signed contributions becomes the expectation rather than a seemingly improbable coincidence.

The visible portion of the TA covers the majority of the higher energy absorption band of both the electron and hole. The entire combined band shows a decay indicating a loss of the initially generated electrons and holes in addition to any spectral diffusion. On the short wavelength side of Fig. 3.2 there is a 400 fs decline with an amplitude that accounts for roughly half of the initial absorption, see Table 3.1. This decay slows with increasing wavelength, in part due to increasing overlap with spectral diffusion of the broad near-IR electron band. The decay is nearly complete in one picosecond, after which the visible band remains static on the 600 ps time scale probed in this experiment. Sub-ps recombination that is rather abruptly arrested is inconsistent with standard models limited to diffusive recombination from an initial spatial distribution,

typically exponential or Gaussian, at a finite sink radius. [29,38,51,69,121] These results are consistent with the initial dry electrons being relatively delocalized, reactive, and mobile. Trapping of the electrons via solvation on sub-ps time scales mediates the fast recombination kinetics for dry electrons and holes. The associated reduction in reactivity and mobility (the trapped electrons are left to diffuse in a medium with $\eta \sim 75$ mPa·s [61]) results in vanishingly little recombination during the subsequent 600 ps. Analogous dynamics are found for reaction of the electrons with proton scavengers, as discussed in detail in the next section.

3.4.3 Electron reactivity

In Fig. 3.5 electron scavenging by perchloric acid was probed at 980 nm, where a significant fraction of the absorption is from the electron. The data are plotted as the fraction of the signal in the absence of the scavenger to eliminate contributions to the dynamics associated with spectral diffusion. The last column in Table 3.2 shows that the sum of the exponential weights is one (within error) at all $HClO_4$ concentrations, indicating sufficient time resolution to observe all initial scavenging kinetics. Within the range of concentrations examined, there are two dominant contributions to the decay. One is on a time scale of >1 ns, which exceeds the maximum time delay in the experiments and limits confidence in the quantitative values. However, the inclusion of a long time decay significantly improved the fits, and the decrease in time constant with scavenger concentration suggests bimolecular kinetics. A rough estimate for the second

order rate coefficient of $k = 1.7 \times 10^9$ $M^{-1} \cdot s^{-1}$ is obtained from the pseudo first order time constant of 1.7 ns at a concentration of 347 mM $HClO_4$. In comparison, a rate of $k = 8.6 \times 10^8$ $M^{-1} \cdot s^{-1}$ was measured for quenching with DQ in the same IL. [145]

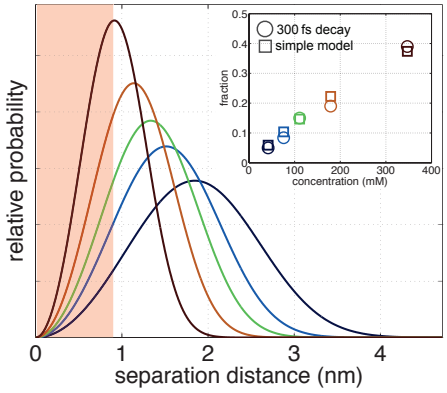

Figure 3.7: Probability distribution of nearest pairwise distances for a random distribution at the concentrations of the $HClO_4$ quencher used. The inset shows a comparison of the fraction of the distribution below 0.9 nm (squares), and the fraction of the quenching fit with the 300 fs decay component (circles), see Table 3.2.

The other dominant component in the fits is a 300 fs decay that increases in amplitude linearly with $HClO_4$ concentration, but without a measurable change in the time constant. The presence of fast quenching mechanism is consistent with the radiolysis study examining electron reactivity with DQ in $[Py^+_{1,4}][NTf^-_2]$. The radiolysis experiments had a concentration-dependent depletion of the initial electron population indicating that scavenging reactions were taking place faster than the 15 ps experimental time resolution. [145] The lack of an obvious dependence of the 300 fs time constant with respect to the quencher concentration demonstrates that this is not a diffusion-mediated, second-order process. The conclusion is that the reaction precedes

the majority of diffusion and reflects reactivity in the static, initial spatial distribution of electrons and scavengers.

The effective distance accessible to the sub-ps reaction can be estimated using a simple model. Figure 3.7 shows the radial distance distributions for the quencher concentrations employed, Eq. 3.1.

$$P(r) = \frac{3}{\gamma}\left(\frac{r}{\gamma}\right)^2 e^{-\left(\frac{r}{\gamma}\right)^3} \tag{3.1}$$

In Eq. 3.1, $\gamma = \left(\frac{3}{4\pi N}\right)^{1/3}$, N is the number density, r is the center-to-center distance between the closest points, and the points are assumed to be randomly distributed. We note that this model ignores the finite volume of the reactants. However, at the relatively low concentrations considered it should provide a reasonable estimation of the distributions. The fraction of the distributions below a fixed distance, representing a quenching radius, can be compared with the fraction of the measured decay accounted for by the 300 fs component, see Table 3.2. Minimizing the difference results in a value of $r = 0.9$ nm. The inset of Fig. 3.7 compares the fraction of the distribution at radius of $r > 0.9$ nm to the sub-ps fraction of the measured decay. Given the simplicity of this static model, the agreement is quite good.

Reaction of all electrons within roughly 0.9 nm of a quencher occurs in less than 1 ps, and the subsequent pause in quenching, until onset of the much slower diffusion-mediated bimolecular reaction, indicates a mechanism analogous to that discussed for geminate recombination. The initially photodetached dry electrons are highly reactive,

delocalized, and mobile. These electrons have a significant reactive radius, however sub-ps solvation localizes the electrons and quickly reduce their reactivity. Independence of the reaction rate with concentration is often associated with tunneling [90, 145], and tunneling certainly may contribute to the quenching reactions in this case. However, the rate of tunneling depends on distance. That dependence should be reflected in a slowing of the rate as the reaction proceeds and the reactant density declines. Within the experimental signal-to-noise the measurements do not show evidence for such behavior. The decays are well fitted by a single exponential. This indicates that fast deactivation of the electron reactivity via solvation, a rate that appears independent of quencher concentration under the conditions reported here, plays a significant role in controlling even the fastest quenching dynamics. To illustrate how solvation mediated reactivity can lead to the appearance of both a linear increase in amplitude and independence of the rate with increasing acid concentration, we model the quenching reaction as a bimolecular process with a time-dependent rate coefficient.

$$e^- + H^+ \xrightarrow{k(t)} H\cdot \tag{3.2}$$

Solvation dynamics are typically multifaceted, with the fastest nuclear reorganization associated with inertial motions that are often modeled as Gaussian in time. [103] However, experiments are seldom sensitive enough to distinguish between a Gaussian and exponential form for the ultrafast solvation, and that is true of the data presented here. For convenience we adopt an exponential form for the initial influence of solvation on

the rate.

$$k(t) = k_{\mathrm{dry}}\, e^{(-t/\tau_{\mathrm{sol}})} \tag{3.3}$$

The rate coefficient at $t = 0$ is k_{dry} and the time constant associated with the solvent's influence on reactivity is τ_{sol}. Assuming this process is first-order in each of the reactants, the differential quenching rate is expressed as

$$\frac{d[\mathrm{e}^-]}{dt} = -\left(k_{\mathrm{dry}}\, e^{(-t/\tau_{\mathrm{sol}})}\right)\ [\mathrm{e}^-][\mathrm{H}^+]. \tag{3.4}$$

The brackets indicate concentration. An upper limit of $[\mathrm{e}^-] = 0.06$ mM results from the assumption that every absorbed 266 nm pump photon at 1.1 TW/cm^2 creates a free electron. For all quenching conditions considered in this study $[\mathrm{H}^+] \gg [\mathrm{e}^-]$ and we approximate $[\mathrm{H}^+]$ as time-independent. Integrating Eq. 3.4 under these conditions,

$$\frac{[\mathrm{e}^-]}{[\mathrm{e}^-]_0} = \exp\left\{-k_{\mathrm{dry}}\tau_{\mathrm{sol}}[\mathrm{H}^+]\left(1 - e^{(-t/\tau_{\mathrm{sol}})}\right)\right\}. \tag{3.5}$$

The electron concentration at $t = 0$ is $[\mathrm{e}^-]_0$. In the limit that the argument is small, $k_{\mathrm{dry}}\tau_{\mathrm{sol}}[\mathrm{H}^+] \ll 1$, the amplitude of the decay in electron concentration is linear in $[\mathrm{H}^+]$ and the rate depends only on the solvation time constant. This is illustrated by expanding the exponential in a power series.

$$\frac{[\mathrm{e}^-]}{[\mathrm{e}^-]_0} = 1 - k_{\mathrm{dry}}\tau_{\mathrm{sol}}[\mathrm{H}^+]\left(1 - e^{(-t/\tau_{\mathrm{sol}})}\right) + \cdots \tag{3.6}$$

In Fig. 3.8(c) the value of Eq. 3.5 at long time, $\frac{[\mathrm{e}^-]}{[\mathrm{e}^-]_0} \overset{t\to\infty}{\longrightarrow} \exp\left\{-k_{\mathrm{dry}}\tau_{\mathrm{sol}}[\mathrm{H}^+]\right\}$, is compared with the residual amplitude of the fastest quenching component in Table 3.2, $(1 - a_1)$. The time constant was fixed at $\tau_{\mathrm{sol}} = 300$ fs and the value of k_{dry} was adjusted

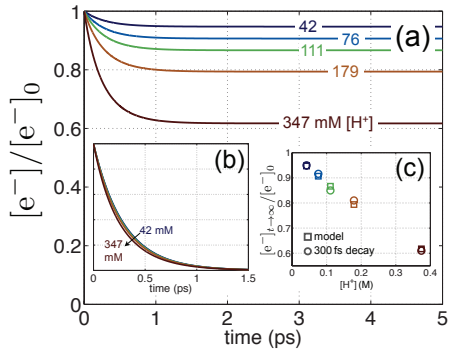

Figure 3.8: Plots of Eq. 3.5 with $\tau_{sol} = 300$ fs, $k_{dry} = 4.3 \times 10^{12}$ M^{-1} s^{-1} and the indicated proton concentration. **(b)** A comparison of the decays in **(a)** for all values of $[H^+]$ after subtraction of the offset at large delay times and scaling to the same initial value. **(c)** Comparison of the quenching at long time in Eq. 3.5 and the residual amplitude of the fastest quenching component determined from the fits to the data, (1 – a_1), see Table 3.2.

to minimize the difference between Eq. 3.5 and residual amplitude of the fit to the data. Fig. 3.8(a) shows the resulting time dependence of Eq. 3.5 for all values of $[H^+]$ and the optimized value of $k_{dry} = 4.3 \times 10^{12}$ $M^{-1} \cdot s^{-1}$. At the highest acid concentration investigated $k_{dry}\tau_{sol}[H^+] = 0.45$, placing a limit on the accuracy of approximating Eq. 3.5 by truncating Eq. 3.6 at first-order. However, as shown in Figs. 3.8(b) and 3.8(c), within the broad range of acid concentrations investigated, the full expression, Eq. 3.5, demonstrates very little influence of $[H^+]$ on the decay rate and very little deviation from a linear dependence of the quenching amplitude on $[H^+]$. The deviations are quite small and beyond the quality of our data to elucidate. As a result, the measured rates appear independent of quencher concentration while the quenching amplitude appears linear in the quencher concentration.

Although our discussion has focused on the initial, fastest quenching component, the

solvent mediated reactivity will extend to the subsequent, slower solvation time scales. There is some limited evidence for this in the data at the two highest quencher concentrations. At these concentrations, an additional ∼8 ps decay emerges from the noise and has an amplitude that increases with quencher concentration, see Table 3.2. Compared with more common solvents, the dilation of solvation time scales that precede diffusion should extend this effect even further in RTILs, and may offer an explanation for the observation by Wishart *et al.* of a 1.3×10^{10} s^{-1} quenching rate that was independent of quencher concentration. [145]

3.5 Conclusion

Following photodetachment of $[Py^{+}_{1,4}][NTf^{-}_{2}]$, the TA spectrum at wavelengths shorter than 1000 nm was shown to be a combination of absorption from the electron and the hole. Spectrally resolved quenching revealed a bimodal shape for the hole spectrum in agreement with recent computational predictions on a smaller aliphatic RTIL. [86] The spectral evolution qualitatively agrees with previous radiolysis studies [145], and differences in the shape reflected the lower energy ionization in photolysis. Both quenching and geminate recombination dynamics demonstrate that significant reactivity is lost in less than a picosecond. These results extend previous observations correlating solvation and trapping of the electron with its reactivity to much shorter time scales. [145] The higher time resolution available from photolysis shows that the dry excess electron is significantly more reactive than previously measured, with the rate coefficient

for reaction with a proton scavenger falling rapidly in the first picosecond. Analogous experiments covering TA at wavelengths longer than 1000 nm, probing the complete primary absorption band of the electron, are needed to quantitatively disentangle the complex coupling between relaxation and reactivity of the electron on ultrafast time scales. These experiments are being pursued presently.

Chapter 4

Photodetachment and electron cooling in a series of neat aliphatic RTILs: $[\mathbf{Py}^+_{1,3}][\mathbf{NTf}^-_2]$, $[\mathbf{Py}^+_{1,6}][\mathbf{NTf}^-_2]$ and $[\mathbf{Py}^+_{1,10}][\mathbf{NTf}^-_2]$

4.1 Introduction

Here we have investigated a series of methyl-alkyl-pyrrolidinium bis(trifluoromethylsulfonyl)amides, structures presented in Fig. 4.1 and abbreviated in what follows as $[\mathrm{Py}^+_{1,x}][\mathrm{NTf}^-_2]$ with the x indicating the chain length of the n-alkyl group. Previously we have investigated the photodetachment and subsequent dynamics of electrons in neat $[\mathrm{Py}^+_{1,4}][\mathrm{NTf}^-_2]$. [91]

Electron detachment was effected by a 266 nm laser pulse (4.6 eV), and a linear dependence of the signal on the detachment laser irradiance indicated that the signals were due to single photon absorption. The induced TA was in good agreement with those previously reported for a species assigned to the solvated electron in radiolysis experiments. Addition of an electron scavenger reduced the magnitude of the induced absorption, and the relative quenching at different wavelengths was consistent with the computationally predicted spectral signatures of the residual hole. [86] However, as part of our ongoing efforts to purify these RTILs we discovered that the optical absorption of neat $[Py^+_{1,x}][NTf^-_2]$, including $[Py^+_{1,4}][NTf^-_2]$, begins deeper in the UV than previously reported. This finding has prompted us to investigate photodetachment at higher detachment energies.

Here we report the dynamics following photolysis at 6.20 eV (200 nm) of a series of methyl-alkyl-pyrrolidinium bis(trifluoromethylsulfonyl)amide liquids of high optical purity, with the alkyl chain increasing in length from *n*-propyl to *n*-decyl. Evidence is presented for branching between localization of the detached electron on the NTf^-_2 anion followed by rapid dissociation, and solvation of a free, solvated, detached electron with a long lifetime. As the length of the alkyl chain on the cation increases, experimental and computational evidence suggests that there is an increasing degree of nanostructuring in the form of polarity ordering, *i.e.* the appearance of regions where the alkyl chains accumulate. [66, 110] By spanning a range of increasing local structure in the liquid, the effects of structure on the nature and dynamics of solvated electrons are probed.

4.2 Experimental

Ionic Liquid Samples: The three liquids used in this study, methyl-alkyl-pyrrolidinium bis(trifluoromethylsulfonyl)amides with alkyl = *n*-propyl, *n*-hexyl, and *n*-decyl, were prepared Gary Baker [61]. To further purify the samples, the neat liquids were continuously stirred with 3% w/w activated carbon (Aldrich, DARCO (R)) overnight at room temperature *without* any solvent added. The thick black slurries were filtered through a fritted gas filter (ChemGlass, Fine) under vacuum, and this procedure was repeated 3 times. Although the liquids appeared colorless prior to the cleaning procedure, each cleaning cycle reduced absorption of the liquids for $\lambda > 205$ nm, with the most dramatic reduction in the first cleaning cycle. The cleaned liquids were stirred for 6 days in a sand bath at 70 °C – 80 °C under vacuum. The vacuum was filled with dry nitrogen and the samples were sealed and stored in a glove box.

Sample Handling: As previously reported, the samples must be continuously translated in order to avoid accumulation of photoproducts. [91] In our prior work on $[Py^+_{1,4}][NTf^-_2]$ this was accomplished using a sealed flow system. However, the higher viscosities of the $[Py^+_{1,6}][NTf^-_2]$ and $[Py^+_{1,10}][NTf^-_2]$ samples prevented flowing the sample at a high enough rate, in addition to the challenges of working with small available sample volumes. In order to address these issues, sealed sample cells that could be simultaneously rotated and translated were fabricated in house. The cells consisted of

two fused silica windows (1.00 mm thick, 50.8 mm diameter. Sydor, Corning 7980) separated by a PTFE ring (OD 50 mm, ID 45 mm, thickness 1.6 mm) in which two holes (1.25 mm diameter) were drilled along the radial direction separated by 5 mm. The holes were capped with stainless steel screws. The PTFE spacer and windows were pressed together between two aluminum rings that were connected by 8 screws. Between each aluminum ring and window a Tygon O-ring (1.5 mm thick) was placed to help homogenize pressure on the fused silica windows. The sample cells were kept in an oven at 45 °C overnight with the access ports open and subsequently introduced into the glove box. For each experiment 2 mL of the RTIL sample was syringed into the cell, the two stainless steel screws were inserted to seal the cell, and the cell was removed from the glove box. Electron scavenging experiments were performed by saturating the RTILs with N_2O by bubbling N_2O through the RTILs via the access ports in the cell for 40 mins. During experiments the cell was continuously rotated at 300 rpm and simultaneously translated back and forth perpendicular to the laser propagation at a speed of speed of 1 mm/s with an amplitude of 8 mm. Translation of the sample was required to avoid rapid buildup of photoproducts as we have demonstrated previously. [91]

Laser System: Our home-built regeneratively amplified Ti:sapphire laser produces 1.1 mJ, 70 fs pulses at 1 kHz with wavelength centered at 800 nm. A fraction of this light is converted into its third harmonic using an inline system. The 266 nm light is isolated using three dielectic mirrors and combined with the 800 nm fundamental in a Type I $\beta-$barium borate crystal (0.1 mm thickness, NewLight). The resulting 200 nm (6.20

eV) excitation pulses were focused to a spot size of 450 μm ($1/e$) at the sample using an aluminum off-axis parabolic mirror. The pump power was controlled by means of a waveplate–polarizer pair at the entrance of the THG system. Supercontinuum probe light was generated by focusing the remaining fraction of the original 800 nm fundamental in a 2 mm sapphire plate and collimated with an aluminum off-axis parabolic mirror.

The continuum probe light was treated differently depending on whether the near-infrared (0.92 eV – 1.38 eV, 900 nm – 1350 nm) or the visible (1.26 eV – 2.76 eV, 450 nm – 980 nm) portion of the light was being detected. In the case of near-IR detection, the continuum was sent through a long-pass filter (FGL1000, Thorlabs) to remove the visible components and excess fundamental, and to flatten the spectrum. For visible detection, the collimated beam was sent through a prism line to compensate for chirp and to allow filtering of the 800 nm driving field by placing a metal light block in the spectrally dispersed light. In both cases, the probe light was focused in the sample to a spot size of 50 μm ($1/e$) and crossed with the pump light. The near-IR and visible data sets were collected one immediately after the other on the same sample. For the experiments in the visible region, the transmitted probe light was dispersed with a grating (150 lines/mm, 500 nm blaze) and detected using a 256 linear pixel silicon diode array (Hamamatsu S3901-256Q). For the near-IR experiments, the transmitted probe light was dispersed with a grating (150 lines/mm, 1.2 μm blaze) and detected with a 256 linear pixel InGaAs diode array (Hamamatsu G9213-256S). In all cases, the probe

spectrum was collected for each individual probe pulse. The pump light was modulated at half the laser repetition rate, 500 Hz, and the change in optical density (ΔOD) with and without the pump pulse present was determined for every pair of probe pulses. The cross-correlation between the pump and probe light was 240 fs (Gaussian, FWHM).

4.3 Results

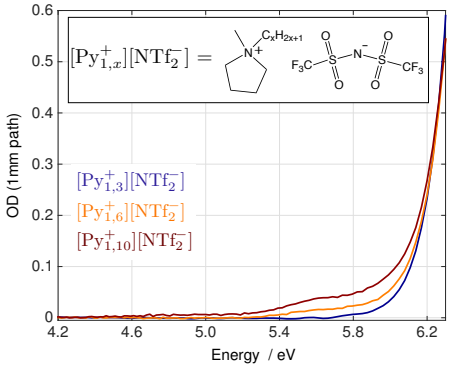

Figure 4.1: Absorption spectrum and structure of the neat $[Py^+_{1,3}][NTf^-_2]$, $[Py^+_{1,6}][NTf^-_2]$ and $[Py^+_{1,10}][NTf^-_2]$.

Absorption spectra of the purified RTIL samples are presented in Fig. 4.1. The cleaning procedure described above resulted in a substantial decline of the absorption at energies lower than 6.05 eV (205 nm), and near elimination of the absorption at energies lower than 5.17 eV (240 nm). All three liquids have a strong absorption band with an onset around 5.90 eV (210 nm). The $[Py^+_{1,6}][NTf^-_2]$ and $[Py^+_{1,10}][NTf^-_2]$ samples have a small shoulder peaked near 5.64 eV (220 nm) that increases intensity with n-alkyl chain length and is absent in the $[Py^+_{1,3}][NTf^-_2]$ liquid. In all of the experimental results

presented below, the liquids were excited at 6.2 eV (200 nm). Absorption at 6.2 eV is within the first major absorption band, and the molar absorptivities of the three liquids are 0.67 M^{-1} cm^{-1} , 1.0 M^{-1} cm^{-1} and 1.1 M^{-1} cm^{-1} for $[Py^{+}_{1,3}][NTf^{-}_{2}]$, $[Py^{+}_{1,6}][NTf^{-}_{2}]$, and $[Py^{+}_{1,10}][NTf^{-}_{2}]$ respectively.

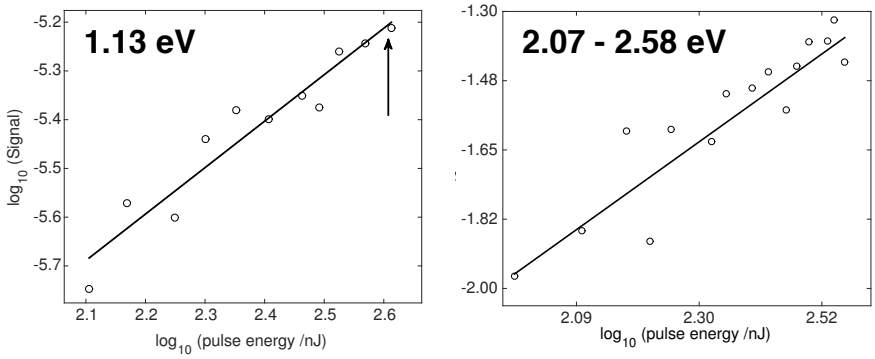

Figure 4.2: Power dependence of the TA in $[Py^{+}_{1,3}][NTf^{-}_{2}]$ at a probe delay of 50 ps and probe energies 1.13 eV and 2.07–2.58 eV. The circles are the data and the solid line is a linear fit. At 1.13 eV the slope is 0.95±0.17 and at 2.07–2.58 eV the slope is 1.01±0.11

The dependence of the TA signal on the laser irradiance was measured for a range of pump pulse energies covering 100 nJ to 500 nJ and found to be consistent with single photon absorption of the pump at 6.2 eV. Figure 4.2 presents the log-log plot of the signal intensity vs. pump pulse energy for $[Py^{+}_{1,3}][NTf^{-}_{2}]$ at a probe energy of 1.13 eV and a probe delay time of 50 ps, which was fitted to a line with a slope of 0.95±0.17. Within the signal to noise of the data, the TA spectra did not change shape with increasing pump pulse energy. In the VIS, between 2.07–2.58 eV, the slope is also very close to 1, thus also indicating that the TA there are due to the absorption of a single photon.

For all of the other pump-probe experiments reported here, the 6.2 eV pump pulse

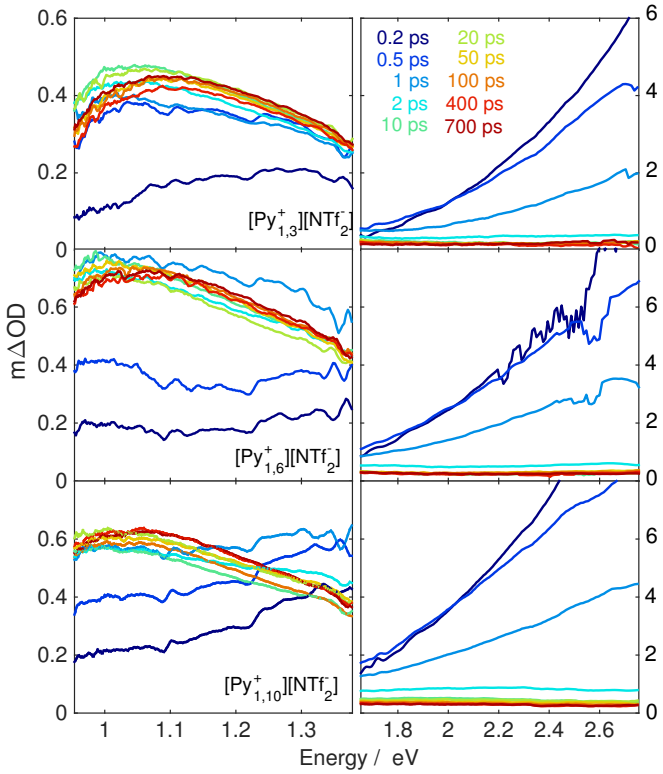

Figure 4.3: Transient absorption of the three RTILs following excitation at 6.20 eV. Note that the ΔOD axis in the near-IR probe range is ten times smaller than in the visible probe range.

was set to 450 nJ at the sample, which under our experimental conditions corresponds to an irradiance of 1.2 GW/cm^2. Pump-probe spectra at a series of delay times for each of the three RTILs are presented in Fig. 4.3. All of the observed changes in optical density were positive and assigned to transient absorption (TA). Upon 6.20 eV excitation, the three samples produced qualitatively similar TA. The following main features are shared by the three liquids: (*i*) an early and very large TA that covers our VIS window (from 450 nm to 750 nm) and even leaks into the NIR at early times; (*ii*) a delayed sub-ps

growth of the NIR TA, followed by marked blue shift; and (*iii*) a slower decay of the TA in the VIS. There are however clear quantitative differences in the evolution of the transients, and it is from these differences that we want to extract information about the dynamics of the ejected electron in this set of ILs.

Figure 4.4 shows the normalized kinetic traces at individual probe energies for the three RTILs. The traces are fitted to sequential scheme of first order processes given by Eq. 4.1 (for the case of two steps):

$$a(t)S_a \xrightarrow{k_1} b(t)S_b \xrightarrow{k_2} c(t)S_c \tag{4.1}$$

The time dependent coefficients, $a - c$, are restricted to sum to 1, and $a = 1$ when $t = 0$. Signal values are represented by S_{a-c}, and the initial signal was set to zero, $S_a = 0$. Equation 4.1 was convoluted with the instrument response. The first-order rate coefficients, k_1 and k_2, and the signal values, S_b and S_c, were varied to minimize the difference between the data and fits. The same applies to the fits with three steps. The optimized fitting parameters are detailed in Tables 4.1, 4.2 and 4.3.

In the visible portion of the spectrum there was a strong, broad TA that appeared very rapidly, rose with a <100 fs time constant, and increased in amplitude with probe energy. Decay of this feature had a time constant of ∼0.7 ps at a probe energy of 2.48 eV, see Fig. 4.5 and Table 4.4. Following the sub-ps decay there was a small residual signal of ∼3% of the maximum value that had a lifetime exceeding the maximum experimentally probed time delay. The optimized fitting parameters are listed in Table 4.4. Although the initial rise was fitted to time constants that were less than the instrument response,

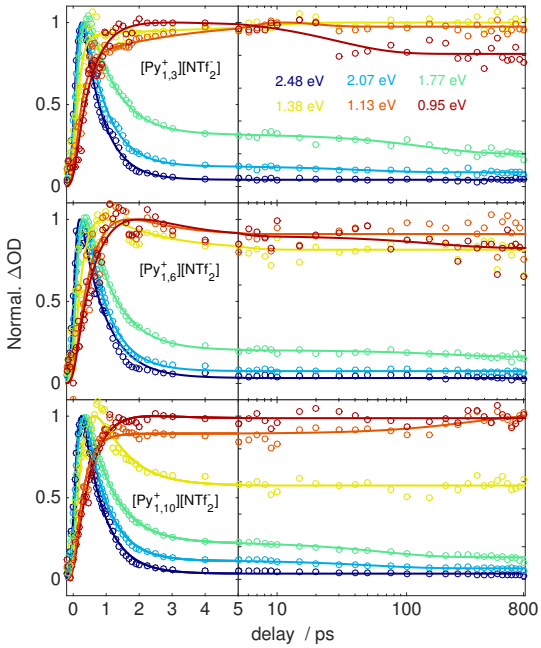

Figure 4.4: TA at selected probe energies. Open circles are the raw data and the lines are the fits using Eq. 4.1. Optimized fitting parameters are listed in Tables 4.1, 4.2, and 4.3.

the fits were improved (statistically significant reduction in the difference between the data and the fits) with the inclusion of a finite time constant for the rise when compared with optimized fits that restricted the rise to be instantaneous ($k_1 \to \infty$).

In the near-IR demonstrated a rapid, on the other hand, there is a rapid yet resolvable sub-ps initial rise. Figure 4.6 presents the TA intensity integrated over the probe energy range of 0.95–1.38 eV. The data were fitted to a single exponential rise with optimized time constant in the range of 0.4–0.6 ps for the three liquids, Table 4.5. There was no evidence for decay of the broad absorption in the near-IR on the experimentally probed time scale of 850 ps.

Probe (eV)	$1/k_1$ (ps)	S_b	$1/k_2$ (ps)	S_c	$1/k_3$ (ps)	S_d
2.48	0.07 (0.064–0.072)	1.55 (1.52–1.57)	0.62 (0.61–0.64)	0.04 (0.041–0.048)		
2.07	0.098 (0.092–0.103)	1.52 (1.49–1.55)	0.67 (0.64–0.69)	0.130 (0.120–0.139)	45 (6.3–86)	0.091 (0.083–0.095)
1.77	0.154 (0.146–0.162)	1.31 (1.28–1.34)	0.819 (0.779–0.860)	0.2937 (0.286–0.301)	139 (92–177)	0.184 (0.182–0.186)
1.38	0.14 (0.12–0.16)	0.74 (0.72–0.76)	5.9 (-1.3–13)	0.80 (0.79–0.81)		
1.13	0.23 (0.19–0.27)	0.71 (0.65–0.78)	1.86 (0.95–2.8)	0.91 (0.90–0.92)		
0.95	0.52 (0.49–0.55)	0.98 (0.96–1.00)	29 (17–41)	0.78 (0.76–0.79)		

Table 4.1: Optimized fitting parameters for equation 4.1 to the data in Fig. 4.4 for $[Py^{+}_{1,3}][NTf^{-}_{2}]$. Error bounds are presented as the 68% confidence interval when all parameters were simultaneously optimized.

Evolution of the maximum in the near-IR TA band is presented in Fig. 4.7, where the TA spectra have been normalized to the same maximum value and the region around the maxima has been isolated. To determine the energy at the maximum in the TA, $E_{\max}$, the spectra were fitted with a third-order polynomial. In Fig. 4.8 the determined $E_{\max}$ values are plotted as a function of probe delay time. Spectra at probe delays less than 2 ps were not included in the analysis due to the lack of a clearly defined maximum, see Fig. 4.3, and concerns about the potential for contamination from the tail of the much larger absorption feature in the visible portion of the spectrum that is broad and decays with a sub-ps time constant. Time dependence of the $E_{\max}$ values were fitted with a time independent offset to represent the initial value at a delay of 2 ps and a single exponential rise. The optimized fitting parameters are listed in Table 4.6 as a function of probe delay time there was an increase in $E_{\max}$. With increasing alkyl chain length the $E_{\max}$ values decreased and the rate of spectral diffusion slowed. The total shift

Probe (eV)	$1/k_1$ (ps)	S_b	$1/k_2$ (ps)	S_c	$1/k_1$ (ps)	S_d
2.48	0.022 (0.012–0.031)	1.37 (1.33–1.41)	0.76 (0.72–0.80)	0.034 (0.025–0.044)		
2.07	0.11 (0.105– 0.115)	1.57 (1.55– 1.60)	0.69 (0.67–0.71)	0.079 (0.075–0.083)		
1.77	0.128 (0.123– 0.134)	1.37 (1.35–1.40)	0.86 (0.830–0.885)	0.199 (39–395)	217 (40–295)	0.157 (0.147– 0.168)
1.38	0.250 (0.193– 0.317)	0.86 (0.76– 0.96)	1.76 (0.56– 2.96)	0.62 (0.60– 0.64)		
1.13	0.78 (-34517–34518)	1.19 (-52587–52589)	0.78 (-34515–34517)	0.64 (0.63– 0.66)		
0.95	1.04 (-30903–30905)	1.54 (-45508–45511)	1.04 (-30903–30905)	0.71 (0.70– 0.73)		

Table 4.2: Optimized fitting parameters for equation 4.1 to the data in Fig. 4.4 for $[Py^+_{1,6}][NTf^-_2]$. Error bounds are presented as the 68% confidence interval when all parameters were simultaneously optimized.

between 2 ps and 850 ps was smaller in $[Py^+_{1,3}][NTf^-_2]$, 0.054 eV, than in $[Py^+_{1,6}][NTf^-_2]$ and $[Py^+_{1,10}][NTf^-_2]$, 0.76 eV and 0.74 eV respectively. In addition to shifting in energy, the broad spectra also narrowed with increasing probe time delay and with a reduction in the alkyl chain length. The width of the near-IR absorption was characterized by determining the square root of the second moment (standard deviation) between 0.95 eV and 1.38 eV, and this is presented as a function of probe delay time in Fig. S2 and Table S4.

The spectral evolution of the near-IR TA is more complex than a shift of the band, and it is difficult to describe the complete behavior of the TA from the observation of a window that does not contain the full transient. Additional to the shift of the band to higher energies, there is also an evolution in the shape of the TA. As a rough measure of this we use the square root of the second moment, RMSD, of the TA between 0.95 eV and 1.38 eV. In Figure 4.9 this RMSD is plotted for the three liquids and fitted to the

Probe (eV)	$1/k_1$ (ps)	S_b	$1/k_2$ (ps)	S_c	$1/k_3$ (ps)	S_d
2.48	0.062 (0.057–0.064)	1.51 (1.49–1.53)	0.66 (0.64–0.67)	0.036 (0.034–0.041)		
2.07	0.101 (0.097–0.106)	1.55 (1.52–1.58)	0.668 (0.645–0.690)	0.122 (0.114–0.130)	54 (21–87)	0.071 (0.066–0.077)
1.77	0.114 (0.109–0.118)	1.40 (1.38–1.42)	0.833 (0.806–0.859)	0.231 (0.223–0.238)	64 (45–82)	0.138 (0.134–0.143)
1.38	0.273 (0.218–0.328)	1.16 (1.01–1.30)	0.87 (0.66–1.09)	0.46 (0.45–0.47)		
1.13	0.309 (0.293–0.324)	0.85 (0.84–0.85)	316 (40–592)	0.96 (0.92–1.00)		
0.95	0.71 (-28476–28477)	1.23 (-49252–49255)	0.71 (-28475–28476)	0.87 (0.87–0.88)		

Table 4.3: Optimized fitting parameters for equation 4.1 to the data in Fig. 4.4 for $[Py^+_{1,10}][NTf^-_2]$. Error bounds are presented as the 68% confidence interval when all parameters were simultaneously optimized.

RTIL	$1/k_1$ (ps)	S_b	$1/k_2$ (ps)	S_c
$[Py^+_{1,3}][NTf^-_2]$	0.069 (0.064–0.072)	1.50 (1.48–1.52)	0.62 (0.61–0.64)	0.043 (0.039–0.047)
$[Py^+_{1,6}][NTf^-_2]$	0.022 (0.012–0.031)	1.37 (1.33–1.41)	0.76 (0.72–0.80)	0.034 (0.025–0.044)
$[Py^+_{1,10}][NTf^-_2]$	0.061 (0.057–0.063)	1.47 (1.45–1.49)	0.66 (0.64–0.69)	0.036 (0.033–0.039)

Table 4.4: Optimized fitting parameters for TA at 2.48 eV, presented in Fig. 4.5. Parameters are defined in Eq. 4.1. Error bounds are presented as the 68% confidence interval when all parameters were simultaneously optimized.

sum of two exponential decays. It is clear from the figure that the width of the near-IR band increases with the size of the cation, and that there is a narrowing of the bands as time progresses. See Table 4.7 for the optimized fitting parameters. The RMSD in all three liquids demonstrates a bimodal decay with time, with an initial time constant of a few ps followed by a much slower decay that our fits place very roughly around 100 ns. This time constant is too large for us to determine with any accuracy given the maximum time delay of 850 ps probed in the experiments, however the addition of a slow step clearly improve the quality of the fits.

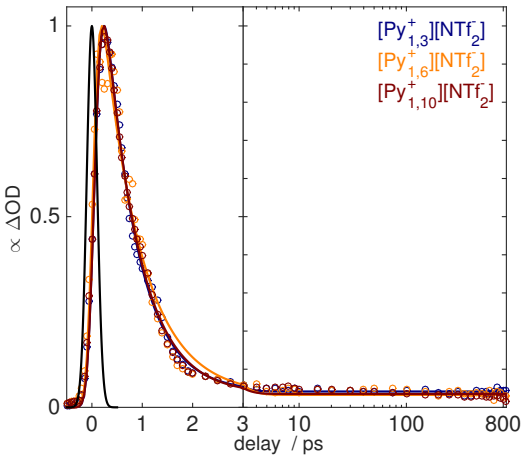

Figure 4.5: Transient absorption at a probe energy of 2.48 eV following excitation at 6.20 eV. The circles are the data and the solid lines are the fits using Eq. 4.1. The black line is the instrument response. Optimized fitting parameters are listed in Table 4.4.

RTIL	τ (ps)
$[Py^+_{1,3}][NTf_2^-]$	0.38 (0.34–0.42)
$[Py^+_{1,6}][NTf_2^-]$	0.56 (0.47–0.65)
$[Py^+_{1,10}][NTf_2^-]$	0.40 (0.38–0.43)

Table 4.5: Optimized time constants determined by fitting a single exponential rise, $S(t) = 1 - e^{-t/\tau}$, to the integrated near-IR TA data presented in Fig. 4.6. Error bounds are presented as the 68% confidence interval.

All of the TA measurements were repeated after the RTILs were saturated with the electron scavenger N_2O. The fraction of TA signal in the absence of N_2O that remained was determined in order to isolate the influence of the N_2O scavenger. Using available data for similar RTILs we roughly estimate the saturated concentration of N_2O at room temperature at 90 mM. Only an estimation is possible given that the Henry constant for this gas has been measured in only a small number ionic liquids which does not

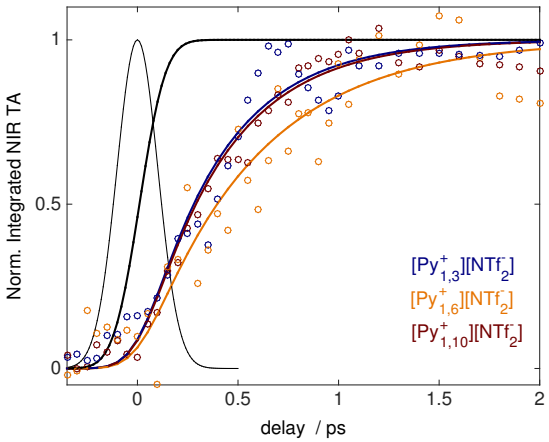

Figure 4.6: Integrated TA in probe energy range 0.95–1.38 eV up to a delay of 2 ps. The open circles are the data and the solid lines are optimized fits to a single exponential rise convoluted over the instrument response function. Time constants are listed in Table 4.5. The instrument response is shown with the thin black line and the thick black line presents a Heaviside function convoluted with the instrument response for comparison.

include those used in these experiments. Assuming that its value does not differ greatly from that in $[\text{bmim}^+][\text{NTf}_2^-]$ (the values for O_2 and CO_2 are within $\approx 15\%$ of each other in $[\text{bmim}^+][\text{NTf}_2^-]$ and $[\text{Py}_{1,4}^+][\text{NTf}_2^-]$), [6] and that they are the roughly the same for $[\text{Py}_{1,4}^+][\text{NTf}_2^-]$ as for $[\text{Py}_{1,3}^+][\text{NTf}_2^-]$, $[\text{Py}_{1,6}^+][\text{NTf}_2^-]$ and $[\text{Py}_{1,10}^+][\text{NTf}_2^-]$, we obtain a N_2O saturation concentration of 90 mM.

The complete quenching results are shown in the Appendix section, and here we show only those that play an important role in the discussion. The N_2O scavenger had a much larger effect on the TA in the near-IR than the visible, Fig. 4.10. In the visible region reduction of the TA due to N_2O was small. In contrast, the near-IR TA was reduced in amplitude by more than 50% in less than 3 ps. Decay in the near-IR TA due to saturation with N_2O was fitted to the sum of two exponentials, and the optimized

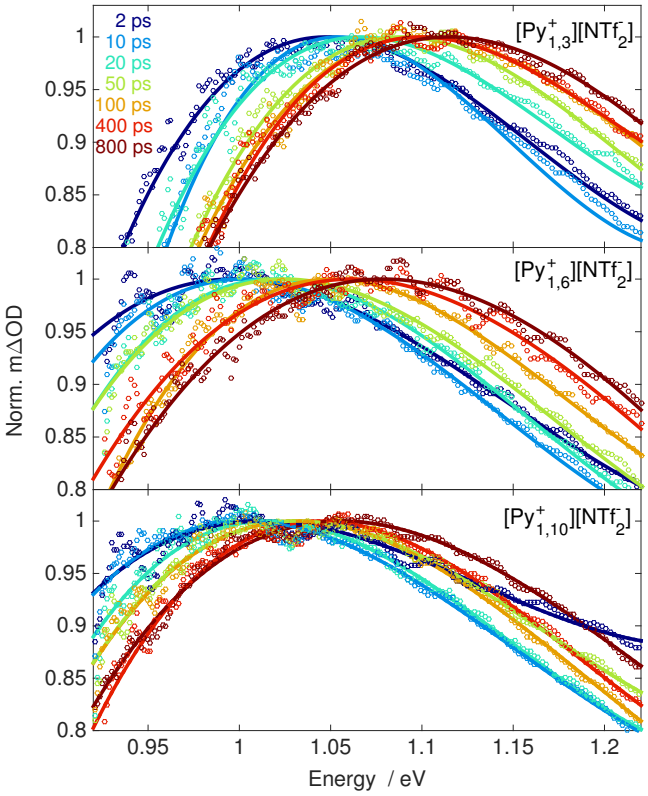

Figure 4.7: TA for the three RTILs scaled to the maximum value and fitted to determine the energy at the maximum TA intensity as a function of probe delay, which is plotted in Fig. 4.8. The open circles are the data and the solid lines are the third-order polynomial fits.

fitting parameters are listed in Table 4.8. Over half of the TA signal was quenched with a time constant of ∼0.5 ps, and although the quenching was statistically slightly faster in the $[Py^{+}_{1,3}][NTf^{-}_{2}]$, there was only a small difference between the ultrafast quenching rate in the three RTILs. After the initial sub-ps decay, the TA signals appeared to plateau and then subsequently decayed with a second time constant that exceeded the longest probe delay measured.

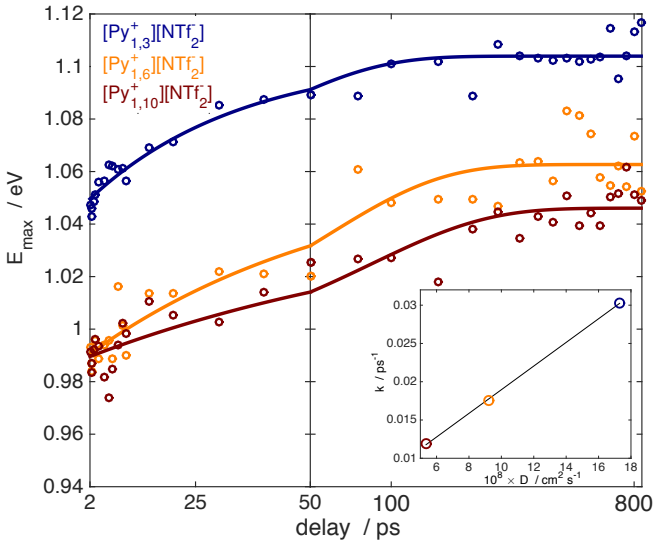

Figure 4.8: Evolution of the maximum in the near-IR TA as a function of delay time. Fitting to determine the value of $E_{\max}$ is presented in Fig. 4.7. The data were fitted to the sum of a time independent offset and a single exponential rise. Open circles are the data and the solid lines are the fits. Note that the time axis is linear from 2 to 50 ps and logarithmic from 50 to 850 ps. The fitting parameters are listed in Table 4.6. The inset is a plot of the resulting rate coefficients ($1/\tau$) against the Stokes-Einstein diffusion coefficients for the three RTILs.

4.4 Discussion

Light absorption in the neat RTILs. Absorption spectra of the RTILs, Fig. 4.1, had an onset of a large band around 5.8 eV. A small shoulder was present in the $[Py^+_{1,6}][NTf_2^-]$ and $[Py^+_{1,10}][NTf_2^-]$ peaked around 5.6 eV. Shape of the large band agrees with the computational prediction by Xu *et al.* for the HOMO–LUMO transition in the analogous $[Py^+_{1,4}][NTf_2^-]$ liquid. [148] The computational prediction indicated onset of this band at a lower energy (∼5.0 eV), however, as the authors explained, this underestimation of the HOMO–LUMO gap is expected as a result of employing a generalized gradient

RTIL	H (eV)	τ (ps)	A (eV)
$[Py^+_{1,3}][NTf^-_2]$	1.046 (1.044–1.049)	33 (28–38)	0.058 (0.055–0.061)
$[Py^+_{1,6}][NTf^-_2]$	0.988 (0.984–0.992)	57 (45–68)	0.075 (0.071–0.079)
$[Py^+_{1,10}][NTf^-_2]$	0.988 (0.986–0.991)	84 (66–102)	0.058 (0.046–0.061)

Table 4.6: Fitting parameters of the evolution of $E_{\max}$ presented in Fig. 4.8. Data for each liquid was fitted to $H + A(1 - e^{-t/\tau})$. Error bounds are presented as the 68% confidence interval when all parameters were simultaneously optimized.

RTIL	τ_a (ps)	A	τ_b (ns)	B
$[Py^+_{1,3}][NTf^-_2]$	7.0 (5.5–8.6)	0.0024 (0.0022–0.0025)	160 (101–217)	0.117 (0.117–0.117)
$[Py^+_{1,6}][NTf^-_2]$	22 (12–31)	0.0016 (0.0013–0.0018)	110 (67–151)	0.118 (0.118–0.118)
$[Py^+_{1,10}][NTf^-_2]$	7.4 (6.0–8.8)	0.0031 (0.0028–0.0033)	90 (68–107)	0.119 (0.119–0.119)

Table 4.7: Fitting parameters for the evolution of the standard deviation of the near-IR TA between 0.95 eV to 1.38 eV, shown in Fig. 4.9. The data was fitted to the sum of two exponential decays, $Ae^{-t/\tau_a} + Be^{-t/\tau_b}$. Error bounds are presented as the 68% confidence interval when all parameters were simultaneously optimized.

approximation. The shoulder around 5.6 eV in $[Py^+_{1,6}][NTf^-_2]$ and $[Py^+_{1,10}][NTf^-_2]$ was not apparent in $[Py^+_{1,3}][NTf^-_2]$, nor was a low energy shoulder predicted by Xu *et al.* in $[Py^+_{1,4}][NTf^-_2]$. Challenges associated with purifying RTILs always leave the potential for residual impurities, and this is one possible explanation for the low energy shoulder. However, absence of the shoulder in $[Py^+_{1,3}][NTf^-_2]$ following the cleaning procedure, and the fact that subsequent cleaning cycles had no measurable effect on any of the three spectra, suggests that the absorption shoulder found with the longer n-alkyl chains is inherent to the neat liquids. An alternative explanation for the absorption shoulder is a charge-transfer-to-solvent (CTTS) type transition associated with individual NTf^-_2

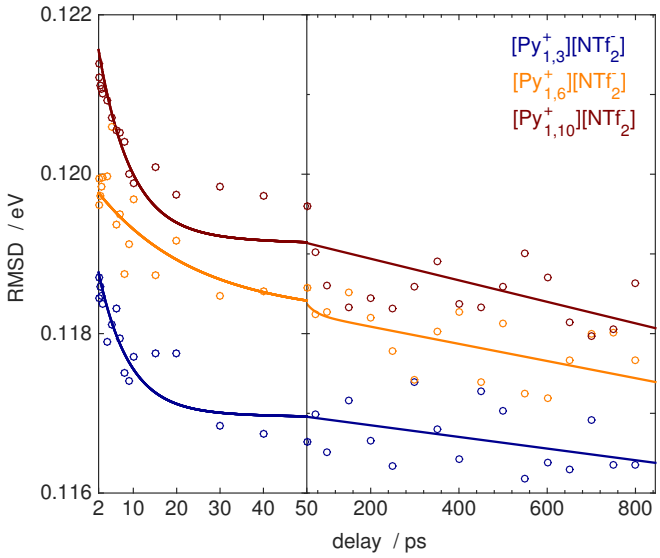

Figure 4.9: Time dependence of the width (rmsd) of the near-IR transient absorption band. Plotted is the standard deviation of the TA determined in the range 0.95 eV to 1.38 eV. The circles are the data and the solid lines are biexponential fits with the optimized fitting parameters listed in Table 4.7

anions. In Fig.4.11 the absorption of $LiNTf_2$ in acetonitrile is presented.

Solvated NTf_2^- absorption is peaked at 5.7 eV and has a width of ∼0.5 eV. Appearance of the CTTS transition for *n*-alkyl chains longer than propyl but shorter than hexyl correlates with predictions of the onset for polarity ordering in the RTILs. [66,110] Changes in the structure of the liquids on nanometer length scales with increasing *n*-alkyl chain length offers a possible explanation for the appearance and increasing amplitude of a CTTS transition in this homologous series.

All of the time resolved experiments presented in this study probed the dynamics after excitation at 6.20 eV. This energy is well above the onset of the HOMO–LUMO transition in the liquids [86], and assuming the width of the CTTS absorption is similar

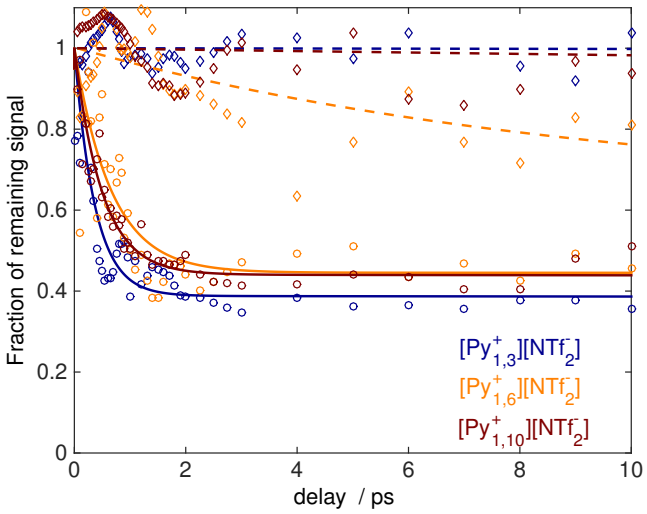

Figure 4.10: Fraction of the signal integrated over the near-IR probe region of 0.95–1.38 eV (circles) and the visible region of 2.07–2.58 eV (diamonds) remaining when the RTILs are saturated with the electron scavenger N_2O. The solid lines are biexponential decay fits and optimized fitting parameters are listed in Table 4.8.

to that found for $Li^+NTf_2^-$ in acetonitrile, at 6.20 eV there should be very little contribution from the CTTS absorption. A comparison between the absorption spectrum of potassium iodide and $[Py^+_{1,4}][NTf_2^-]$ iodide, Fig. 4.12, indicates identical absorption at 6.20 eV, excluding any significant absorption from individual $[Py^+_{1,4}][NTf_2^-]$ cations. We conclude that excitation at 6.20 eV is dominated by the HOMO–LUMO transition of the liquids described by Margulis and coworkers with the resulting excited state initially delocalized over more than one anion. [86, 148] Delocalization of the initially excited electron is supported by sub-ps electron scavenging in the presence of ∼90 mM N_2O, Fig. 4.10 and Table 4.8. The detached, excess electron concentration can be estimated from the amplitude of the TA in the near-IR. Assuming an absorptivity of 20,000

RTIL	τ_a (ps)	A	τ_b (ns)	B
$[Py^+_{1,3}][NTf^-_2]$	0.37 (0.31–0.42)	0.64 (0.55–0.68)	2.5 (1.8–3.1)	0.39 (0.38–0.40)
$[Py^+_{1,6}][NTf^-_2]$	0.66 (0.45–0.87)	0.55 (0.45–0.66)	13 (–20–47)	0.45 (0.41–0.48)
$[Py^+_{1,10}][NTf^-_2]$	0.50 (0.45–0.54)	0.56 (0.53–0.59)	2.5 (2.1–3.0)	0.44 (0.43–0.45)

Table 4.8: Fitting parameters for the fraction of remaining near-IR TA presented in Fig. 4.10. The data was fitted to the sum of two exponential decays, $S(t) = Ae^{-t/\tau_a} + Be^{-t/\tau_b}$. Error bounds are presented as the 68% confidence interval when all parameters were simultaneously optimized.

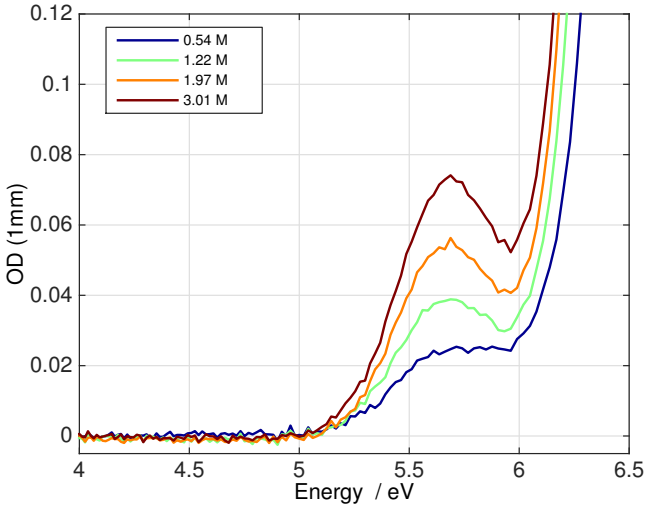

Figure 4.11: Absorption spectrum of $LiNTf_2$ in acetonitrile at several concentrations.

M^{-1} cm^{-1} at λ_{max} for the free electron based on reports in similar ionic liquids, [67,146] and accounting for the experimental geometry results in an estimated excess electron concentration of 0.3 μM. At these concentrations for the electron and scavenger, delocalization and substantial reactivity of the initially created, dry electron are necessary to explain the observed ultrafast quenching. [86, 91]

Origins of the TA signals. There are two prominent features in the TA following

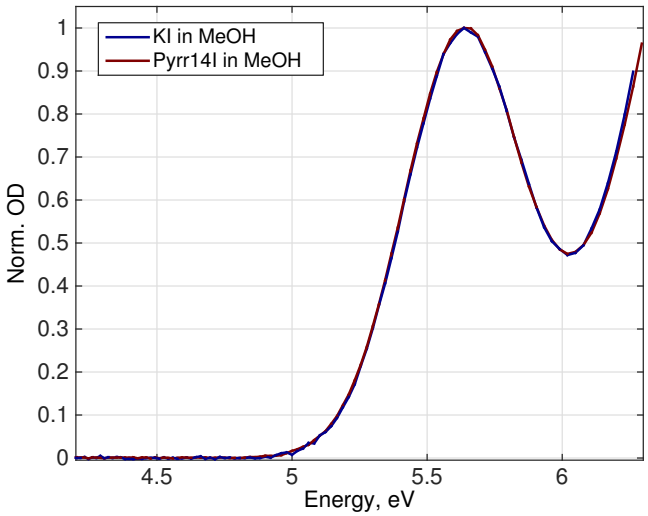

Figure 4.12: Normalized UV absorption spectrum of K^+I^- and Py_{14}^+ I^- in MeOH.

excitation at 6.20 eV in all three RTILs investigated. These are a strong broad absorption in the visible region of the spectrum with a sub-ps lifetime, and a weaker, broad absorption in the near-IR that has a sub-ps rise in intensity, exhibits spectral diffusion shifting to higher energy and narrowing of the absorption band on time scales of tens of ps, and presents no evidence of decay in intensity on the 850 ps time delay measured. At short delay times the N_2O electron scavenger has a very small effect on the visible TA, but results in a dramatic reduction of the near-IR TA suggesting the detached electron as the source. The dramatically different lifetimes and quenching behavior in the presence of N_2O indicate that the two absorption features do not originate from the same species. Absorption in the visible has been associated with the hole following electron detachment in analogous systems. [86, 91, 146] However, the hole has a >1 ns lifetime in the absence of any added hole scavengers, rather than the sub-ps lifetime of

the primary TA in the visible measured here. Dynamics of the visible TA are essentially indistinguishable between the different RTILs, Fig. 4.5, while there is a 50% increase in the ratio between the visible and near-IR TA features for $[Py^{+}_{1,10}][NTf^{-}_{2}]$ compared to the other two RTILs, Table 4.9. This suggests that the two signals do not represent a geminate pair with a common origin. Another possibility is that the species absorbing in the visible region is a precursor for the free electron that absorbs in the near-IR. However, rise in the near-IR TA is faster than decay of the visible TA, Tables 4.4 and 4.5. Taken together, the evidence indicates that the two TA features represent separate, competing outcomes following the initial HOMO–LUMO excitation at 6.20 eV.

Elaborated upon in the discussion that follows, absorption in the visible spectrum is consistent with recent simulations indicating absorption from a short-lived associated ion pair following dissociation of the NTf_2^{2-} dianion. [148] Absorption in the near-IR is consistent with previous radiolysis experiments in a wide range of liquids and is assigned to a long-lived free solvated electron. [74, 92, 145, 146] Branching between the two channels cannot be quantified in the absence of a known absorption cross-section for the dissociated anion pair. Different RTILs were measured on different days, and issues such as alignment and crossing of the pump and probe lasers could affect quantitative comparisons of individual signal amplitudes between different samples. However, the visible and near-IR portions of the spectrum for a single liquid were collected back-to-back without changes in the alignment and this allows comparison of the relative branching between the two channels as a function of the *n*-alkyl chain length on the

cation. The visible component is taken to be proportional to ΔOD at 2.58 eV and a probe delay of 200 fs, and the amplitude of the near-IR component is taken to be proportional to the maximum ΔOD in the near-IR at an average probe delay of 700 ps. Ratios of the two signals in the RTILs are listed in Table 4.9. There is greater partitioning to the dissociative NTf_2^{2-} dianion channel in $[Py^+_{1,10}][NTf_2^-]$ compared with the smaller *n*-alkyl chains, and this correlated with the predicted onset of polarization ordering in the $[Py^+_{1,x}][NTf_2^-]$ around $x = 6$. [4, 66, 78, 110]

RTIL	mΔOD (2.58 eV)	mΔOD (near-IR, λ_{max})	Ratio
$[Py^+_{1,3}][NTf_2^-]$	4.73	0.44	11.0
$[Py^+_{1,6}][NTf_2^-]$	7.32	0.69	10.6
$[Py^+_{1,10}][NTf_2^-]$	10.18	0.62	16.4

Table 4.9: Ratio of the short lived absorption in the visible portion of the spectrum to the long lived absorption in the near-IR. The ΔOD at 2.48 eV was measured at a probe delay time of 200 fs. The ΔOD at the maximum in the near-IR was measured at an average probe delay time of 700 ps.

Visible TA and NTf_2^{2-} dissociation. Strong, short-lived TA in the visible region of the spectrum, Figs. 4.3 and 4.5, is consistent with recent ab initio molecular dynamics calculations performed by Xu *et al.* [148] These simulations indicate that an excess electron initially placed in the delocalized LUMO of the liquid will localize to an individual NTf_2^- anion in approximately 50 fs. The resulting NTf_2^{2-} dianion is not bound and immediately dissociates along the N−S bond to form an associated anion pair. After 200 fs a strong charge transfer transition of the associated ion pair has developed that is broad, increases in intensity with energy through the visible region of the spectrum,

and has a maximum above 3.1 eV. The shape of the simulated spectrum is very similar to the TA observed at a probe delay of 200 fs in Fig. 4.3. Although our instrument response function of 240 fs is much too slow for us to probe the putative attachment of the very early excess electron onto a NTf_2^- anion that we have mentioned above, it might be capable of detecting the predicted spectral red shifts of the dianion, although with our time resolution we would expect to see a greatly convoluted resultant of this spectral evolution. Indeed, in Figure 4.3 it can be seen that the average energy of the transient absorption between 2.07 eV and 2.82 eV decreases in the three liquids over the first 500 fs. Although it is hard to quantify this shift because the TA decreases into a basically flat TA, the signs of this early red shift can be seen in Figure 4.3 between 200 fs and 500 fs and between 1.9 eV and 1.7 eV, and are thus in qualitative agreement with Xu's predictions.

Strength of the observed transition cannot be quantified without knowledge of the concentration. However, a lower limit for the absorption coefficient can be estimated assuming that every absorbed photon in the pump at 6.20 eV created an absorber at 2.58 eV. Since this approximates the highest possible concentration for the absorber it produces a lower limit for its absorption coefficient. Using the value of 10 mOD for the absorption at a probe delay of 200 fs in $[Py^+_{1,10}][NTf_2^-]$, Table 4.9, and our experimental geometry, the lower limit is $\varepsilon = 40,000\ M^{-1}\ cm^{-1}$. Double the typical absorptivity of a solvated electron in similar RTILs, [11, 67, 74] this lower limit agrees with the qualitative prediction of a strong charge transfer absorption calculated by

Xu *et al.* for the associated anion pair. Sub-picosecond rise and decay of the TA at 2.48 eV, Table 4.4, are also consistent with the simulations by Xu *et al.* [148] In the simulations, localization and dissociation of the anion occurred in less than 100 fs to create the strongly absorptive associated anion pair. At less than half of the width of instrument response function, the 22–69 fs time constants measured for the appearance of the signal at 2.58 eV were susceptible to uncertainties in the time origin and shape of the instrument response. However, inclusion of the finite rise in the signal statistically improved the fits when compared to an instantaneous rise, indicating ∼50 fs development of the signal in agreement with the simulations. Decay of the measured signal with a 0.62–0.76 ps time constant is consistent with the prediction from the simulations that the strong charge transfer transition will be lost as a result of strong sensitivity to relative orientation and separation of the two anion fragments. Driven by impulsive bond cleavage, energy partitioned to rotation of the fragments will very quickly scramble the ensemble average relative orientation. Broad agreement between the visible TA spectra presented here and the simulations of Xu *et al.* offers strong evidence that the observed TA in the visible region of the spectrum at short (<3 ps) delay times originates from charge transfer transitions between associated anion fragments following dissociation of the NTf_2^{2-} dianion.

Near-IR TA and the solvated electron. Radiolysis and UV laser photolysis experiments on tetralkylammonium and pyrrolidinium bistriflimide RTILs consistently

yield broad TA spectra peaking around 1100 nm with lifetimes in the range of hundreds of nanoseconds. These transients are quenched by a variety of electron scavengers on both ultra-fast [91] and ns time scales. [46,74,92,125,145,146] Direct spectroscopic evidence for an electron was obtained from EPR experiments on irradiated glassy $[Py^{+}_{1,4}][NTf^{-}_{2}]$ at low temperatures. [105] The adiabatic ionization potential of the NTf^{-}_{2} anion has been estimated at 5.5 eV, [118] indicating that 6.20 eV excitation should be thermodynamically sufficient to detach an electron.

As we have mentioned in the Introduction, however, the assignment of this near-IR TAs to the solvated electron is apparently contradicted by the ab initio simulations done by the Margulis group [86, 148]. These authors have suggested that charge transfer transitions between the products of dissociation of the NTf^{2-}_{2} dianion which we have considered above, enclosed in a solvent cage, might explain the long lived near-IR TA. This would contribute to the near-IR TA between delays of $\approx$ 0.5 ps (when there has been a significant decay of the dianion) and until the fragments have escaped from the solvent cage. A rough estimate for the escape lifetime of two fragments inside a cage can be computed from the simple Stokes-Einstein hydrodynamic model,

$$D_i = \frac{k_B T}{6\pi\eta r_i} \tag{4.2}$$

where η is the shear viscosity of the liquid and r_i is the radius of the diffusing particle i. The rate of escape from the solvent cage is related to the diffusivity of the two fragments

D [13],

$$\tau_{esc} = \frac{R^2}{D_1 + D_2} \tag{4.3}$$

where R is the sum of the fragment radii and D_1 and D_2 are the self-diffusion constants of each fragment. Assuming two fragments each with a radius of 1.7 $\AA$ and no potential between them, the cage escape lifetimes in $[Py^+_{1,3}][NTf^-_2]$, $[Py^+_{1,6}][NTf^-_2]$ and $[Py^+_{1,10}][NTf^-_2]$ are thus estimated to be 3.3 ns, 6.3 ns and 11 ns, respectively. [1] These lifetimes of several ns are beyond what our experiments can measure with any accuracy, and we see no evidence of a slow TA decay in any of the three liquids. These time constants can however be compared with the lifetimes of the NIR TA obtained from Pulse Radiolysis experiments of bistriflimide ILs. Takahashi *et al.* have found a 240 ns first order decay of the NIR TA assigned to the solvated electron in $[N^+_{1113}]$ $[NTf^-_2]$ [126], and Neta and Wishart found a lifetime of 300 ns for the NIR induced by PR of$[N^+_{1444}]$ $[NTf^-_2]$. [146] Using the shear viscosity of these two liquids we obtain cage escape lifetimes 5 ns for the first, and 32 ns for the second. The difference between the hydrodynamic estimation for the cage escape lifetimes and the decay of the of the near-IR TAs points towards the fragmentation products in the solvent cage not being the responsible for these TAs.

The deviations of the diffusivity in $[Py^+_{1,4}][NTf^-_2]$ compared to the Stokes Einstein (SE) model have recently been investigated theoretically by the Margulis group [149]. They find that for *ions* with volumes comparable to the IL constituent ions or up to

[1] Note that since both fragments are negatively charged one would expect that their escape from the solvent cage would be much faster still

about 10 times smaller, diffusion is a few fold faster than predicted by the SE model. This, together with the coulombic repulsion between the anion and radical anion pair in the solvent cage reinforces the argument that intermolecular charge transfer between fragments of the NTf_2^{2-} dianion cannot account for the long lived NIR TA. Thus given the different kinds of spectroscopic evidence mentioned above along with the quenching behavior observed in the presence of the electron scavenger N_2O, leads us to conclude that the broad, long-lived near-IR TA is dominated by free solvated electrons.

Absorption in the near-IR grows in and narrows on a time scale of 0.4–0.6 ps, Figs. 4.3 and 4.6 and Table 4.5. Quenching of the TA in the near-IR by modest concentrations of N_2O decays on the same time scale, Fig. 4.8 and Table 4.8. Sub-ps quenching behavior that is rapidly arrested can be explained by a first-order quenching process with a time dependent rate coefficient to account for the sub-ps loss of reactivity. [91] The conclusion is that the initially delocalized, highly reactive electron in the LUMO of the liquid localizes to a cavity in the liquid in $\sim$0.5 ps. Spatial localization is supported by the subsequent loss of reactivity with N_2O until time scales $>$1 ns, consistent with much slower diffusion mediated bimolecular reaction.

In all of the samples the TA shifts to higher energy at later delay times, Fig. 4.8. Given that the peak energy of the TA and the rate of relaxation are dependent on the size of the cation, and that the excess electron cannot survive in the proximity of NTf_2^- anions, the excess solvated electron must be associated with cation rich domains. At all probe delay times, E_{max} is shifted to lower energy with longer *n*-alkyl chain length

indicating a deeper potential energy trap for the electron. This suggests that the smaller cations are able to more efficiently pack themselves around the free electron. The TA spectra are in good qualitative agreement with the radiolysis experiments by Wishart and coworkers on $[Py^{+}_{1,4}][NTf^{-}_{2}]$ both in the shape and position. [145] At a probe time delay of 15 ps, roughly the time resolution of the radiolysis experiments, the initial TA is much broader and peaked at lower energy than any of the spectra presented here at a comparable time delay. By 800 ps the TA in the radiolysis experiment on $[Py^{+}_{1,4}][NTf^{-}_{2}]$ is in quantitative agreement with the photodetachment experiments, with a similar width and peak energy between the $[Py^{+}_{1,3}][NTf^{-}_{2}]$ and $[Py^{+}_{1,6}][NTf^{-}_{2}]$. Spectral diffusion in the radiolysis experiments was fitted to a biexponential rise with time constants of 36 ps and 200 ps. Although within the signal to noise of the data presented here we did not resolve any potential biexponential nature in the correlation function following photodetachment or evidence for the faster time constant, the 36 ps time constant for $[Py^{+}_{1,4}][NTf^{-}_{2}]$ is in perfect agreement with those we find for $[Py^{+}_{1,3}][NTf^{-}_{2}]$ and $[Py^{+}_{1,6}][NTf^{-}_{2}]$.

Solvation of the free electron in the range measured here, 2–850 ps, demonstrated a strong and systematic dependence on the cation, Fig. 4.8 and Table 4.6. This is analogous to solvation measurements in the same series of RTILs reported by Maroncelli and coworkers quantifying the dynamic Stokes shift (DSS) of Coumarin 153. [152]. The DSS

results demonstrated solvation on a wide range of time scales, including a significant sub-ps component. Measurements presented here were not able to access any potential sub-ps solvation due to the finite localization time for the electron and spectral interference from the associated anion pair discussed above. Beyond the ultrafast component, the DSS measurements were fitted to a stretched exponential with time constants of 140 ps, 420 ps and 820 ps for $[Py^+_{1,3}][NTf^-_2]$, $[Py^+_{1,6}][NTf^-_2]$and $[Py^+_{1,10}][NTf^-_2]$respectively. The stretching factors were all around 0.5. These time constant are significantly slower than the exponential time constants reported here of 33 ps, 57 ps and 84 ps. Although the quality of the data present in Fig. 4.8 is not sufficient to definitively distinguish between an exponential and a stretched exponential rise, for direct comparison the data was fitted to stretched exponentials with resulting time constants of 36 ps, 56 ps and 116 ps, and stretching factors around 0.6. In both experiments the time constants correlate well with the viscosity of the liquids, Fig. 4.8 inset, suggesting similarity in the associated solvent reorganizational motions. However, observed solvation times for the electron are an order of magnitude faster than the comparable intermediate dipolar solvation. Contributing factors to the difference in solvation time scales include the different nature and larger magnitude of the solvent perturbation associated with detachment of the electron compared with the change in solute dipole moment. As discussed above when comparing photodetachement and radiolysis, the larger total reorganization involved in solvating the higher energy electrons in the radiolysis experiments accelerated the observed solvation.

4.5 Conclusion

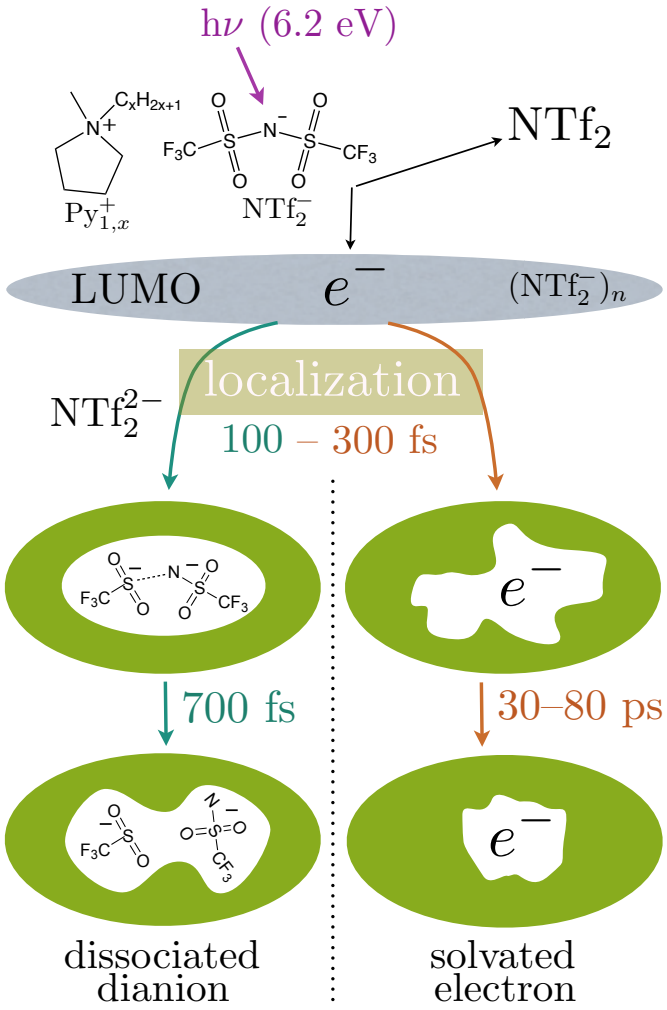

Figure 4.13: Illustration summarizing the competing channels in the photodetachment dynamics following excitation at 6.20 eV common to the $[Py^+_{1,x}][NTf^-_2]$ RTILs investigated.

Photo excitation of a series of neat methyl-alkyl-pyrrolidinium bis(trifluoromethylsulfonyl)amides at 6.20 eV promotes an electron to the LUMO of the liquid, which simulations by Xu *et al.* indicate to be delocalized over the NTf^-_2 anions. Long range reactive reach at short

time delays support the delocalized nature of the initially excited electron, and sub-ps loss of that reactivity indicates localization of the electrons on a ∼300 fs timescale. As summarized in Fig. 4.13, there are two competing sub-ps localization channels with different spectroscopic signatures. A short-lived absorption in the visible spectrum is assigned to the charge transfer transition of the dissociative NTf_2^{2-} dianion, consistent with simulations that predict localization of the electron onto an individual NTf_2^- anion. Long-lived, broad absorption in the near-IR is assigned to the solvated free electron based on agreement with prior photodetachment and radiolysis experiment in a wide range of common and ionic liquids. The free electron localizes to a cavity in less than a picosecond followed by solvation of the electron on a 30–50 ps time scale. Evidence for the two competing channels provides an explanation for the apparent contradiction between the short lifetime of the free electron predicted by the simulations of Xu *et al.*, the observation of anion dissociation products under radiologic conditions, and prior photolysis and radiolysis experiments that found compelling evidence for stable, long lived free electrons.

Branching between the two channels, the degree of solvation for the free electrons, and the solvation time scales of the free electrons are dependent on the size of the cation between $[Py^+_{1,3}][NTf_2^-]$ and $[Py^+_{1,10}][NTf_2^-]$. This is the range in *n*-alkyl chain length associated with the onset of polarizability structuring in the liquids. Compared with $[Py^+_{1,3}][NTf_2^-]$ and $[Py^+_{1,6}][NTf_2^-]$, $[Py^+_{1,10}][NTf_2^-]$ favors the channel that localizes onto an individual NTf_2^- rather than a cationic cavity. Smaller cations are able to more

effectively solvate the free electrons providing a deeper trap, and solvation proceeds on a faster times scale as the alkyl chain shortens producing a trend that is correlated with the viscosity of the liquids. Compared with free electrons produced by radiolysis, solvation of the free electron is slower reflecting the lower energy of the initially detached electrons. Compared with dipolar solvation measurements, the intermediate solvation time scales are an order of magnitude faster. This suggests different coupling to the spectral density of the liquid for the electron compared with the dipolar solvent probe that reflects the different local solvent environments, and it hints at the potential for non-linear response in the solvation of the electron.

Chapter 5

I^- photodetachment and electron cooling in a series of neat aliphatic RTILs: $[Py^+_{1,3}][NTf^-_2]$, $[Py^+_{1,6}][NTf^-_2]$ and $[Py^+_{1,10}][NTf^-_2]$

5.1 Introduction:

In the previous chapter we have analyzed the transient dynamics that follow the 6.2 eV excitation of a series of three $[Py^+_{1,x}][NTf^-_2]$ RTILs, with x = 3,6,10. The transients in the near-IR were assigned to an ejected electron based on the agreement with those TAs found under radiolytic conditions of similar liquids and photoionization of electron

donors in the same liquids, combined with the ultrafast quenching of the signal with an electron scavenger. As we have already mentioned, theoretical work [86, 95, 148, 149] as well as experimental electrochemical work [52, 53, 95], indicates that the NTf_2^- anion undergoes a dissociative attachment in the presence of excess electrons and this seems to contradict to long lifetimes observed for solvated electrons in these liquids (100's of ns being typical). We found a very intense and short lived TA in the blue part of the VIS part of the spectrum that agrees almost quantitatively with the computed spectral evolution of the fragments formed by the dissociation of the NTf_2^{2-} dianion obtained by the Margulis group [148] and so proposed the possibility of a competitive scheme where the very early (within 50 fs to 100 fs) and very delocalized ejected electrons either attach to a NTf_2^- anion (leading to dissociation) or are trapped in a favorable pocket in the liquid, where solvation occurs.

In comparison to the previous chapter, where excess electrons were photodetached from the NTf_2^- anions of the neat ILs, here we generate excess electrons by means of photodetachment from the well known electron donor I^-. Photodetachment from halides and the I^- anion in particular, occurs through the intermediacy of charge transfer to solvent (CTTS) states and the mechanism for electron ejection in water through these states has been well studied. [29]

Our experiment is complicated by the fact that iodide in these ILs does not absorb at 266 nm (4.66 eV) and thus we cannot easily access the better studied first CTTS band. Rather we have had to excite the second band at 200 nm (6.20 eV), which is

understood in less detail. Nevertheless, these experiments were performed in order to achieve an additional view of relaxation dynamics of excess electrons in these RTILs.

5.2 Experimental:

The laser setup, purification procedure of the ILs, spin cell and sample handling are all described the previous chapter. A set of Tetrabutylammonium Iodide stock solutions in each of the three ionic liquids were prepared in the glove box by dissolving *ca.* 10 mg of Tetrabutylammonium Iodide (Aldrich) in *ca.* 1 mL of the purified ILs. These stock solutions were stored inside the glove box and wrapped in tin foil to avoid light exposure. An amount of the corresponding stock solution necessary to yield an OD (1 mm path length) of about 1.5 at 200 nm was added to 1.8 mL of the corresponding neat IL, stirred, and transferred into the assembled spinning cell. From the OD at λ_{max} $\sim$235 nm, the [I^-] of these solutions is found to be $\sim$ 0.7 mM. Optical densities of the solutions were measured in a 1 mm Suprasil fused silica cell, in a Cary 14 UV-VIS Spectrometer. The measurements were referenced to an empty cell, and corrected the shift in the base line.

The 6.2 eV pump pulse energy at the sample (corrected for reflection and absorption through the first fused silica window) was 100 nJ per pulse. The instrument response function (IRF) of our measurements was found to be 240 fs. This was measured by exciting a series of dyes under the same experimental conditions as for IL iodide solutions (same power, same beam crossing, identical spin cell), and fitting the rises of a series of

dyes to a step function convoluted over a Gaussian whose fwhm was optimized. All of these dyes exhibited an identical rise, thus proving that they were all IRF-limited.

5.3 Results:

Figure 5.1 shows the UV absorption spectra of the Bu_4N^+ I^- solutions in the three ionic liquids used. Included for comparison, are the absorption spectra of the neat liquids. The peak at ∼5.4 eV is the well known first CTTS (charge transfer to solvent) band of the I^- anion. At the excitation energy of 6.2 eV, the OD for 1 mm path length of the iodide solutions is around 1.5, with some variability between the liquids. The OD of the neat RTIL solvent under the same conditions is about 0.26, ie more than 5 times lower. The absorption spectrum of Bu_4N^+ I^- in MeOH, shown in the Appendix, overlaps perfectly with that of K^+I^- also in MeOH from 4.8 eV to 6.3 eV, that is to say, there is no evidence of absorption from the Bu_4N^+ cation up to 6.2 eV. In the previous chapter we showed that the $Py^+_{1,x}$ cations also do not absorb below ∼6.3 eV. We therefore conclude that at the excitation energy of 6.2 eV light is only absorbed by the I^- anion, and to a much smaller extend the NTf_2^- anion from the solvent. The inset in Figure 5.1 shows the normalized first CTTS bands of I^- in the four liquids. There is a small but clear red shift of the first CTTS band as the pyrrolidinium cation becomes larger. We will see that this red shift of the first CTTS absorption band in the three liquids correlates with the position of the near-IR signals.

That the energy absorbed by the IL itself does not contribute significantly to the

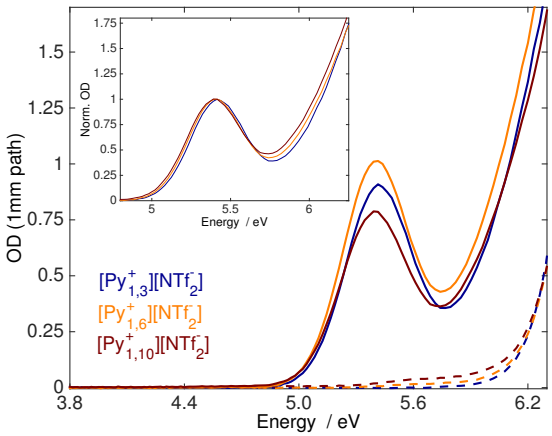

Figure 5.1: Ultraviolet absorption spectrum of the Bu_4N^+ I^- in the ILs (solid line), along with that of the neat RTIL solvents (dashed line). The inset shows the normalized peaks of the first I^- CTTS band in the three liquids. At the excitation energy of 6.20 eV, the OD of the solutions is approx. 1.5.

observed TAs is shown in Figure 5.2. The solid lines show the raw magnitude of the near-IR TA in the I^- solutions at a time delay of 10 ps, and the dashed lines show the TA under the same experimental conditions of pump power and beam crossing for the corresponding neat IL solvent. In all cases the TA from the I^- solutions are about 20 times larger than those from the neat ionic liquids.

We have also confirmed that the transients that we see upon excitation with the 6.2 eV pulse are due to the absorption of one photon by the I^- anion. Figure 5.3 shows the plot of the logarithm of the induced signal at a probe energy of 1.27 eV as a function of the logarithm of the pump pulse energy. A slope of 0.95 ± 0.03 is obtained, indicating a 1-photon process. The arrow in the figure indicates the pulse energy at the sample used in the pump-probe experiments, which is 100 nJ.

The induced transient absorptions in the near-IR and VIS part of the spectrum are

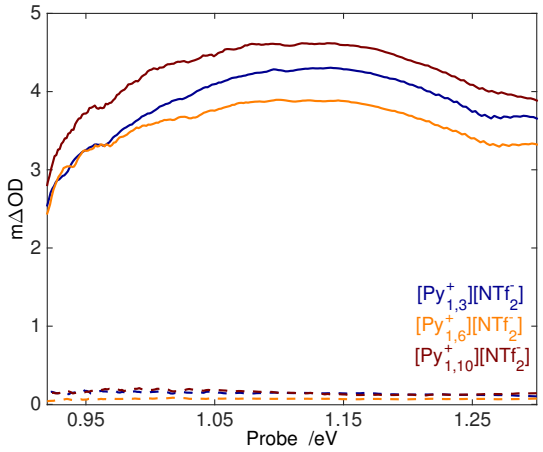

Figure 5.2: Induced TA at 10 ps after the 6.2 eV excitation. In solid line are the TAs obtained from the I^- solutions, and in dashed lines are the TAs under the same conditions for the corresponding neat ILs.

shown in Figures 5.4 and 5.5, respectively. In each liquid the near-IR and VIS transients have been scaled using the spectral overlap of the two data sets, and normalized by the global maximum. In the near-IR, the transients show the characteristic broad band that peaks at about 1.1 eV and which is attributed to the solvated electron. A well resolved rise in the TA is observed. There is also a clear shift in the maxima to lower energies in going from $[Py^+_{1,3}][NTf^-_2]$ to $[Py^+_{1,10}][NTf^-_2]$.

The transients in visible are shown only for $[Py^+_{1,3}][NTf^-_2]$ and $[Py^+_{1,6}][NTf^-_2]$ because unfortunately we ran out of the $[Py^+_{1,10}][NTf^-_2]$ liquid before the experiment could be performed. The visible transients are about 4 times less intense than in the near-IR and show a maximum at ∼2.0 eV. Very prominent in the $[Py^+_{1,6}][NTf^-_2]$ solution but also present in the $[Py^+_{1,3}][NTf^-_2]$ is a fast rise and decay of a transient between 2.2 eV and 2.5 eV that has kinetics similar to those of the much larger blue transient that we have

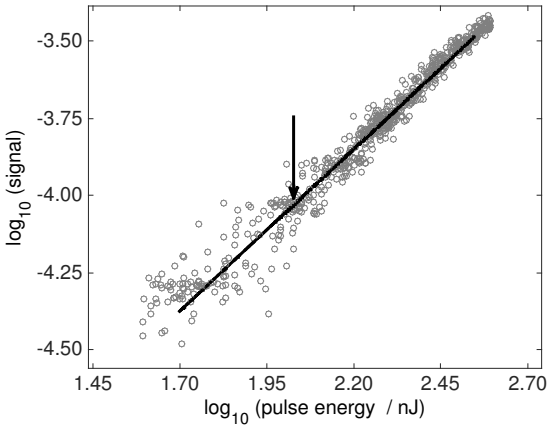

Figure 5.3: Dependence of the log of the induced signal at 980 nm and a delay of 50 ps as a function of the energy of the pump pulse measured in nJ, of an I^- solution in $[Py^+_{1,3}][NTf^-_2]$. The slope of the log - log plot is 0.95 ± 0.03 (68 % confidence interval).

described in the previous chapter for the neat liquids. Also clear in both liquids is a slow global rise of the visible transient.

The resolved appearance of the near-IR transient is shown explicitly in Figure 5.6. The transient ΔOD is integrated between 1.38 and 0.95 eV and plotted as a function of delay. For comparison, the IRF is shown as a Gaussian with fwhm of 240 fs, and also, in a dashed line, the corresponding IRF-limited rise. The data has been fitted to a single exponential convoluted over the IRF up to a delay of 5 ps. It is seen that in all of the three RTILs there is a significant delay in the appearance of the near-IR TA. The optimized fitting parameters are shown in Table 5.1, where it is seen that in the three liquids this rise has a time constant of ∼0.7 ps.

To make the spectral changes in the near-IR part of the spectrum clearer, Figure 5.7 shows the normalized near-IR TAs of each I^- solution, along with a cubic polynomial fit

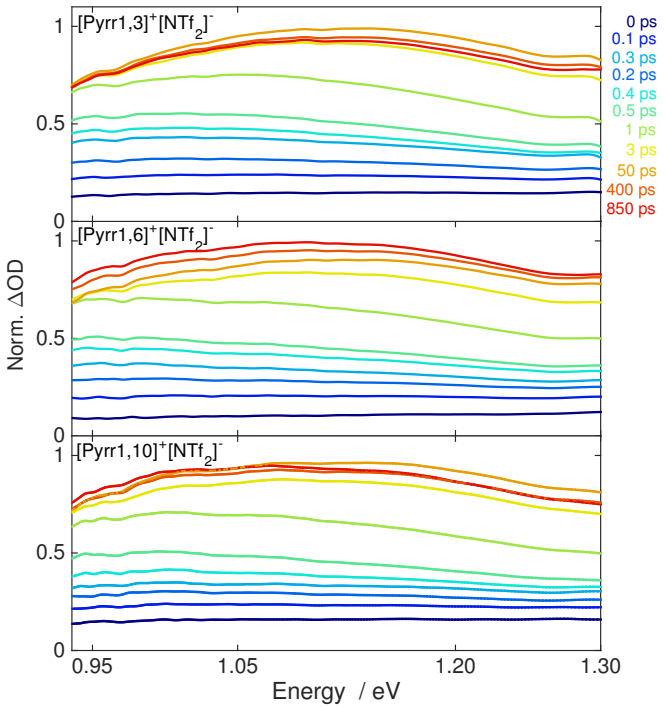

Figure 5.4: Transient absorptions in the near-IR following the 6.20 eV excitation of the I^- solutions in the three RTILs. The TAs for each solution are normalized by the amplitude of the most intense TA.

to the TA, which is used to determine the maximum of the transient at each delay. From the figure it is obvious that the TAs appear at progressively lower energies as the length of the $Py^+_{1,x}$ side chain increases from $[Py^+_{1,3}][NTf^-_2]$ to $[Py^+_{1,10}][NTf^-_2]$. Additionally, in each solution, there is a prominent shift towards higher energies happening in the first couple of ps, followed by a much slower shift back to lower energies.

Figure 5.8 shows plots of the time evolution of the near-IR E_{max} in each solution. Data from the three I^- solutions are shown in thick solid lines and diamond markers. For comparison, the results obtained in the neat RTILs are also included and shown in a

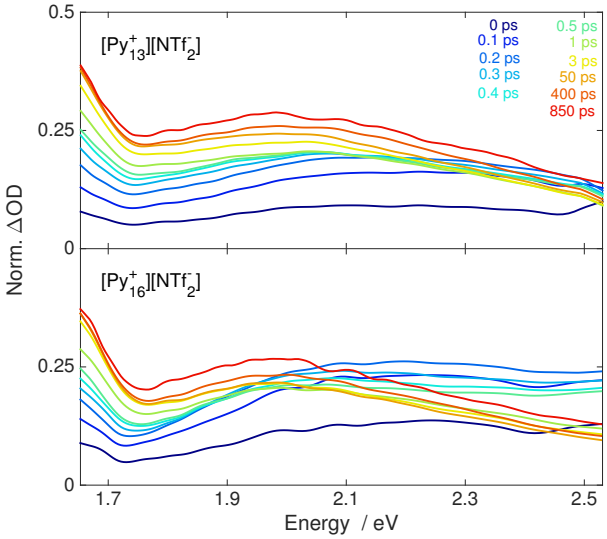

Figure 5.5: Transient absorptions in the VIS following the 6.20 eV excitation of the I^- solutions. The transients are normalized on the same scale as the near-IR data shown in Figure 5.4.

Liquid	τ (ps)
$[Py^+_{1,3}][NTf^-_2]$	0.71
	(0.69 – 0.72)
$[Py^+_{1,6}][NTf^-_2]$	0.74
	(0.72 – 0.76)
$[Py^+_{1,10}][NTf^-_2]$	0.77
	(0.75 – 0.79)

Table 5.1: Fitting parameters for exponential rise of integrated near-IR TA.

thin solid line and circle markers. In the Figure it can be seen that there is a large fast blue-shift followed by a much slower red-shift. In the case of the $[Py^+_{1,3}][NTf^-_2]$ liquid the long delay convergence of E_{max} from the I^- solution with that from the neat liquid is very clear. In the case of the $[Py^+_{1,6}][NTf^-_2]$ and $[Py^+_{1,10}][NTf^-_2]$ liquids it seems this convergence may also occur, but beyond our time observation window.

The current evolution of E_{max} in each solution has been fitted to a two sequential

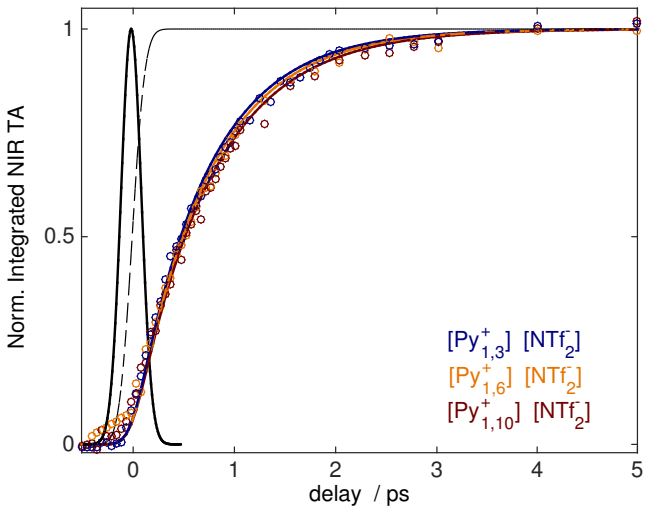

Figure 5.6: Integrated TA between 1.27 and 0.97 eV after excitation of I^- anion in the 3 RTILs. Each trace is fit to an exponential rise up to a delay of 5 ps.

Liquid	w_A	τ_1 (ps)	w_B	τ_2 (ps)	w_C	w_B - w_A	w_B - w_C
$[Py^+_{1,3}][NTf^-_2]$	1.012	1.22	1.119	584	1.103	0.107	0.016
		(1.19 – 1.25)	(1.119 – 1.119)	(130 – 1037)	(1.10 – 1.11)		
$[Py^+_{1,6}][NTf^-_2]$	0.980	1.26	1.106	325	1.090	0.126	0.016
		(1.23 – 1.29)	(1.11 – 1.11)	(186 – 464)	(1.09 – 1.09)		
$[Py^+_{1,10}][NTf^-_2]$	1.005	1.28	1.101	322	1.064	0.096	0.037
		(1.25 – 1.32)	(1.10 – 1.10)	(268 – 376)	(1.06 – 1.07)		

Table 5.2: Fitting parameters for the evolution of E_{max} of the near-IR TAs to a sequential two step scheme. See the text for details about the fitting procedure.

step kinetic scheme and the optmized fitting parameters are shown in Table 5.2. The first amplitude (w_A) for each liquid is set and fixed at the value of before the early rise. The early blue-shifts have a time constant of about 1.3 ps in the three solutions, without any apparent trend along the series. Beyond roughly 10 ps, the spectral evolution of the near-IR TA changes sign and begins to red-shift with time constants ranging from 300 to 600 ps, again without a clear trend along the three liquids. The magnitude of

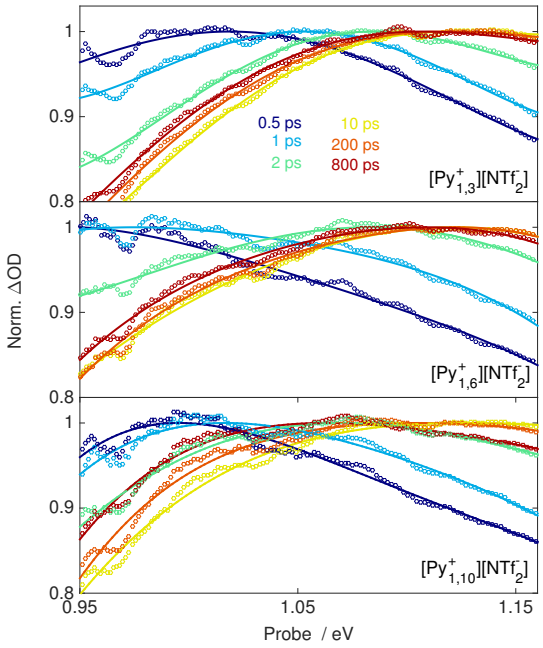

Figure 5.7: Normalized TAs in the near-IR following the 6.20 eV excitation of each of the three I^- solutions. The circles are experimental data and the solid lines are a 3rd order polynomial fit to each transient spectrum.

the early blue shift is given by w_B - w_A increases from $[Py^+_{1,3}][NTf^-_2]$ to $[Py^+_{1,6}][NTf^-_2]$ but is lowest for $[Py^+_{1,10}][NTf^-_2]$. Conversely, the amplitude of the later slower red, given by w_B - w_C shift is by far largest for $[Py^+_{1,10}][NTf^-_2]$.

The evolution of the near-IR band is characterized not only by shift in the maximum, but also by a change in width. We quantify this by means of the square root of second moment (RMSD) of the spectra between 0.97 nm and 1.27 eV. The evolution of this quantity with time is shown in Figure 5.9, which also includes, for direct comparison, the corresponding data for the neat ILs. The data has been fitted to a two sequential step scheme. It can be seen that there is an early fast narrowing of the near-IR TA,

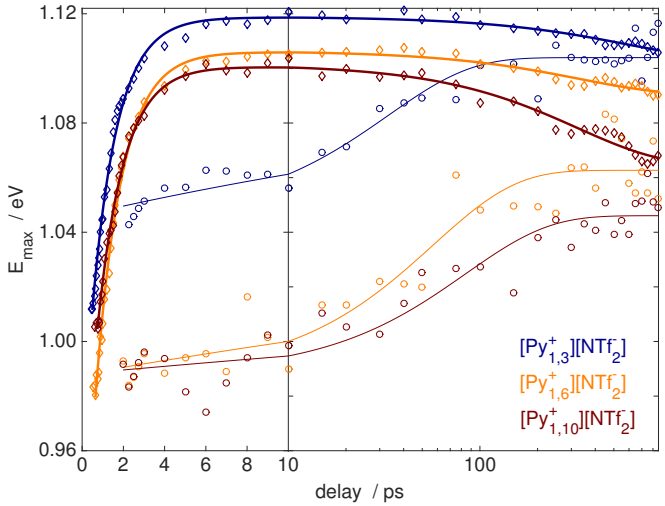

Figure 5.8: Evolution of E_{max} of the near-IR TA induced by photodetachment of I^- in the three RTILs liquids (thick solid line and diamonds) and measured in the same three neat liquids (thin solid lines and circles).

Solvent	w_A	τ_1 (ps)	w_B	τ_2 (ps)	w_C
$[Py^+_{1,3}][NTf^-_2]$	0.0850	0.33	0.0842	96	0.0844
	(0.0850 – 0.0850)	(0.31 – 0.34)	(0.0842 – 0.0842)	(80 – 112)	(0.0844 – 0.0844)
$[Py^+_{1,6}][NTf^-_2]$	0.0852	0.46	0.0843	85	0.0844
	(0.0852 – 0.0852)	(0.44 –0.48)	(0.0843 – 0.0843)	(54 – 116)	(0.0844 – 0.844)
$[Py^+_{1,10}][NTf^-_2]$	0.0857	0.56	0.0848	81	0.0850
	(0.0857 – 0.0857)	(0.54 – 0.59)	(0.0848 – 0.0848)	(63 – 99)	(0.0850 – 0.0850)

Table 5.3: Fitting parameters for a two sequential step scheme for the evolution of RMSD of the near-IR TA band between 0.95 eV and 1.38 eV.

followed by a slower broadening. The fast narrowing has time constants ranging from 0.33 ps for $[Py^+_{1,3}][NTf^-_2]$ progressively getting slower up to 0.56 ps for $[Py^+_{1,10}][NTf^-_2]$. It is interesting that these time constants are significantly faster than the early blue shifts which as we mentioned have time constants of about 1.3 ps, and thus show that there is rearrangement faster than indicated by the shift in E_{max}. The following broadening of the near-IR band also differs significantly from the later red shift described above in that

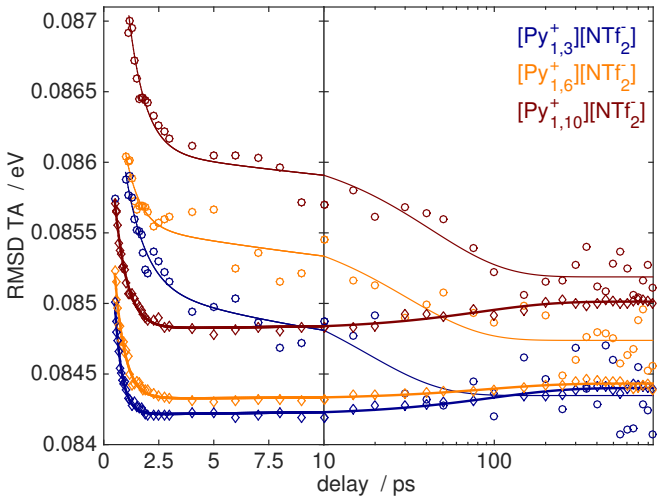

Figure 5.9: RMSD of the near-IR transients from the integral between 0.99 eV to 1.31 eV. The data is fit to a two sequential step kinetic scheme between 0.5 ps to 850 ps.

the time constants are significantly faster than those for the red shift, the broadening process having either ended or become very slow at the end of our observation window of 850 ps.

5.4 Discussion

Light absorption in the I^- solutions. We have seen that neither the I^- counter ion Bu_4N^+ or the $Py^+_{1,x}$ cation absorb at energies below 6.3 eV, so that the absorption at the excitation energy of 6.20 eV is absorbed solely by I^- and NTf_2^- anions. To further test this, we have fit the absorption spectra of the I^- solutions to a sum of two gaussians whose separation is fixed at 0.93 eV (the same energy separation between the two first CTTS bands of I^- in water) plus the contribution of the IL solvent. These fits, shown

in the appendix, are very good, and thus further support that up to 6.3 eV, all the absorption can be explained in terms of the I^- and NTf_2^- anions.

The ODs of the I^- solutions and corresponding neat ILs at 6.20 eV are for $[Py^+_{1,3}][NTf_2^-]$, $[Py^+_{1,6}][NTf_2^-]$ and $[Py^+_{1,10}][NTf_2^-]$: 0.24 and 1.37, 0.24 and 1.54. and 0.27 and 1.29, respectively. From these, the fraction of 6.20 eV light absorbed by the NTf_2^- anion is : 0.18 , 0.16 and 0.21, that is, at most one fifth of pump light is absorbed by the NTf_2^- anion. We have seen in Figure 5.2 that this results in TAs in the near-IR that are $\sim$20 times smaller that those obtained from the photons absorbed by the I^-, and thus their effect in the observed transient dynamics is safely disregarded.

Detachment Mechanism. In the neat liquid experiments described in the previous chapter, we saw that in the visible part of the spectrum very intense short-lived transients appeared at early times, and we assigned these transients to the dissociation products of the NTf_2^{2-} dianion. In Figure 5.5 we also see that both the $[Py^+_{1,3}][NTf_2^-]$ and $[Py^+_{1,6}][NTf_2^-]$ solutions exhibit a short-lived transient in the bluest part of the visible spectrum, albeit much less intense than in the neat liquids. Can this TA be explained by the $\sim$20% of pump light absorbed by the NTf_2^- anions? This question is complicated by the necessarily different overlap of the pump and probe beams in the neat liquids and I^- solutions, due to the very different ODs at 6.20 eV. If this geometrical effect is considered small, then taking into account the pump power in the neat experiments (450 nJ/pulse) and the different ODs in the in the neat liquids and I^- solutions, we compute a ratio of intensities for this blue TA of 10.5 for neat $[Py^+_{1,3}][NTf_2^-]$ vis a vis

I^- in $[Py^+_{1,3}][NTf^-_2]$ and of 11.7 for neat$[Py^+_{1,6}][NTf^-_2]$ vis a vis I^-/ in $[Py^+_{1,6}][NTf^-_2]$. The ratios that we calculate from the raw amplitudes of the TAs at 2.38 eV are 16 for $[Py^+_{1,3}][NTf^-_2]$ and 8 for $[Py^+_{1,6}][NTf^-_2]$. Within the limited precision of these estimations, the observed short lived TA in the visible can be explained by the fraction of light absorbed by the solvent anions.

This is a rather meaningful conclusion given the expected great reactivity of the NTf^-_2 anion towards dissociative electron attachment, because it implies that the 6.20 eV electron photodetachment from the I^- anion in these solvents very likely does not involve any delocalized state as we found in the photodetachment of the neat $[Py^+_{1,x}][NTf^-_2]$ liquids, as we would expect these to yield large TAs in the blue part of the visible spectrum. Thus, in this system the ejection distance is either significantly shorter than in the neat liquid measurements, or otherwise very selective into traps (possibly cavities) where the electron cannot react with the NTf^-_2 anions.

Small ejection distances are well known for the photodetachment of I^- in aqueous solution with excitation energies within the *first* CTTS band. [29, 69, 79, 133] In this case the commonly accepted picture consists in an excitation into a CTTS sate whose core iodine atom is in its ground state $^2P_{3/2}$, and the excited electron is in an nonsymmetrical space around the atom with an initial shape determined by the fluctuations of the solvent molecules around the parent iodide ion. [29, 81, 112, 113] This early state is followed by ∼300 fs adiabatic localization of the excited electron into a electron –

parent iodide atom pair within the same solvation shell. [57, 112, 113] This electron-atom pair is thought to be stabilized by a combination of the monopole-induced dipole interaction between the electron and the polarizable iodine atom and with the dipoles of the surrounding water molecules. [113] A this stage a competition for geminate recombination and diffusive dissociation of the pair occurs. In water, the rate constant for recombination of this electron-atom pair is $\sim$ 30 ps, and the average recombination fractions approach $\sim$70%. [29] One might imagine a mechanism where the CTTS state formed with 6.20 eV excitation rapidly interconverts to the same CTTS state formed by excitation within the first CTTS band, and then follows the same ejection path described above. However, we see no evidence of recombination in the near-IR part of the spectrum, where the electron – iodine atom pair is expected to absorb. It is hard to explain how recombination of such a e – iodine atom contact pair would become much slower or the diffusive dissociation much faster by a change in solvent. This mechanism therefore does not seem a good candidate.

Also in water, however, when the excitation energy reaches the *second* CTTS band, ie the same that we are exciting at 6.20 eV, the fraction of early recombination decreases to about 40%, indicating that a different mechanism is operating.

It is believed that because the 0.93 eV energy difference between the two CTTS transitions is equal to the energy difference between the spin-orbit excited iodine atom $^2P_{1/2}$ and its ground state $^2P_{3/2}$, the difference in the CTTS states reached through the second or first CTTS bands resides in the spin-orbit state of the core iodine atom.

To explain the change in mechanism in aqueous solutions it has been proposed that the electron ejection mechanism when the second CTTS band is excited consists in a spin–orbit induced autodetachment into the conduction band [29]:

$$[\mathrm{I}\,(^2P_{1/2})]^-_{\mathrm{CTTS}} \;\rightarrow\; [\mathrm{I}\,(^2P_{3/2})] \;+\; e^-_{CB} \tag{5.1}$$

We propose that the ejection mechanism from the CTTS formed at 6.20 in these ILs is induced by the spin–orbit relaxation of the I atom but not into a conduction band of the liquid, but rather to trapping sites:

$$[\mathrm{I}\,(^2P_{1/2})]^-_{\mathrm{CTTS}} \;\rightarrow\; [\mathrm{I}\,(^2P_{3/2})] \;+\; e^-_{trap} \tag{5.2}$$

We make yet not conjecture as to the nature of these sites, although a preformed cavity is extremely unlikely. Simulations have shown that the density of cavities with the right diameter needed to accommodate an electron is vanishingly small, and thus we do not expect the ejection to be into anything like a preformed cavity [21, 56]. This is also shown by the very large and fast blue shifts that we observe in the near-IR, Figure 5.8 which indicate a large amount of fast reorganization. These rather indicate that the electron is ejected into a shallow trap which within ∼1.3 ps has reached a meta-stable state of solvation for the electron. This trap may be an incipient cavity or some special grouping of the liquid ions.

In Table 5.1 we see that the near-IR appears with a time constant of ∼0.7 ps, which is significantly faster than that of 0.5 ps found in the neat ILs. These time constants represent a convolution of the early spectral diffusion of the near-IR TA with the increase

in population, and cannot thus be compared directly. However, the slower rise of in the I^- solution is indicative of an intermediate in the mechanism, namely the $I(^2P_{1/2})]^-_{\mathrm{CTTS}}$ that we have proposed. The rate of electron ejection from this state, induced by spin–orbit relaxation, may be limited by the frequency of appearance of appropriate incipient traps near the CTTS state, or by the tunneling barrier.

Electron Solvation We have spoken above of a meta-stable state of solvation after the initial 1.3 ps blue shift because after this time the near-IR peak evolves only with a time constant of 400 to 600 ps, although a slight narrowing does happen with a time constant of ∼80 ps (Table 5.3). This much slower spectral evolution may involve a greater reorganization of the same ions already involved in the first stage of solvation of the electron, or it may require a fluctuation of the arrangement of the ions somewhere near this trapped electron into a different kind of deeper trap into which the electron may tunnel and in which the it shows a redder spectrum. Spectral red shifts of a solvated electron have been encountered before. For example, in the two photon photoionization of hexane and iso-octane the near-IR transient was observed to red-shift with a time constant of 2 ps, and this was attributed to the expansion of the cavity in which the electron was trapped. [121]

This second stage of solvation, and possibly last in these liquids, seems to be accessed directly by the ejected electrons in the neat liquids and with lifetimes of 50 to 90 ps. This is strongly suggested by the convergence of the near-IR TA in both cases as told by the convergence of both E_{max}, Figure 5.8, and the width of the transient band, Figure

5.9.

The fact that this (possibly) final state of electron solvation is reached faster in the neat liquid experiments is expected given the initial great delocalization that both Margulis' simulations and our finding of an significant sub-ps quenching component suggest.

As can be seen in 5.8, there is a clear trend in the position of the near-IR TA at long time delays in the three ILs, the TA appearing at lower energies as the size of the pyrrolidinium cation increases.

It is well known that E_{max} of solvated electrons in very diverse solvents does not correlate with the static dielectric constant or refractive index, but it does correlate with the position of the first CTTS band of the iodide ion in that solvent [3,89], indicating that the excitation energy of the solvated electron is affected by the solvent proportionally to the same effect on the energy of the CTTS transition. Over the wide spectrum of solvents over which this correlations stands, the slope of the linear trend is ~ 1.65. [89] It is interesting that we also find that the E_{max} of the near-IR TA in the three liquids correlates well with the energy of the first CTTS band of the I^- ion that liquid. This is shown in Figure 5.10. Because within our time window of 850 ps the solvation of the electron is not complete, we show the trend at 10 ps, when the near-IR has roughly shifted to its bluest position in each of the four liquids, and at ∞, as given by the value of the last weight in the sequential scheme used to fit the evolution of E_{max}.

The slope of 1.3 for the first stage of solvation (measured at 10 ps) indicates on the

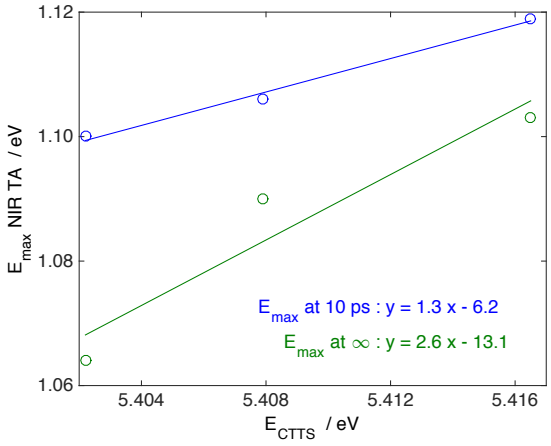

Figure 5.10: Correlation of the peak of the near-IR TA vs. the first CTTS band energy in the three ILs. The correlation is shown at a 10 ps delay, when it roughly attains it highest energy for the three liquids, and at infinity, as given by the last weight factor in the fits of E_{max} vs delay. In order of increasing E_{CTTS}, the data points correspond to $[Py^+_{1,10}][NTf^-_2]$, $[Py^+_{1,6}][NTf^-_2]$, and $[Py^+_{1,3}][NTf^-_2]$

one hand that as in common molecular liquids, the absorption spectrum of the solvated electron at this stage is more sensitive to the IL composition than the CTTS transition (by 30 %). On the other hand, this stage of solvation is significantly less sensitive to the ionic liquid structure than the later stage of solvation (with a slope of 2.6). Given that these liquids differ only on the size of the cation, it seems plausible that in the later stage of solvation the cations play a bigger role than in the first stage of solvation. This may also explain the larger amplitude of red-shift in the case of the $[Py^+_{1,10}][NTf^-_2]$ liquid, since it is conceivable that in the $[Py^+_{1,10}][NTf^-_2]$ the greater association with the cation also implies a greater increase in the space available to the electron.

At this stage of our understanding it is still very difficult to make propositions regarding the precise nature of the solvated electron in these liquids. Polarized hole

burning experiments have been suggested as a test for electrons in a cavity and given the strong near-IR signals that can be obtained by I^- photodetachment, this experiment can likely be carried out in this system.

Origin of the visible Transient. We have already discussed the fast rise and decay of the TA between ∼2.3 – 2.5 eV as likely solely due to the fraction of light absorbed by the NTf_2^- anions. There is a significant difference in the shape and intensity between the visible transient produced by photodetachment of the I^- solution and of the neat liquids. Here, the visible TA shows a peak at ∼2.0 eV and there is also a slow generalized rise of the absorption, whereas in the neat liquids the visible TA was flatter and static within 800 ps. Part of the signal we expect to be due to the high energy tail of the electron absorption, although this has not been confirmed by quenching experiments.

The slow rise in signal that we see here cannot be thought as part of the near-IR spectral diffusion since in the hundreds of ps that TA undergoes a red shift and not a blue shift. Assignment of the visible transient to the iodine atom hole seems also very unlikely given that the absorption spectra of iodine atoms in solvents so different as water and cyclohexane appears between 3.5 eV and 4.8 eV [76, 80]. Likewise a reaction of the iodine atom by H abstraction to produce a C centered radical of the pyrrolidinium cations also seem very unlikely given the bond dissociation energy of the H–I bond (∼70 kcal/mol) compared with that of a secondary carbon C–H bond (∼95 kcal/mol). At the moment we don't have a good explanation for the differences in the VIS transients and dynamics between the I^- solutions and those in the neat ILs.

5.5 Conclusion

6.20 eV excitation of the second CTTS transition of I^- in a series of $[Py^+_{1,x}][NTf^-_2]$ produces solvated electrons with the near-IR TA in these RTILs. Interestingly there is no sign of geminate recombination. In order to explain this we propose a mechanism involving photodetachment into shallow traps that is induced by the spin–orbit relaxation of the core iodine atom. The intermediacy of early delocalized states of the ejected electron is ruled out because of the lack of the fast blue transient absorption that we have previously assigned to the dissociation products of the NTf^{2-}_2 dianion. The near-IR transient absorption undergoes a 1 ps blue shift followed by a 100's of ps red shift that converges to the same energy position that was found in the photodetachment of the neat ILs.

Chapter 6

4.67 eV photodetachment and electron relaxation in $[\mathbf{Py}^{+}_{1,4}][\mathbf{N(CN)}^{-}_{2}]$

6.1 Introduction

In the previous chapters we have investigated the dynamics of excess electrons generated by photodetachment, of either the neat liquid or of an external electron donor, in pyrrolidinium bistriflimides. We have seen that theoretical results as well as our observations indicate that the NTf_2^- anion undergoes an ultrafast dissociative electron attachment. It is thus interesting to study a system in which the anion is resistant to such a reaction. The $N(CN)_2^-$ anion, called dicyanoamide and often denoted by DCA, is believed to be

resistant to both strongly reductive and oxidizing conditions, both the reduced form (dianion) and the oxidized (hole, or neutral radical) being stable. [118, 149] Because of this we have studied the ensuing dynamics after photoexcitation in this liquid. Thus, even if from a different liquid, and hence surely with different detachment and electron trapping and solvation dynamics, the study of $[Py^+_{1,4}][N(CN)^-_2]$ may provide a view into these dynamics in ILs without interference of the reaction of the NTf^-_2 anion with the excess electrons. Besides, there is an ongoing quest for low viscosity RTILs that are resistant to the presence of solvated electrons, and $[Py^+_{1,4}][N(CN)^-_2]$, in combination with its low viscosity (45 cP at room temperature), is an important promising candidate. It is therefore of interest to investigate the early processes involving an excess electron in this liquid.

The results presented in this chapter are of a semi-preliminary nature, further experimenting and analysis being still required, but we still present them because they raise new interesting questions on how to interpret the results in the $[Py^+_{1,x}][NTf^-_2]$ liquids.

6.2 Experimental

The laser setup, procedure for purifying the IL, spin cell and sample handling are all described in previous chapters. The excitation wavelength used was 266 nm (4.67 eV), and the setup for the generation of these laser pulses has also been described in the experimental chapter. The $[Py^+_{1,4}][N(CN)^-_2]$ IL originates from Iolitec and was kindly given to us by James Wishart. It was received as a pale yellow liquid. It was cleaned four

consecutive times using our standard procedure. Figure 6.1 shows the UV absorption spectrum of the after each cleaning step.

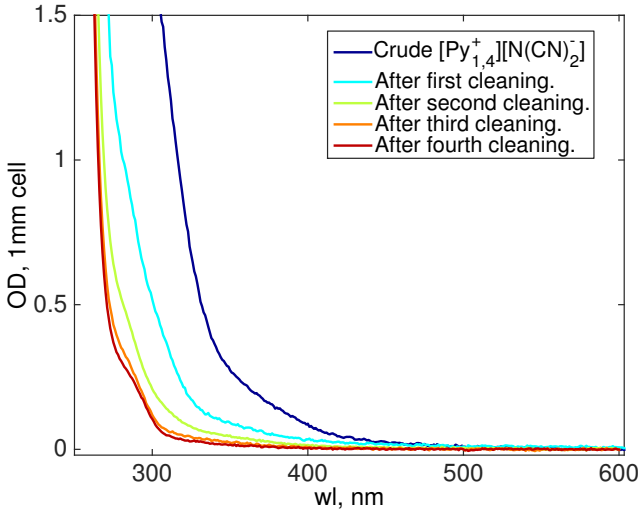

Figure 6.1: Ultraviolet absorption spectrum the $[Py^{+}_{1,4}][N(CN)^{-}_{2}]$ RTIL at each purification step.

The clean RTIL was kept in a sand bath at 80° under vacuum for 4 days, then replenished with nitrogen, and transferred to the glove box. About 1.8 mL of the IL were introduced into the spin cell in the glove box. The pulse energy at the sample was 300 nJ. The instrument response function (IRF) was measured by fitting the signal rises at 1.03 eV of a series of dyes in an identical cuvette to the one used for the experiment, to a step function convoluted over a gaussian function. The IRF was thus determined to be 135 fs. The VIS and near-IR data sets were collected back to back. For the electron scavenging experiments, the liquid in the spinning cuvette was bubbled with N_2O for 45 min and then the near-IR and VIS measurements were repeated.

6.3 Results

As can be seen in Figure 6.1, the absorption onset of the purified $[Py^+_{1,4}][N(CN)^-_2]$ liquid is just under 300 nm (4.1 eV). In a recent paper the Margulis group has calculated the HOMO–LUMO gap in this liquid at about 3.9 eV, indicating that the absorption onset the we find is probably intrinsic to the liquid and not to an impurity. We have investigated the power dependence of the near-IR transients. In a log-log plot the slope is found to 1.12 ± 0.07, compatible with a single photon process.

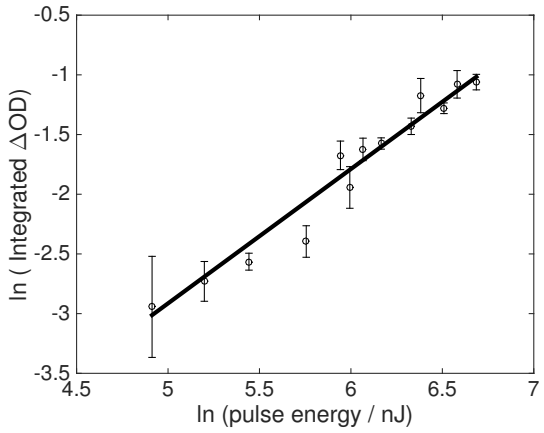

Figure 6.2: Dependence of the ln of the induced signal between 0.99 and 1.31 eV at a delay of 100 ps as a function of the energy of the pump pulse, measured in nJ, in neat $[Py^+_{1,4}][N(CN)^-_2]$. The slope of the log - log plot is 1.12 ± 0.07 (68 % confidence interval).

When the neat liquid is excited with 300 nJ (at the sample) of 4.7 eV light, we find that a very large and short lived transient appears in the bluest part of the visible region which is very similar to those observed in the neat $[Py^+_{1,x}][NTf^-_2]$ liquids. The rise of this blue transient is IRF limited, as it can be seen in Figure 6.5, and it decays with a time

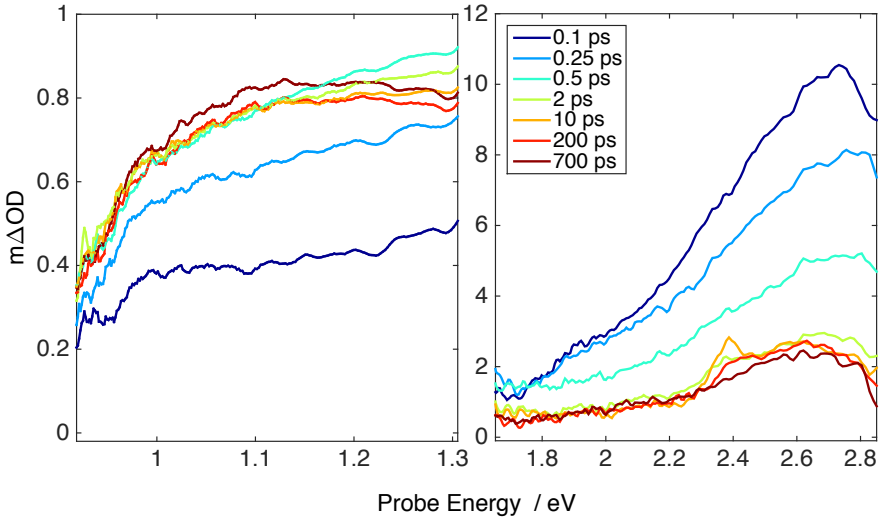

Figure 6.3: Transient absorptions in the VIS and near-IR induced by a 4.7 eV excitation in $[Py^{+}_{1,4}][N(CN)^{-}_{2}]$ at different time delays. Note the difference in y-scale in the left and right plots

constant that at 2.78 eV is 0.37 ps which becomes progressively slower at lower probe energies. From Figure 6.3 it is clear that the decay of the VIS TA is not a simple decay of the transient, and that there is an significant amount of spectral evolution in the first 2 ps after the excitation pulse. The fast decay of this TA leaves a residual broad peak that within the time window of 700 ps undergoes a minor further decay.

The near-IR rises with time constants that are slow enough to be determined given our IRF of 135 fs. When the near-IR TA is integrated between 0.99 and 1.30 eV, we find an average rise time of 170 fs (Figure 6.4). During the rise of the near-IR, the TA undergoes a significant red-shift up to ∼20 ps, when a poorly defined peak appears at about 1.17 eV, and which afterwards experiences a slight narrowing. This red shift is shown more explicitly in Figure 6.6, where the normalized near-IR TAs are fitted to a

cubic polynomial. Anything like a peak in the near-IR does not appear until between 15 and 30 ps, and the peak is much less prominent than we have seen in the $[Py^{+}_{1,x}][NTf^{-}_{2}]$ liquids. There is also close to no spectral evolution of this TA after these delays.

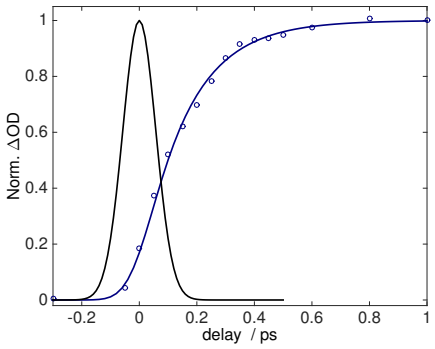

Figure 6.4: Rise of the near-IR TA signal integrated between 0.99 and 1.30 eV. The circles are experimental data and the solid line is a fit to an exponential rise convoluted over the IRF, shown in black. The optimized exponential time constant is 170 fs.

Probe (eV)	τ_1 (ps)	w_B	τ_2 (ps)	w_C
2.78	0.012	1.31	0.37	0.240
	(0.008 - 0.015)	(1.29 - 1.34)	(0.36 - 0.38)	(0.237 - 0.244)
2.07	0.008	1.26	0.41	0.254
	(0.004 - 0.011)	(1.23 - 1.30)	(0.39 - 0.44)	(0.248 - 0.260)
1.77	0.004	1.10	0.95	0.354
	(0 - 0.009)	(1.08 - 1.13)	(0.90 - 1.01)	(0.346 - 0.363)
1.31	0.131	1.05	1.66	0.891
	(0.104 - 0.157)	(0.97 - 1.14)	(-0.27 - 3.59)	(0.874 - 0.908)
1.18	0.163	1.097	0.63	0.951
	(0.079 - 0.246)	(0.71 - 1.48)	(-1.28 - 2.56)	(0.934 - 0.968)
0.92	0.136	1.03	0.9	0.956
	(0.072 - 0.200)	(0.78 - 1.30)	(-4.0 - 5.8)	(0.931 - 0.980)

Table 6.1: Optimized fitting parameters for the single color kinetics traces, shown in Figure 6.5, to a two sequential step kinetic scheme.

Saturation of the IL with N_2O has a very limited effect on the transients. In Figure 6.7 it can be seen that within noise the near-IR and visible transients are quenched to

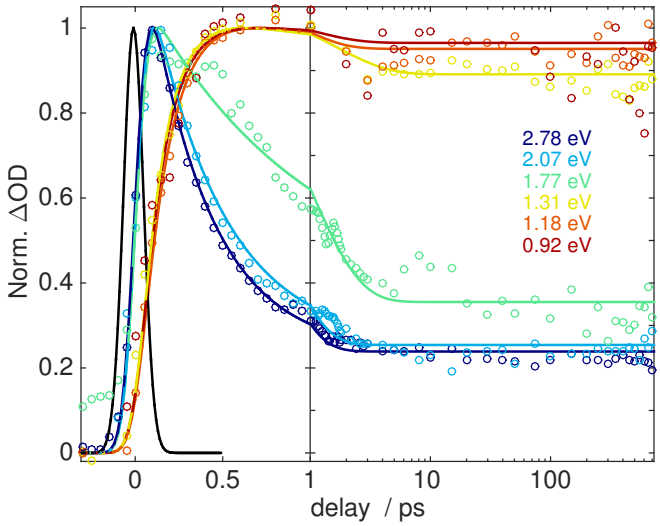

Figure 6.5: Single color kinetic traces following 4.67 eV photolysis of $[Py^{+}_{1,4}][N(CN)^{-}_{2}]$. The data is fit to a 2 step sequential kinetic scheme. Optimized fitting parameters are shown in Table 6.1.

the same extent, which at 700 ps is about 20% of the amplitude. Very meaningful is also the lack of a sub-ps quenching of signal component (with in noise) in the near-IR, indicating that there are no very delocalized states of the ejected electron involved.

6.4 Discussion

Purification of the $[Py^{+}_{1,4}][N(CN)^{-}_{2}]$ liquid has converged to an optical spectrum where the onset of the absorption is in agreement with the computed band gap of $\sim$ 4 eV. [149] According to the simulations of the Margulis group, the LUMO, or bottom of the band of unoccupied states, involves delocalization of the dry electron (before any nuclear motions have had time to respond) over several anions and cations, from which with a time constant of $\sim$70 fs the excess electron collapses on one of the $N(CN)^{-}_{2}$ anions, to

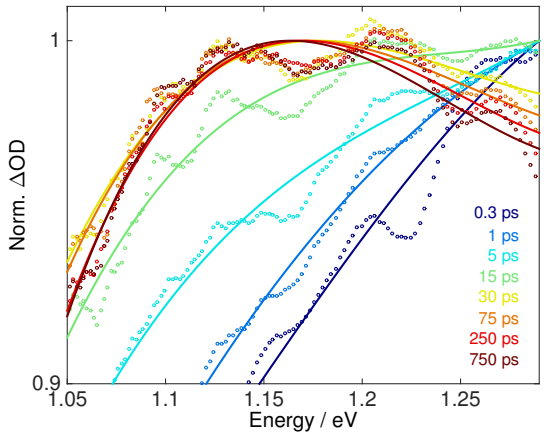

Figure 6.6: Normalized TAs in the NIR following the 4.67 eV excitation. The circles are experimental data and the solid lines are a 3rd order polynomial fit to each transient spectrum. Note that the y axis is such that the peak of the band is greatly exaggerated.

form a stable (up to several ns) dianion that shares a small fraction of spin density with the neighboring cations. This is interesting because of the observation of the large early blue TA in this neat liquid, $[Py^{+}_{1,4}][N(CN)^{-}_{2}]$, which we also saw in the neat $[Py^{+}_{1,x}][NTf^{-}_{2}]$ ILs has made us consider another possibility to explain the large early blue transients that we have seen. Given the cationic involvement in the very early delocalized state of the excess electron in this liquid that gives rise to the large short-lived TA in the VIS, it might be that the fast blue transient is due to a short-lived involvement of cationic states in the very early dry ejected electron.

The much faster rise of the near-IR TA compared to what we have seen in the $[Py^{+}_{1,x}][NTf^{-}_{2}]$ liquids and the lack of any significant spectral shifts after about ~30 ps make us consider the possibility that the absorption in the near-IR is not due to a solvated electron but rather to the dicyanoamide dianion. This possibility is supported

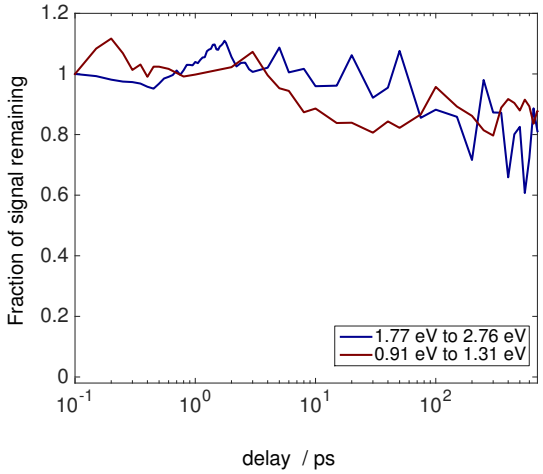

Figure 6.7: Fraction of remaining signal in the VIS and near-IR in the presence of N_2O.

by the fact that the N_2O electron scavenger quenches both the VIS and near-IR TAs equally weakly, thus implying that the species responsible for most of the absorption throughout the spectrum is a reduced species and that it is in a localized state. A qualitative agreement between the TA that we see with that computed by the Margulis group for the dianion makes us tentatively assign our TA to that species.

It might be thought as well that an electron in a cavity, which is also a localized state, is responsible for the observed transients. This seems unlikely on two accounts: it does not have the usual transient transient of with a well defined peak and a heavy tail at higher energies, and the few ps spectral evolution of the near-IR TA seems too fast for the relaxation of a cavity, as compared to what we see in the other ionic liquids.

The experimental observations that we have made in this IL still need additional detailed analysis, but they are important in underlying that the diversity of behaviors, in particular with respect to excess electrons, that ILs can exhibit.

References

[1] A. Ahosseini and A. Scurto. Viscosity of imidazolium-based ionic liquids at elevated pressures: Cation and anion effects. *Int. J. Thermophys.*, 29(4):1222–1243, 2008.

[2] D. Allen, G. Baston, A. E. Bradley, T. Gorman, A. Haile, I. Hamblett, J. E. Hatter, M. J. F. Healey, B. Hodgson, R. Lewin, K. V. Lovell, B. Newton, W. R. Pitner, D. W. Rooney, D. Sanders, K. R. Seddon, H. E. Sims, and R. C. Thied. An investigation of the radiochemical stability of ionic liquids. *Green Chem.*, 4:152–158, 2002.

[3] M. Anbar and E. J. Hart. The effect of solvent and of solutes on the absorption spectrum of solvated electrons. *J. Phys. Chem.*, 69(4):1244–1247, 1965.

[4] H. V. R. Annapureddy, H. K. Kashyap, P. M. De Biase, and C. J. Margulis. What is the origin of the prepeak in the x-ray scattering of imidazolium-based room-temperature ionic liquids? *J. Phys. Chem. B*, 114(50):16838–16846, 2010.

[5] H. V. R. Annapureddy and C. J. Margulis. Controlling the outcome of electron transfer reactions in ionic liquids. *J. Phys. Chem. B*, 113(35):12005–12012, 2009.

[6] J. L. Anthony, J. L. Anderson, E. J. Maginn, and J. F. Brennecke. Anion effects on gas solubility in ionic liquids. *J. Phys. Chem. B*, 109(13):6366–6374, 2005.

[7] B. Aoun, A. Goldbach, M. A. Gonzalez, S. Kohara, D. L. Price, and M.-L. Saboungi. Nanoscale heterogeneity in alkyl-methylimidazolium bromide ionic liquids. *J. Chem. Phys.*, 134(10):–, 2011.

[8] A. Arce, M. J. Earle, S. P. Katdare, H. Rodriguez, and K. R. Seddon. Mutually immiscible ionic liquids. *Chem. Commun.*, pages 2548–2550, 2006.

[9] M. Armand, F. Endres, D. R. MacFarlane, H. Ohno, and B. Scrosati. Ionic-liquid materials for the electrochemical challenges of the future. *Nat. Mater.*, 8(8):621, 2009.

[10] S. Arzhantsev, H. Jin, G. A. Baker, and M. Maroncelli. Measurements of the complete solvation response in ionic liquids. *J. Phys. Chem. B*, 111(18):4978–4989, 2007.

[11] A. Asano, J. Yang, T. Kondoh, K. Norizawa, R. Nagaishi, K. Takahashi, and Y. Yoshida. Molar absorption coefficient and radiolytic yield of solvated electrons in diethylmethyl(2-methoxy)ammonium bis (trifluoromethanesulfonyl)imide ionic liquid. *Radiat. Phys. Chem.*, 77(10-12):1244–1247, OCT-DEC 2008.

[12] R. Atkin and G. G. Warr. The smallest amphiphiles: Nanostructure in protic room-temperature ionic liquids with short alkyl groups. *J. Phys. Chem. B*, 112(14):4164–4166, 2008.

[13] K. S. Bagdasar'yan. Kinetics of the recombination of radicals and radical-ions in the liquid phase. *Russ. Chem. Rev.*, 53(7):623, 1984.

[14] D. Behar, C. Gonzalez, and P. Neta. Reaction kinetics in ionic liquids: Pulse radiolysis studies of 1-butyl-3-methylimidazolium salts. *J. Phys. Chem. A*, 105(32):7607–7614, 2001.

[15] D. Behar, P. Neta, and C. Schultheisz. Reaction kinetics in ionic liquids as studied by pulse radiolysis: Redox reactions in the solvents methyltributylammonium bis(trifluoromethylsulfonyl)imide and n-butylpyridinium tetrafluoroborate. *J. Phys. Chem. A*, 106(13):3139–3147, 2002.

[16] B. L. Bhargava, R. Devane, M. L. Klein, and S. Balasubramanian. Nanoscale organization in room temperature ionic liquids: a coarse grained molecular dynamics simulation study. *Soft Matter*, 3:1395–1400, 2007.

[17] O. Borodin and G. D. Smith. Structure and dynamics of n-methyl-n-propylpyrrolidinium bis(trifluoromethanesulfonyl)imide ionic liquid from molecular dynamics simulations. *J. Phys. Chem. B*, 110(23):11481–11490, 2006.

[18] A. E. Bradley, C. Hardacre, J. D. Holbrey, S. Johnston, S. E. J. McMath, and M. Nieuwenhuyzen. Small-angle x-ray scattering studies of liquid crystalline 1-alkyl-3-methylimidazolium salts. *Chem. Mater.*, 14(2):629–635, 2002.

[19] H. Brands, N. Chandrasekhar, and A. Unterreiner. Ultrafast dynamics of room temperature ionic liquids after ultraviolet femtosecond excitation.. *J. Phys. Chem. B*, 111(18):4830–4836, 2007.

[20] J. F. Brennecke and E. J. Maginn. Ionic liquids: Innovative fluids for chemical processing. *AIChE J.*, 47(11):2384–2389, 2001.

[21] C. Cadena, J. L. Anthony, J. K. Shah, T. I. Morrow, J. F. Brennecke, and E. J. Maginn. Why is co2 so soluble in imidazolium-based ionic liquids? *J. Am. Chem. Soc.*, 126(16):5300–5308, 2004.

[22] J. N. Canongia Lopes, K. Shimizu, A. A. H. Padua, Y. Umebayashi, S. Fukuda, K. Fujii, and S.-i. Ishiguro. A tale of two ions: The conformational landscapes of bis(trifluoromethanesulfonyl)amide and n,n-dialkylpyrrolidinium. *J. Phys. Chem. B*, 112(5):1465–1472, 2008.

[23] J. N. A. Canongia Lopes and A. A. H. Padua. Nanostructural organization in ionic liquids. *J. Phys. Chem. B*, 110(7):3330–3335, 2006.

[24] E. W. Castner, C. J. Margulis, M. Maroncelli, and J. F. Wishart. Ionic liquids: Structure and photochemical reactions. *Annu. Rev. Phys. Chem.*, 62(1):85–105,

2011.

[25] E. W. Castner and J. F. Wishart. Spotlight on ionic liquids. *J. Chem. Phys.*, 132(12):–, 2010.

[26] N. Chandrasekhar, F. Endres, and A.-N. Unterreiner. Evidence for laser-induced formation of solvated electrons in room temperature ionic liquids. *Phys. Chem. Chem. Phys.*, 8:3192–3196, 2006.

[27] N. Chandrasekhar, O. Schalk, and A.-N. Unterreiner. Femtosecond UV excitation in imidazolium-based ionic liquids. *J. Phys. Chem. B*, 112(49):15718–15724, 2008.

[28] N. Chandrasekhar and A.-N. Unterreiner. Relaxation dynamics upon ultrashort UV photo-excitation of an iodide doped ionic liquid and of a pure lithium iodide melt. *Z. Phys. Chem.*, 220(10):1235–1246, 2009.

[29] X. Chen and S. E. Bradforth. The ultrafast dynamics of photodetachment. *Ann. Rev. Phys. Chem.*, 59(1):203–231, 2008.

[30] D. M. D'Alessandro, B. Smit, and J. Long. Carbon dioxide capture: Prospects for new materials. *Angew. Chem. Int. Ed.*, 49(35):6058–6082, 2010.

[31] J. H. Davis, Jr. and P. A. Fox. From curiosities to commodities: ionic liquids begin the transition. *Chem. Commun.*, pages 1209–1212, 2003.

[32] M. Deetlefs, C. Hardacre, M. Nieuwenhuyzen, A. A. H. Padua, O. Sheppard, and A. K. Soper. Liquid structure of the ionic liquid 1,3-dimethylimidazolium bis(trifluoromethyl)sulfonylamide. *J. Phys. Chem. B*, 110(24):12055–12061, 2006.

[33] M. G. Del Popolo and G. A. Voth. On the structure and dynamics of ionic liquids. *J. Phys. Chem. B*, 108(5):1744–1752, 2004.

[34] A. P. Demchenko. The red-edge effects: 30 years of exploration. *Luminescence*, 17(1):19–42, 2002.

[35] V. Dmitriev, G. Gurzadian, and D. Nikogosyan. *Hanbook of Nonlinear Optical Crystals.* Springer, 1999.

[36] J. Dupont. From molten salts to ionic liquids: A nano journey. *Acc. Chem. Res.*, 44(11):1223–1231, 2011.

[37] M. D. Ediger. Spatially heterogeneous dynamics in supercooled liquids. *Annu. Rev. Phys. Chem.*, 51(1):99–128, 2000.

[38] C. G. Elles, A. E. Jailaubekov, R. A. Crowell, and S. E. Bradforth. Excitation-energy dependence of the mechanism for two-photon ionization of liquid h2o and d2o from 8.3 to 12.4ev. *J. Chem. Phys.*, 125(4):044515, 2006.

[39] F. Endres, O. Hofft, N. Borisenko, L. H. Gasparotto, A. Prowald, R. Al-Salman, T. Carstens, R. Atkin, A. Bund, and S. Zein El Abedin. Do solvation layers

of ionic liquids influence electrochemical reactions? *Phys. Chem. Chem. Phys.*, 12:1724–1732, 2010.

[40] H. Enqvist. A setup fo efficient frequency tripling of high-power femtosecond laser pulses. Master's thesis, Lund University, 2004.

[41] K. Fujii, R. Kanzaki, T. Takamuku, Y. Kameda, S. Kohara, M. Kanakubo, M. Shibayama, S.-i. Ishiguro, and Y. Umebayashi. Experimental evidences for molecular origin of low-q peak in neutron/x-ray scattering of 1-alkyl-3-methylimidazolium bis(trifluoromethanesulfonyl)amide ionic liquids. *J. Chem. Phys.*, 135(24):–, 2011.

[42] A. M. Funston and J. F. Wishart. *Dynamics of Fast Reactions in Ionic Liquids*, volume 901 of *ACS Symposium Series*, chapter 9, pages 102–116. ACS, 2005.

[43] R. Giernoth. Task-specific ionic liquids. *Angew. Chem. Int. Ed.*, 49(16):2834–2839, 2010.

[44] L. Gontrani, O. Russina, F. L. Celso, R. Caminiti, G. Annat, and A. Triolo. Liquid structure of trihexyltetradecylphosphonium chloride at ambient temperature: An x-ray scattering and simulation study. *J. Phys. Chem. B*, 113(27):9235–9240, 2009.

[45] J. Grodkowski and P. Neta. Formation and reaction of Br_2^- radicals in the ionic liquid methyltributylammonium bis(trifluoromethylsulfonyl)imide and in other

solvents. *J. Phys. Chem. A*, 106(46):11130–11134, 2002.

[46] J. Grodkowski and P. Neta. Reaction kinetics in the ionic liquid methyltributylammonium bis(trifluoromethylsulfonyl)imide. pulse radiolysis study of CF_3 radical reactions. *J. Phys. Chem. A*, 106(22):5468–5473, 2002.

[47] C. G. HANKE, S. L. PRICE, and R. M. LYNDEN-BELL. Intermolecular potentials for simulations of liquid imidazolium salts. *Mol. Phys.*, 99(10):801–809, 2001.

[48] C. Hardacre, J. D. Holbrey, M. Nieuwenhuyzen, and T. G. A. Youngs. Structure and solvation in ionic liquids. *Acc. Chem. Res.*, 40(11):1146–1155, 2007.

[49] R. Hayes, S. Imberti, G. G. Warr, and R. Atkin. Pronounced sponge-like nanostructure in propylammonium nitrate. *Phys. Chem. Chem. Phys.*, 13:13544–13551, 2011.

[50] L. M. Helene Olivier-Bourbigou. Ionic liquids: perspectives for organic and catalytic reactions. *J. Mol. Catal. A*, 182Äì183(0):419 – 437, 2002.

[51] K. M. Hong and J. Noolandi. Solution of the smoluchowski equation with a coulomb potential. i. general results. *J. Chem. Phys.*, 68(11):5163–5171, 1978.

[52] P. Howlett, E. Izgorodina, and e. a. Forsyth, M. Electrochemistry at negative potentials in bis(trifluoromethanesulfonyl)amide ionic liquids. *Z. Phys. Chem.*, 220(10):1483–1498, 2006.

[53] P. C. Howlett, N. Brack, A. F. Hollenkamp, M. Forsyth, and D. R. MacFarlane. Characterization of the lithium surface in n-methyl-n-alkylpyrrolidinium bis(trifluoromethanesulfonyl)amide room-temperature ionic liquid electrolytes. *J. Electrochem. Soc.*, 153(3):A595–A606, 2006.

[54] Z. Hu and C. J. Margulis. Heterogeneity in a room-temperature ionic liquid: Persistent local environments and the red-edge effect. *Proc. Natl. Acad. Sci. U.S.A.*, 103(4):831–836, 2006.

[55] Z. Hu and C. J. Margulis. Room-temperature ionic liquids: Slow dynamics, viscosity, and the red edge effect. *Acc. Chem. Res.*, 40(11):1097–1105, 2007.

[56] X. Huang, C. J. Margulis, Y. Li, and B. J. Berne. Why is the partial molar volume of co2 so small when dissolved in a room temperature ionic liquid? structure and dynamics of co2 dissolved in [bmim+] [pf6-]. *J. Am. Chem. Soc.*, 127(50):17842–17851, 2005.

[57] H. Iglev, A. Trifonov, A. Thaller, I. Buchvarov, T. Fiebig, and A. Laubereau. Photoionization dynamics of an aqueous iodide solution: the temperature dependence. *Chem. Phys. Lett.*, 403(1 - 3):198 – 204, 2005.

[58] J. R. James F. Wishart, Edward W. Castner. The physical chemistry of ionic liquids. *J. Phys. Chem. B*, 111(18):4639–4640, 2007.

[59] H. Jin, X. Li, and M. Maroncelli. Heterogeneous solute dynamics in room temperature ionic liquids. *J. Phys. Chem. B*, 111(48):13473–13478, 2007.

[60] H. Jin, X. Li, and M. Maroncelli. Heterogeneous solute dynamics in room-temperature ionic liquids. (addition and correction). *J. Phys. Chem. B*, 114(34):11370–11370, 2010.

[61] H. Jin, B. O'Hare, J. Dong, S. Arzhantsev, G. A. Baker, J. F. Wishart, A. J. Benesi, and M. Maroncelli. Physical properties of ionic liquids consisting of the 1-butyl-3-methylimidazolium cation with various anions and the bis(trifluoromethylsulfonyl)imide anion with various cations. *J. Phys. Chem. B*, 112(1):81–92, 2008. PMID: 18069817.

[62] M. Kanakubo, K. R. Harris, N. Tsuchihashi, K. Ibuki, and M. Ueno. Effect of pressure on transport properties of the ionic liquid 1-butyl-3-methylimidazolium hexafluorophosphate. *J. Phys. Chem. B*, 111(8):2062–2069, 2007.

[63] F. Karadas, M. Atilhan, and S. Aparicio. Review on the use of ionic liquids (ils) as alternative fluids for co2 capture and natural gas sweetening. *Energy & Fuels*, 24(11):5817–5828, 2010.

[64] H. K. Kashyap, J. J. Hettige, H. V. R. Annapureddy, and C. J. Margulis. Saxs anti-peaks reveal the length-scales of dual positive-negative and polar-apolar ordering in room-temperature ionic liquids. *Chem. Commun.*, 48:5103–5105, 2012.

[65] H. K. Kashyap, C. S. Santos, H. V. R. Annapureddy, N. S. Murthy, C. J. Margulis, and E. W. Castner, Edward W. Jr. Temperature-dependent structure of ionic liquids: X-ray scattering and simulations. *Faraday Discuss.*, 154:133–143, 2012.

[66] H. K. Kashyap, C. S. Santos, N. S. Murthy, J. J. Hettige, K. Kerr, S. Ramati, J. Gwon, M. Gohdo, S. I. Lall-Ramnarine, J. F. Wishart, C. J. Margulis, and E. W. Castner. Structure of 1-alkyl-1-methylpyrrolidinium bis(trifluoromethylsulfonyl)amide ionic liquids with linear, branched, and cyclic alkyl groups. *J. Phys. Chem. B*, 117(49):15328–15337, 2013.

[67] R. Katoh, Y. Yoshida, Y. Katsumura, and K. Takahashi. Electron photodetachment from iodide in ionic liquids through charge-transfer-to-solvent band excitation. *J. Phys. Chem. B*, 111(18):4770–4774, MAY 10 2007.

[68] B. Kirchner. Ionic liquids from theoretical investigations. In B. Kirchner, editor, *Ionic Liquids*, volume 290 of *Topics in Current Chemistry*, pages 213–262. Springer Berlin Heidelberg, 2010.

[69] J. A. Kloepfer, V. H. Vilchiz, V. A. Lenchenkov, A. C. Germaine, and S. E. Bradforth. The ejection distribution of solvated electrons generated by the one-photon photodetachment of aqueous i- and two-photon ionization of the solvent. *J. Chem. Phys.*, 113(15):6288–6307, 2000.

[70] M. N. Kobrak. Characterization of the solvation dynamics of an ionic liquid via molecular dynamics simulation. *J. Chem. Phys.*, 125(6):–, 2006.

[71] M. N. Kobrak. A comparative study of solvation dynamics in room-temperature ionic liquids. *J. Chem. Phys.*, 127(18):–, 2007.

[72] M. N. Kobrak. *The Chemical Environment of Ionic Liquids: Links Between Liquid Structure, Dynamics, and Solvation*, pages 85–138. John Wiley & Sons, Inc., 2008.

[73] M. N. Kobrak and V. Znamenskiy. Solvation dynamics of room-temperature ionic liquids: evidence for collective solvent motion on sub-picosecond timescales. *Chem. Phys. Lett.*, 395(1 - 3):127 – 132, 2004.

[74] T. Kondoh, A. Asano, J. Yang, K. Norizawa, K. Takahashi, M. Taguchi, R. Nagaishi, R. Katoh, and Y. Yoshida. Pulse radiolysis study of ion-species effects on the solvated electron in alkylammonium ionic liquids. *Radiat. Phys. Chem.*, 78(12):1157–1160, 2009.

[75] I. Krossing, J. M. Slattery, C. Daguenet, P. J. Dyson, A. Oleinikova, and H. Weingaertner. Why are ionic liquids liquid? a simple explanation based on lattice and solvation energies. *J. Am. Chem. Soc.*, 128(41):13427–13434, 2006.

[76] J. Larsen, D. Madsen, J.-A. Poulsen, T. D. Poulsen, S. R. Keiding, and J. Thogersen. The photoisomerization of aqueous icn studied by subpicosecond transient absorption spectroscopy. *The Journal of Chemical Physics*, 116(18):7997–8005, 2002.

[77] Z. Lei, C. Dai, and B. Chen. Gas solubility in ionic liquids. *Chem. Rev.*, 114(2):1289–1326, 2014.

[78] S. Li, J. L. Banuelos, J. Guo, L. Anovitz, G. Rother, R. W. Shaw, P. C. Hillesheim, S. Dai, G. A. Baker, and P. T. Cummings. Alkyl chain length and temperature effects on structural properties of pyrrolidinium-based ionic liquids: A combined atomistic simulation and small-angle x-ray scattering study. *J. Phys. Chem. Lett.*, 3(1):125–130, 2012.

[79] R. Lian, D. A. Oulianov, R. A. Crowell, I. A. Shkrob, X. Chen, and S. E. Bradforth. Electron photodetachment from aqueous anions. 3. dynamics of geminate pairs derived from photoexcitation of mono- vs polyatomic anions. *J. Phys. Chem. A*, 110(29):9071–9078, 2006. PMID: 16854017.

[80] S. R. Logan, R. Bonneau, J. Joussot-Dubien, and P. F. de Violet. Solvent-iodine atom charge transfer absorption in liquid alkanes and cycloalkanes. *J. Chem. Soc., Faraday Trans. 1*, 71:2148–2155, 1975.

[81] F. H. Long, X. Shi, H. Lu, and K. B. Eisenthal. Electron photodetachment from halide ions in solution: Excited-state dynamics in the polarization well. *J. Phys. Chem.*, 98(30):7252–7255, 1994.

[82] E. J. Maginn. *Atomistic Simulation of Ionic Liquids*, pages 421–493. John Wiley & Sons, Inc., 2009.

[83] P. K. Mandal, M. Sarkar, and A. Samanta. Excitation-wavelength-dependent fluorescence behavior of some dipolar molecules in room-temperature ionic liquids. *J. Phys. Chem. A*, 108(42):9048–9053, 2004.

[84] A. Marcinek, J. Zielonka, J. G©bicki, C. M. Gordon, and I. R. Dunkin. Ionic liquids: A novel media for characterization of radical ions. *J. Phys. Chem. A*, 105(40):9305–9309, 2001.

[85] C. J. Margulis. Computational study of imidazolium-based ionic solvents with alkyl substituents of different lengths. *Mol. Phys.*, 102(9-10):829–838, 2004.

[86] C. J. Margulis, H. V. R. Annapureddy, P. M. De Biase, D. Coker, J. Kohanoff, and M. G. Del Pópolo. Dry excess electrons in room-temperature ionic liquids. *J. Am. Chem. Soc.*, 133(50):20186–20193, 2011.

[87] K. R. S. Martyn J. Earle. Ionic liquids. green solvents for the future. *Pure Appl. Chem.*, 72(7):1391–1398, 2000.

[88] A. Mele, G. Romano, M. Giannone, E. Ragg, G. Fronza, G. Raos, and V. Marcon. The local structure of ionic liquids: Cation - cation noe interactions and internuclear distances in neat [bmim][bf4] and [bdmim][bf4]. *Angew. Chem. Int. Ed.*, 45(7):1123–1126, 2006.

[89] E. H. M.F Fox. Correlation of the ctts solvent scale with λ max of the solvated electron. prediction of band maxima. *Chem. Phys. Lett.*, 25(4):511–514, 1974.

[90] J. R. Miller. Scavenging kinetics of electrons produced by irradiation of organic glasses; experimental evidence for long range tunneling. *J. Chem. Phys.*, 56(10):5173–5183, 1972.

[91] F. Molins i Domenech, B. FitzPatrick, A. T. Healy, and D. A. Blank. Photodetachment and electron reactivity in 1-methyl-1-butyl-pyrrolidinium bis(trifluoromethylsulfonyl)amide. *J. Chem. Phys.*, 137(3):–, 2012.

[92] R. M. Musat, T. Kondoh, Y. Yoshida, and K. Takahashi. Twin-peaks absorption spectra of excess electron in ionic liquids. *Radiat. Phys. Chem.*, 100:32–37, 2014.

[93] Y. Nagasawa and H. Miyasaka. Ultrafast solvation dynamics and charge transfer reactions in room temperature ionic liquids. *Phys. Chem. Chem. Phys.*, 16:13008–13026, 2014.

[94] C. Nese and A.-N. Unterreiner. Photochemical processes in ionic liquids on ultrafast timescales. *Phys. Chem. Chem. Phys.*, 12:1698–1708, 2010.

[95] S. P. Ong, O. Andreussi, Y. Wu, N. Marzari, and G. Ceder. Electrochemical windows of room-temperature ionic liquids from molecular dynamics and density functional theory calculations. *Chem. Mater.*, 23(11):2979–2986, 2011.

[96] V. I. Parvulescu and C. Hardacre. Catalysis in ionic liquids. *Chem. Rev.*, 107(6):2615–2665, 2007.

[97] Y. U. Paulechka, G. J. Kabo, A. V. Blokhin, O. A. Vydrov, J. W. Magee, and M. Frenkel. Thermodynamic properties of 1-butyl-3-methylimidazolium hexafluorophosphate in the ideal gas state. *J. Chem. Eng. Data*, 48(3):457–462, 2003.

[98] N. V. Plechkova and K. R. Seddon. Applications of ionic liquids in the chemical industry. *Chem. Soc. Rev.*, 37:123–150, 2008.

[99] T. Pott and P. Meleard. New insight into the nanostructure of ionic liquids: a small angle x-ray scattering (saxs) study on liquid tri-alkyl-methyl-ammonium bis(trifluoromethanesulfonyl)amides and their mixtures. *Phys. Chem. Chem. Phys.*, 11:5469–5475, 2009.

[100] R. Richert. Heterogeneous dynamics in liquids: fluctuations in space and time. *J. Phys. Condens. Matter*, 14(23):R703, 2002.

[101] R. D. Rogers and G. A. Voth. Ionic liquids. *Acc. Chem. Res.*, 40(11):1077–1078, 2007.

[102] S. J. Rosenthal, X. Xie, M. Du, and G. R. Fleming. Femtosecond solvation dynamics in acetonitrile: Observation of the inertial contribution to the solvent response. *J. Chem. Phys.*, 95(6):4715–4718, 1991.

[103] D. Roy and M. Maroncelli. Simulations of solvation and solvation dynamics in an idealized ionic liquid model. *J. Phys. Chem. B*, 116(20):5951–5970, 2012.

[104] O. Russina, A. Triolo, L. Gontrani, and R. Caminiti. Mesoscopic structural heterogeneities in room-temperature ionic liquids. *J. Phys. Chem. Lett.*, 3(1):27–33, 2012.

[105] E. V. Saenko, K. Takahashi, and V. I. Feldman. Epr evidence for a physically trapped excess electron in a glassy ionic liquid. *J. Chem. Phys. Lett.*, 4(17):2896–2899, 2013.

[106] A. Samanta. Dynamic stokes shift and excitation wavelength dependent fluorescence of dipolar molecules in room temperature ionic liquids. *J. Phys. Chem. B*, 110(28):13704–13716, 2006.

[107] A. Samanta. Solvation dynamics in ionic liquids: What we have learned from the dynamic fluorescence stokes shift studies. *J. Chem. Phys. Lett.*, 1(10):1557–1562, 2010.

[108] K. Santhosh and A. Samanta. Modulation of the excited state intramolecular electron transfer reaction and dual fluorescence of crystal violet lactone in room temperature ionic liquids. *J. Phys. Chem. B*, 114(28):9195–9200, 2010.

[109] C. S. Santos, H. V. R. Annapureddy, N. S. Murthy, H. K. Kashyap, E. W. Castner, and C. J. Margulis. Temperature-dependent structure of methyltributylammonium bis(trifluoromethylsulfonyl)amide: X ray scattering and simulations. *J. Chem. Phys.*, 134(6):–, 2011.

[110] C. S. Santos, N. S. Murthy, G. A. Baker, and E. W. Castner. Communication: X-ray scattering from ionic liquids with pyrrolidinium cations. *J. Chem. Phys.*, 134(12):–, 2011.

[111] J. K. Shah, J. F. Brennecke, and E. J. Maginn. Thermodynamic properties of the ionic liquid 1-n-butyl-3-methylimidazolium hexafluorophosphate from monte carlo simulations. *Green Chem.*, 4:112–118, 2002.

[112] W.-S. Sheu and P. J. Rossky. The electronic dynamics of photoexcited aqueous iodide. *Chem. Phys. Lett.*, 202(3 - 4):186 – 190, 1993.

[113] W.-S. Sheu and P. J. Rossky. Electronic and solvent relaxation dynamics of a photoexcited aqueous halide. *J. Phys. Chem.*, 100(4):1295–1302, 1996.

[114] Y. Shim, M. Y. Choi, and H. J. Kim. A molecular dynamics computer simulation study of room-temperature ionic liquids. ii. equilibrium and nonequilibrium solvation dynamics. *J. Chem. Phys.*, 122(4):–, 2005.

[115] Y. Shim, J. Duan, M. Y. Choi, and H. J. Kim. Solvation in molecular ionic liquids. *J. Chem. Phys.*, 119(13):6411–6414, 2003.

[116] H. Shirota, A. M. Funston, J. F. Wishart, and E. W. Castner. Ultrafast dynamics of pyrrolidinium cation ionic liquids. *J. Chem. Phys.*, 122(18):–, 2005.

[117] I. A. Shkrob, T. W. Marin, S. D. Chemerisov, J. L. Hatcher, and J. F. Wishart. Radiation induced redox reactions and fragmentation of constituent ions in ionic liquids. 2. Imidazolium cations. *J. Phys. Chem. B*, 115(14):3889–3902, 2011.

[118] I. A. Shkrob, T. W. Marin, S. D. Chemerisov, and J. F. Wishart. Radiation induced redox reactions and fragmentation of constituent ions in ionic liquids. 1. Anions. *J. Phys. Chem. B*, 115(14):3872–3888, 2011.

[119] I. A. Shkrob, T. W. Marin, J. L. Hatcher, A. R. Cook, T. Szreder, and J. F. Wishart. Radiation stability of cations in ionic liquids. 2. Improved radiation resistance through charge delocalization in 1-benzylpyridinium. *J. Phys. Chem. B*, 117(46):14385–14399, 2013.

[120] I. A. Shkrob and J. F. Wishart. Charge trapping in imidazolium ionic liquids. *J. Phys. Chem. B*, 113(16):5582–5592, 2009.

[121] L. D. A. Siebbeles, U. Emmerichs, A. Hummel, and H. J. Bakker. A subpicosecond pump-probe laser study of ionization and geminate charge recombination kinetics in alkane liquids. *J. Chem. Phys.*, 107(22):9339–9347, 1997.

[122] L. J. A. Siqueira and M. C. C. Ribeiro. Charge ordering and intermediate range order in ammonium ionic liquids. *J. Chem. Phys.*, 135(20):–, 2011.

[123] M. Smiglak, A. Metlen, and R. D. Rogers. The second evolution of ionic liquids: From solvents and separations to advanced materials - energetic examples from

the ionic liquid cookbook. *Acc. Chem. Res.*, 40(11):1182–1192, 2007.

[124] D. R. M. Stewart A. Forsyth, Jennifer M. Pringle. Ionic liquids - an overview. *Aust. J. Chem.*, 57(2):113–119, 2004.

[125] K. Takahashi, T. Sato, Y. Katsumura, J. Yang, T. Kondoh, Y. Yoshida, and R. Katoh. Reactions of solvated electrons with imidazolium cations in ionic liquids. *Radiat. Phys. Chem.*, 77(10-12):1239–1243, 2008.

[126] K. Takahashi, K. Suda, T. Seto, Y. Katsumura, R. Katoh, R. A. Crowell, and J. F. Wishart. Photo-detrapping of solvated electrons in an ionic liquid. *Radiat. Phys. Chem.*, 78(12):1129–1132, 2009.

[127] T. Torimoto, T. Tsuda, K.-i. Okazaki, and S. Kuwabata. New frontiers in materials science opened by ionic liquids. *Adv. Mater.*, 22(11):1196–1221, 2010.

[128] A. Triolo, O. Russina, V. Arrighi, F. Juranyi, S. Janssen, and C. M. Gordon. Quasielastic neutron scattering characterization of the relaxation processes in a room temperature ionic liquid. *J. Chem. Phys.*, 119(16):8549–8557, 2003.

[129] A. Triolo, O. Russina, B. Fazio, G. B. Appetecchi, M. Carewska, and S. Passerini. Nanoscale organization in piperidinium-based room temperature ionic liquids. *J. Chem. Phys.*, 130(16):–, 2009.

[130] A. Triolo, O. Russina, B. Fazio, R. Triolo, and E. D. Cola. Morphology of 1-alkyl-3-methylimidazolium hexafluorophosphate room temperature ionic liquids. *Chem. Phys. Lett.*, 457(4Äì6):362 – 365, 2008.

[131] Y. Umebayashi, H. Hamano, S. Seki, B. Minofar, K. Fujii, K. Hayamizu, S. Tsuzuki, Y. Kameda, S. Kohara, and M. Watanabe. Liquid structure of and li+ ion solvation in bis(trifluoromethanesulfonyl)amide based ionic liquids composed of 1-ethyl-3-methylimidazolium and n-methyl-n-propylpyrrolidinium cations. *J. Phys. Chem. B*, 115(42):12179–12191, 2011.

[132] S. M. Urahata and M. C. C. Ribeiro. Structure of ionic liquids of 1-alkyl-3-methylimidazolium cations: A systematic computer simulation study. *J. Chem. Phys.*, 120(4):1855–1863, 2004.

[133] V. H. Vilchiz, X. Chen, J. A. Kloepfer, and S. E. Bradforth. Solvent effects on geminate recombination dynamics after photodetachment. *Rad. Phys. Chem.*, 72(2 - 3):159 – 167, 2005.

[134] C. Wakai, A. Oleinikova, M. Ott, and H. Weing§rtner. How polar are ionic liquids? determination of the static dielectric constant of an imidazolium-based ionic liquid by microwave dielectric spectroscopy. *J. Phys. Chem. B*, 109(36):17028–17030, 2005.

[135] P. Walden. Ueber die molekulargroesse und elektrische leitfaehigkeit einiger geschmolzenen salze. *Bull. Acad. Imper. Sci. St. Petersbourg*, 8:405–422, 1914.

[136] Y. Wang and G. A. Voth. Unique spatial heterogeneity in ionic liquids. *J. Am. Chem. Soc.*, 127(35):12192–12193, 2005.

[137] Y. Wang and G. A. Voth. Tail aggregation and domain diffusion in ionic liquids. *J. Phys. Chem. B*, 110(37):18601–18608, 2006.

[138] H. Weingaertner, P. Sasisanker, C. Daguenet, P. J. Dyson, I. Krossing, J. M. Slattery, and T. Schubert. The dielectric response of room-temperature ionic liquids: Effect of cation variation. *J. Phys. Chem. B*, 111(18):4775–4780, 2007.

[139] H. Weingärtner. Understanding ionic liquids at the molecular level: Facts, problems, and controversies. *Angew. Chem. Int. Ed.*, 47(4):654–670, 2008.

[140] T. Welton. Room-temperature ionic liquids. solvents for synthesis and catalysis. *Chem. Rev.*, 99(8):2071–2084, 1999.

[141] S. Werner, M. Haumann, and P. Wasserscheid. Ionic liquids in chemical engineering. *Annu. Rev. Chem. Biomol. Eng.*, 1(1):203–230, 2010.

[142] J. S. Wilkes. A short history of ionic liquids-from molten salts to neoteric solvents. *Green Chem.*, 4:73–80, 2002.

[143] J. F. Wishart. *Radiation Chemistry of Ionic Liquids: Reactivity of Primary Species*, volume 856 of *ACS Symposium Series*, chapter 32, pages 381–396. ACS, 2003.

[144] J. F. Wishart. Energy applications of ionic liquids. *Energy Environ. Sci.*, 2:956–961, 2009.

[145] J. F. Wishart, A. M. Funston, T. Szreder, A. R. Cook, and M. Gohdo. Electron solvation dynamics and reactivity in ionic liquids observed by picosecond radiolysis techniques. *Faraday Discuss.*, 154:353–363, 2012.

[146] J. F. Wishart and P. Neta. Spectrum and reactivity of the solvated electron in the ionic liquid methyltributylammonium bis(trifluoromethylsulfonyl)imide. *J. Phys. Chem. B*, 107(30):7261–7267, 2003.

[147] D. Xiao, L. G. Hines, S. Li, R. A. Bartsch, E. L. Quitevis, O. Russina, and A. Triolo. Effect of cation symmetry and alkyl chain length on the structure and intermolecular dynamics of 1,3-dialkylimidazolium bis(trifluoromethanesulfonyl)amide ionic liquids. *J. Phys. Chem. B*, 113(18):6426–6433, 2009.

[148] C. Xu, A. Durumeric, H. K. Kashyap, J. Kohanoff, and C. J. Margulis. Dynamics of excess electronic charge in aliphatic ionic liquids containing the bis(trifluoromethylsulfonyl)amide anion. *J. Am. Chem. Soc.*, 135(46):17528–17536, 2013.

[149] C. Xu and C. J. Margulis. Solvation of an excess electron in pyrrolidinium dicyanamide based ionic liquids. *J. Phys. Chem. B*, 119(2):532–542, 2015.

[150] J. Yan, Q. Wang, T. Wei, and Z. Fan. Recent advances in design and fabrication of electrochemical supercapacitors with high energy densities. *Adv. Energy Mater.*, 4(4):1300816, 2014.

[151] M. T. Zafarani-Moattar and R. Majdan-Cegincara. Viscosity, density, speed of sound, and refractive index of binary mixtures of organic solvent + ionic liquid, 1-butyl-3-methylimidazolium hexafluorophosphate at 298.15 k. *J. Chem. Eng. Data*, 52(6):2359–2364, 2007.

[152] X.-X. Zhang, M. Liang, N. P. Ernsting, and M. Maroncelli. Complete solvation response of coumarin 153 in ionic liquids. *J. Phys. Chem. B*, 117(16):4291–4304, 2013.

Chapter 7

Appendices

7.1 REFERENCE VALUES OF THE PHYSICAL PROPERTIES OF THE RTILs USED.

RTIL	MW (g/mol)	R(NTf_2^-) ($\AA$)	R($Py_{1,x}^+$) ($\AA$)	η (cP)	ρ (g/cm^3)	n_D	ϵ_∞
$[Py_{1,3}^+][NTf_2^-]$	408.3	3.37	3.31	73	1.40	1.420	
$[Py_{1,4}^+][NTf_2^-]$	422.4	3.37	3.43	91	1.39	1.423	11.7
$[Py_{1,6}^+][NTf_2^-]$	450.4	3.37	3.65	137	1.32	1.425	
$[Py_{1,10}^+][NTf_2^-]$	506.5	3.37	4.01	236	1.25	1.431	

Table 7.1: Physical properties of the $[Py_{1,x}^+][NTf_2^-]$ ILs. All value except Dielectric constant are from ref. [152]. Dielectric constant for $[Py_{1,4}^+][NTf_2^-]$ from ref. [138]

7.2 3D-PRINTED CELL HOLDER DESIGN.

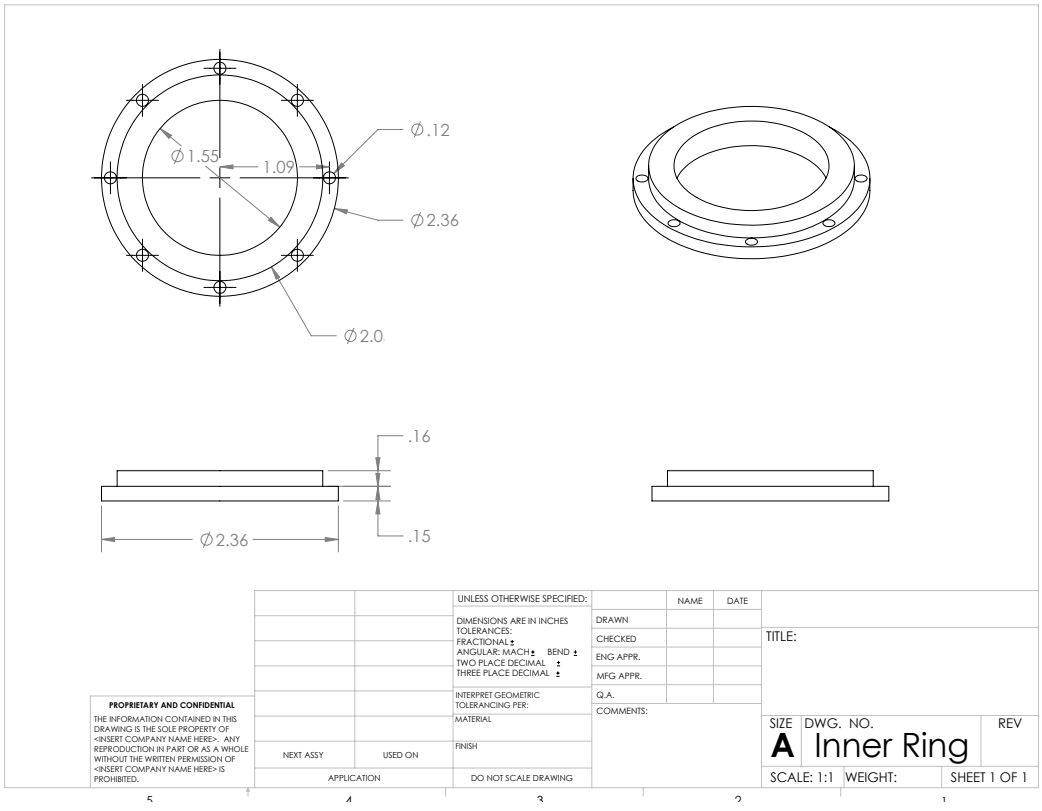

Figure 7.1: Design of the inner ring of the 3D-printed cell holder.

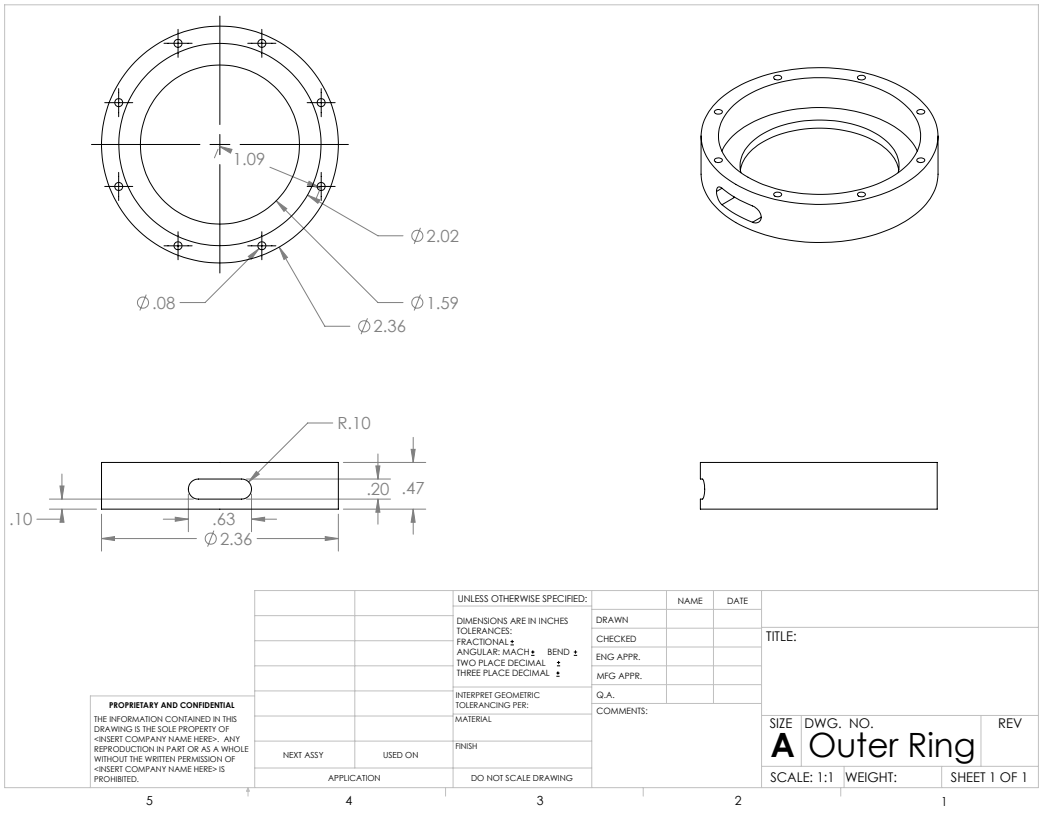

Figure 7.2: Design of the outer ring of the 3D-printed cell holder.

7.3 APPENDIX TO CHAPTER 4

7.3.1 Estimating the concentration of N_2O at saturation.

The concentration of N_2O in the RTILs we can only estimate, given that the Henry constant for this gas has only been measured in a few ionic liquids. [6]Assuming that its value does not differ greatly from that in $[Im^+_{1,4}][NTf^-_2]$ (the values for O_2 and CO_2 are within $\approx 15\%$ of each other in $[bmim^+][NTf^-_2]$ and $[Py^+_{1,4}][NTf^-_2]$) and that are the roughly the same for $[Py^+_{1,4}][NTf^-_2]$ as for $[Py^+_{1,3}][NTf^-_2]$, $[Py^+_{1,6}][NTf^-_2]$ and $[Py^+_{1,10}][NTf^-_2]$, we obtain a N_2O saturation concentration of 90 mM.

7.3.2 Kinetics of Remaining Signal

The evolution of the *fraction of remaining signal*, which is the ratio of the signal at each time delay and color with and without the presence of the N_2O quencher, are shown here:

Probe (eV)	τ_a (ps)	A	τ_b (ns)	B
2.48	1.3×10^3	0.754		
	(-1.5 – 29) $\times 10^3$	(0.74 – 0.77)		
2.07	4.0	0.132	3.0	0.72
	(0.26 – 7.8)	(0.09 – 0.18)	(1.7 – 4.3)	(0.68 – 0.76)
1.77	0.85	0.31	5.6	0.60
	(0.56 – 1.14)	(0.26 – 0.36)	(1.4 – 9.7)	(0.58 – 0.63)
1.38	0.52	0.547	3.1	0.46
	(0.48 – 0.57)	(0.52 – 0.57)	(2.3 – 3.8)	(0.45 – 0.47)
1.13	0.63	0.40	2.8	0.4
	(0.52 – 0.74)	(0.37 – 0.44)	(1.8 – 3.9)	(0.42 – 0.45)
0.95	0.39	0.59	2.7	0.28
	(0.33 – 0.46)	(0.53 – 0.64)	(0.9 – 4.4)	(0.26 – 0.30)

Table 7.2: Optimized fitting parameters for the $[Py^+_{1,3}][NTf^-_2]$ data presented in Fig. 7.3. The data was fitted to the sum of two exponential decays, $Ae^{-t/\tau_a} + Be^{-t/\tau_b}$. Error bounds are presented as the 68% confidence interval when all parameters are simultaneously optimized.

Probe (eV)	τ_a (ps)	A	τ_b (ns)	B
2.48	6.2	0.29		
	(3.5 – 8.8)	(0.25 – 0.34)		
2.07	5.9	0.31	5.9	0.61
	(3.8 – 7.9)	(0.27 – 0.34)	(0.9 – 11)	(0.57 – 0.64)
1.77	5.6	0.229	6.5	0.68
	(3.7 – 7.4)	(0.20 – 0.26)	(2.6 – 10)	(0.65 – 0.70)
1.38	0.49	0.593		
	(0.40 – 0.57)	(0.51 – 0.68)		
1.13	0.42	0.81	7.3	0.37
	(0.35 – 0.48)	(0.69 – 0.92)	(-0.04 – 15)	(0.36 – 0.39)
0.95	0.51	0.59	3.9	0.37
	(0.43 – 0.59)	(0.52 – 0.66)	(2.1 – 5.9)	(0.36 – 0.39)

Table 7.3: Optimized fitting parameters for the $[Py^+_{1,6}][NTf^-_2]$ data presented in Fig. 7.3. The data was fitted to the sum of two exponential decays, $Ae^{-t/\tau_a} + Be^{-t/\tau_b}$. Error bounds are presented as the 68% confidence interval when all parameters are simultaneously optimized.

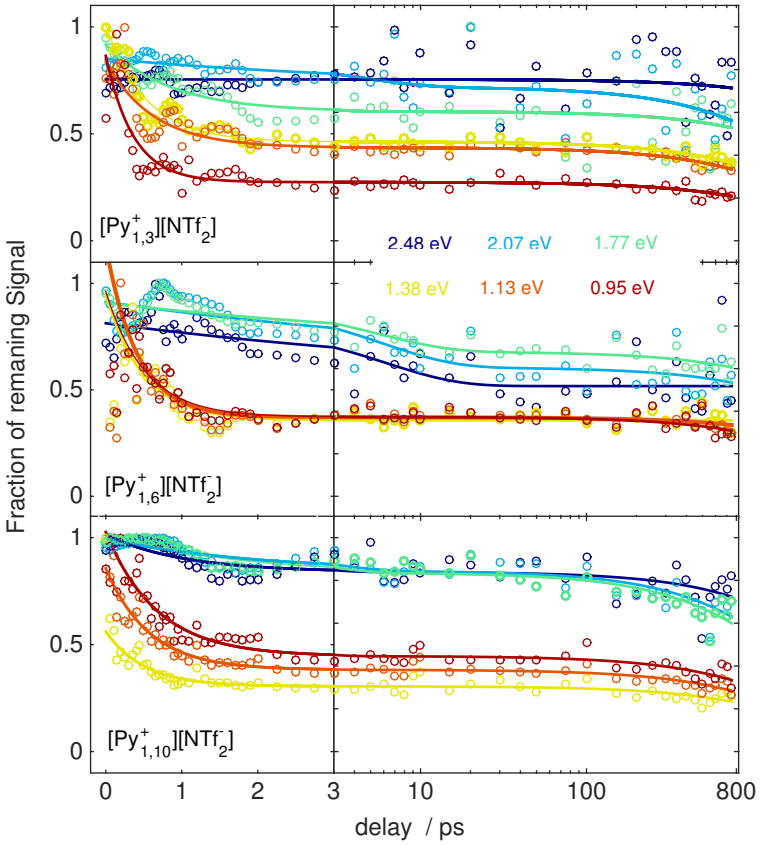

Figure 7.3: Ratio of probe signal between RTILs saturated with N_2 vs. saturated with N_2O at a series of probe energies. The open circles are the data. The data were fitted to a sum of two exponential decays, shown as the solid lines, and the optimized fitting parameters are presented in Tables 7.2, 7.3, and 7.4 below.

Probe (eV)	τ_a (ps)	A	τ_b (ns)	B
2.48	1.02	0.17	5.0	0.84
	(0.64 – 1.39)	(0.14 – 0.20)	(3.5 – 6.6)	(0.82 – 0.86)
2.07	1.91	0.15	2.6	0.84
	(1.26 – 2.56)	(0.13 – 0.17)	(2.2 – 2.9)	(0.83 – 0.86)
1.77	1.56	0.19	2.3	0.84
	(1.19 – 1.92)	(0.17 – 0.21)	(2.0 – 2.5)	(0.82 – 0.85)
1.38	0.50	0.26	2.8	0.31
	(0.42 – 0.59)	(0.23 – 0.28)	(2.1 – 3.5)	(0.30 – 0.31)
1.13	0.57	0.47	2.5	0.38
	(0.50 – 0.63)	(0.44 – 0.51)	(2.0 – 3.1)	(0.37 – 0.39)
0.95	0.67	0.58	2.6	0.45
	(0.60 – 0.75)	(0.54 – 0.62)	(1.9 – 3.3)	(0.43 – 0.46)

Table 7.4: Optimized fitting parameters for the $[Py^{+}_{1,10}][NTf^{-}_{2}]$ data presented in Fig. 7.3. The data was fitted to the sum of two exponential decays, $Ae^{-t/\tau_a} + Be^{-t/\tau_b}$. Error bounds are presented as the 68% confidence interval when all parameters are simultaneously optimized.

7.3.3 Spectrally Resolved Fraction of Signal Remaining:

The spectrally resolved relative quenching in the near-IR is shown below at several time delays. These spectra are interesting because they may indicate heterogeneity of the near-IR TA, either because not only the solvated electron absorbs there, or because there is a distribution of solvated electrons in slightly different environments. The effect appears weak and has not been further analyzed. The same spectra in the VIS might bring to light the presence of NTf_2 neutral radical long-lived visible TA that has been proposed by Wishart [146]. Slightly weaker quenching in the blue part of the spectrum would agree with Wishart's proposal, but the effect appears weak.

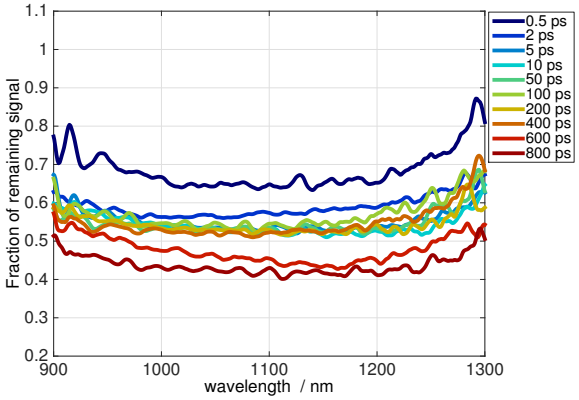

Figure 7.4: Relative spectral quenching of the near-IR TA in neat $[Py^{+}_{1,3}][NTf^{-}_{2}]$.

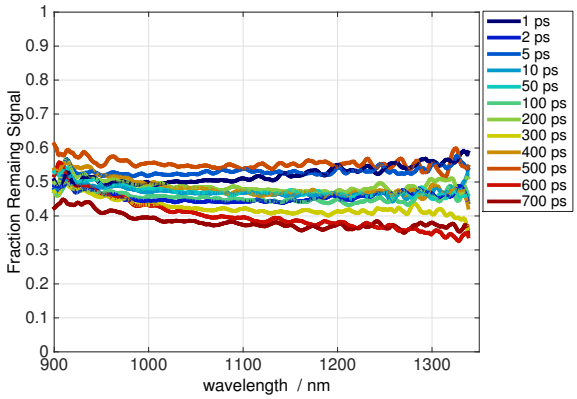

Figure 7.5: Relative spectral quenching of the near-IR TA in neat $[Py^{+}_{1,6}][NTf^{-}_{2}]$.

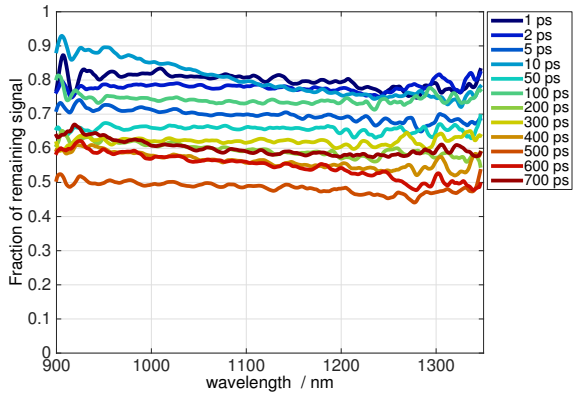

Figure 7.6: Relative spectral quenching of the near-IR TA in neat $[Py^{+}_{1,10}][NTf^{-}_{2}]$.

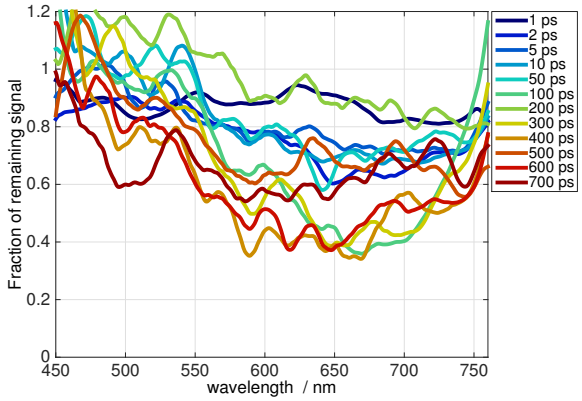

Figure 7.7: Relative spectral quenching of the VIS TA in neat $[Py^{+}_{1,3}][NTf^{-}_{2}]$.

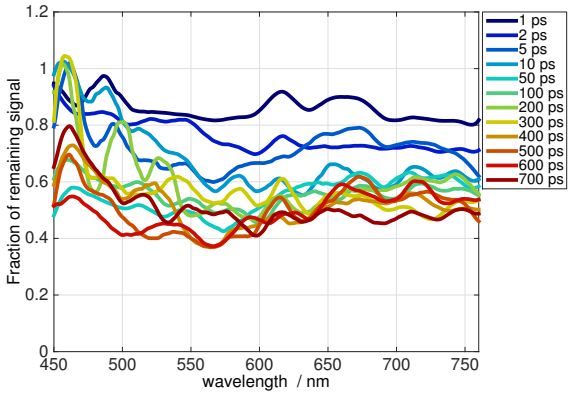

Figure 7.8: Relative spectral quenching of the VIS TA in neat $[Py^{+}_{1,6}][NTf^{-}_{2}]$.

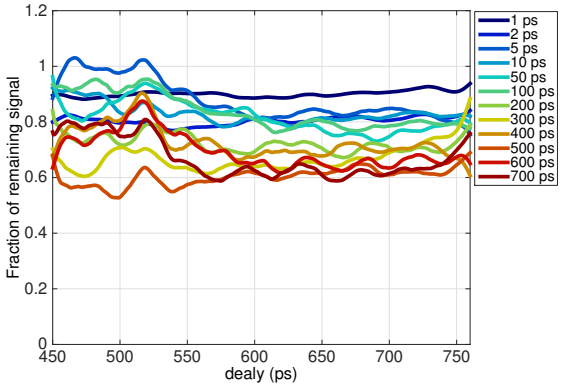

Figure 7.9: Relative spectral quenching of the VIS TA in neat $[Py^{+}_{1,10}][NTf^{-}_{2}]$.

7.4 PHOTODETACHMENT AND ELECTRON COOLING IN NEAT $[Py^+_{1,4}][NTf^-_2]$

7.4.1 Introduction

We have found that the transients induced in the neat $[Py^+_{1,4}][NTf^-_2]$ RTIL, although in qualitative agreement with those seen for $[Py^+_{1,3}][NTf^-_2]$, $[Py^+_{1,6}][NTf^-_2]$ and $[Py^+_{1,10}][NTf^-_2]$, do not follow the trends in the $[Py^+_{1,3}][NTf^-_2]$, $[Py^+_{1,6}][NTf^-_2]$ and $[Py^+_{1,10}][NTf^-_2]$ series. The results for this liquid are thus shown here separately. We have concluded that these differences are due to the different origin of this liquid (Iolitec) compared to the other three, which were prepared by our collaborator Gary Baker. [61]. We see below how the UV absorption of this liquid is higher than expected vis a vis the UV absorption spectra of the other three. Also, the evolution of the UV absorption spectrum as it is sequentially purified with activated carbon, seems to indicate that there is some impurity that the activated carbon cannot extract.

7.4.2 Experimental

As opposed the other three ILs, which were made available to us by our collaborator Gary Baker, the $[Py^+_{1,4}][NTf^-_2]$ RTIL was obtained from Iolitec (99.5 %, IL-0035-UP-0050), and was purified with activated carbon (Aldrich, DARCO (R)) according the standard procedure described in the previous chapter. The absorption spectra of the progressively cleaned liquid is shown in Figure 7.10. The twice cleaned liquid was

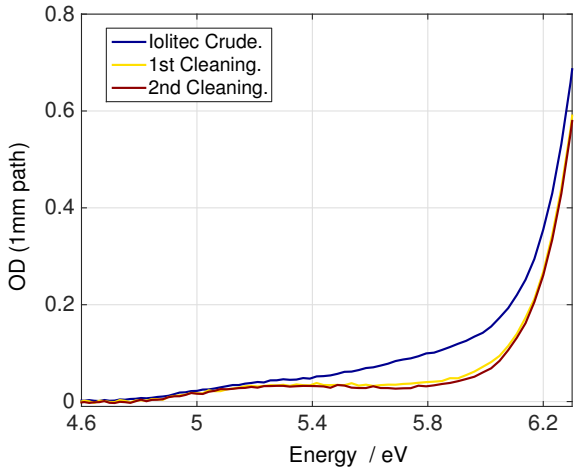

Figure 7.10: Absorption spectra of the consecutive cleanings of the $[Py^{+}_{1,4}][NTf^{-}_{2}]$ sample from Iolitec.

subjected to the same drying in a sand bath (6 days, 70 °C – 80 °C under vacuum) and transferred into the glove box as for the other three liquids as described in the previous chapter. Similarly, all sample handling procedures and laser setup for the experiments involving the $[Py^{+}_{1,4}][NTf^{-}_{2}]$ liquid were the same as for the other three liquids, and all these experiments were performed within 5 days. As in the experiments with the other three liquids, the 200 nm (6.2 eV) pump pulse energy was set at 450 nJ at the sample, and the IRF of the experiment was determined to be 240 fs (gaussian, fwhm). Detailed experimental information is to be found in the previous chapter.

7.4.3 Results

In Figure 7.11 the absorption spectra of the cleanest sample obtained for each of the fours RTILs is compared. Clear from the Figure is the trend in absorption onsets that the

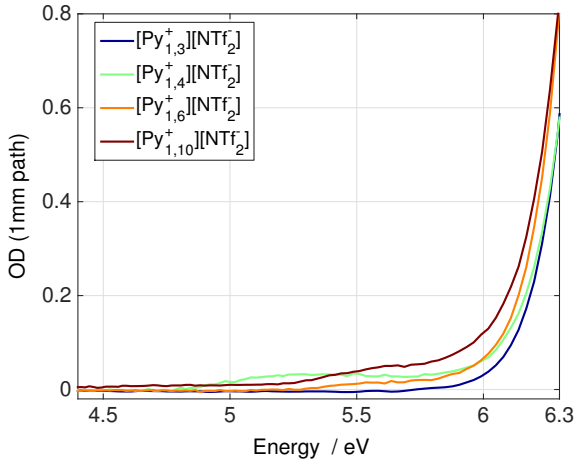

Figure 7.11: Comparison of the UV absorption spectra for the four RTILs obtained used in the 6.20 eV photolysis experiments.

series of liquids $[Py^+_{1,4}][NTf^-_2]$, $[Py^+_{1,6}][NTf^-_2]$ and $[Py^+_{1,10}][NTf^-_2]$ exhibit. $[Py^+_{1,4}][NTf^-_2]$ does not fit in the trend, its absorption being higher than expected between 5 and 5.5 eV. This, along with the evolution of the absorption spectra with successive cleanings shown in Figure 7.10, seems to indicate that the Iolitec sample includes some impurity which cannot be removed by our procedure. The identity of this impurity has not been ascertained.

TA spectra in the NIR and VIS parts of the spectrum at a series of delay times are shown in Fig. 7.12. These TAs are in qualitative agreement with those measured in the other three liquids. In particular the well resolved appearance of the NIR TA followed by a clear blue shift, and the very large TA present in the bluer part of the VIS window and its rapid decay. More detailed kinetic information is shown in Figure 7.13, where the normalized kinetic traces at individual probe energies for the three RTILs. Of

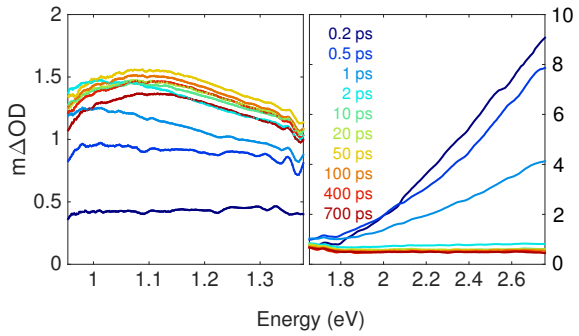

Figure 7.12: Transient absorption in neat $[Py^{+}_{1,4}][NTf^{-}_{2}]$ following excitation at 6.20 eV. Note that the ΔOD axis in the near-IR probe range is five times smaller than in the visible probe range.

particular interest is the trace at 2.48 eV, which represents the kinetics of the large early transient common to the four ILs. As can be seen in Table 7.5, at this probe energy the signal appears with a sub 100 fs time constant, as in the case of the other ILs, and the initial fast decay has a time constant of 0.62 ps, also in agreement with those found in the other 3 liquids (0.62 ps, 0.76 ps and 0.66 ps for $[Py^{+}_{1,3}][NTf^{-}_{2}]$, $[Py^{+}_{1,6}][NTf^{-}_{2}]$ and $[Py^{+}_{1,10}][NTf^{-}_{2}]$ respectively). The final amplitude of this transient ($\sim$8% of the max) is also comparable to that found in the other three liquids ($\sim$4%) . Thus, the dynamics of this early transient, which we have attributed to charge transfer transitions between the dissociation fragments of the NTf^{2-}_{2} dianion, are the same as in the other three ILs.

As in the case of the other three ILs, the integrated near-IR transient absorption rise is resolved, and is well fitted by a single exponential rise convoluted over 240 fs IRF with a time constant of 0.56 ps. See Figure 7.14. This 0.56 ps time constant is comparable to those found in the other three liquids.

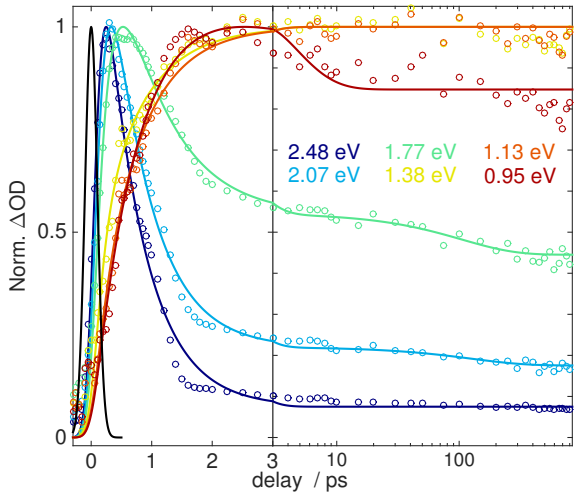

Figure 7.13: Induced TAs at selected probe energies. Open circles are the raw data and the lines are the fits using a kinetic scheme of either 2 or 3 sequential steps. Optimized fitting parameters are listed in Table 7.5

The spectral evolution of the near-IR transients is shown in Fig. 7.15, where the TA spectra have been normalized to the same maximum value, the region around the maxima isolated, and then fitted to a cubic polynomial. Using these cubic fits the maxima of the different transients are tracked. As in the other liquids, the spectra at probe delays less than 2 ps are not included in the analysis due to the lack of a clearly defined maximum. The time dependence of the $E_{\max}$ values are fitted with a time independent offset to represent the initial value at a delay of 2 ps and a single exponential rise, as shown in Figure 7.16. The optimized fitting parameters are listed in Table 7.6. This evolution of $E_{\max}$ differs significantly from that found in the other three liquids. In the first place, the initial value at 2 ps is slightly above that of the $[Py^{+}_{1,3}][NTf^{-}_{2}]$ liquids, whereas the trend followed by the other 3 liquids would makes us

Probe (eV)	τ_1(ps)	w_B	τ_2(ps)	w_C	τ_3 (ps)	w_D
2.48	0.072 (0.066 – 0.078)	1.53 (1.50 – 1.57)	0.63 (0.61 – 0.65)	0.080 (0.074 – 0.085)		
2.07	0.130 (0.123 – 0.138)	1.47 (1.44 – 1.51)	0.65 (0.62 – 0.68)	0.215 (0.208 – 0.223)	126 (21 – 231)	0.172 (0.164 – 0.180)
1.77	0.213 (0.193 – 0.233)	1.48 (1.40 – 1.56)	0.81 (0.71 – 0.90)	0.57 (0.56 – 0.58)	105 (47 – 163)	0.465 (0.454 – 0.477)
1.38	0.152 (0.050 – 0.240)	0.46 (0.27 – 0.64)	0.73 (0.49 – 0.97)	0.870 (0.859 – 0.880)		
1.13	0.18 (-0.04 – 0.40)	0.32 (-0.06 – 0.69)	0.69 (0.51 – 0.87)	0.895 (0.886 – 0.907)		
0.95	0.78 (0.66 – 0.91)	1.21 (1.07 – 1.34)	3.1 (1.6 – 4.6)	0.855 (0.843 – 0.869)		

Table 7.5: Optimized fitting parameters of the single color traces presented in Fig. 7.23. Error bounds are presented as the 68% confidence interval when all parameters were simultaneously optimized.

expect it to be between that of $[Py^+_{1,3}][NTf^-_2]$ and $[Py^+_{1,6}][NTf^-_2]$. Besides, the evolution is clearly bimodal, whereas in the other three liquids the data is well represented by a single exponential rise.

We also find that the (weighted) average rate constant of the two exponentials is k_{aver} = 0.099 ps^{-1}, about three times faster than that of the $[Py^+_{1,3}][NTf^-_2]$ liquid, and thus it does not fit in the excellent linear trend of k_{aver} vs diffusion constant that the other three liquids exhibit.

H (eV)	τ_1 (ps)	A (eV)	τ_2 (ps)	B (eV)
1.05 (0.93–1.16)	6.5 (-61–74)	0.036 (-0.12–0.19)	339 (-9600–10200)	0.02 (-0.16–0.24)

Table 7.6: Fitting parameters of the evolution of E_{max} presented in Fig. 7.16. Data for each liquid was fitted to $H + A(1 - e^{-t/\tau_1}) + B(1 - e^{-t/\tau_2})$. Error bounds are presented as the 68% confidence interval when all parameters were simultaneously optimized.

As in the case of the other three ILs, besides the blue shift of the near-IR transient,

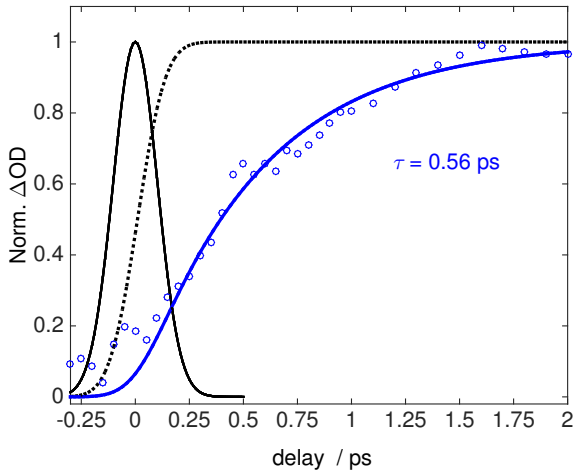

Figure 7.14: Integrated TA in probe energy range 0.95–1.38 eV up to a delay of 2 ps. The open circles are the data and the solid line is an optimized fits to a single exponential rise convoluted over the instrument response function. The instrument response is shown with the thin black line and the thick black line presents a Heaviside function convoluted with the instrument response for comparison. The time optimized time constant is 0.56 ± 0.03.

there is a narrowing of the band. As a rough measure of this we use the square root of the second moment, RMSD, of the TA between 0.95 eV and 1.38 eV. In Figure 7.17 this RMSD is plotted as a function of probe delay and is fitted to the sum of two exponential decays, and Table 7.7 shows the optimized fitting parameters. As found in the other three liquids, the narrowing is clearly bimodal, with an initial sub-ps component followed by one of ∼50ps. Although also bimodal, the two components found in the other three liquids are significantly slower, the faster one being a few ps and the slower one, much too slow to determine with accuracy.

As in the other three ILs, TA measurements were repeated after being saturated with N_2O. The effect of the quencher is shown in terms of the fraction of remaining

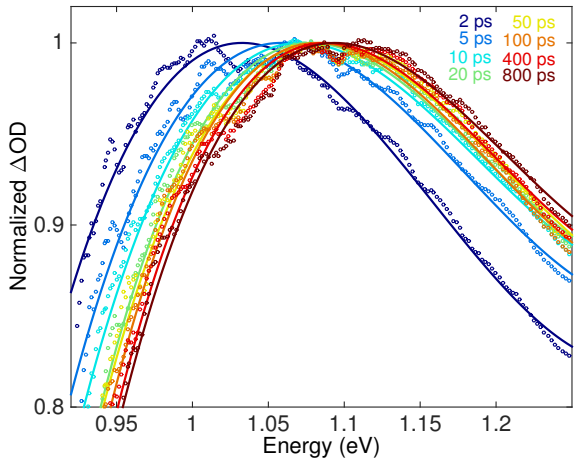

Figure 7.15: TA scaled to the maximum value and fitted to determine the energy at the maximum TA intensity as a function of probe delay, which is plotted in Fig. 7.16.

τ_a (ps)	A (eV)	τ_b (ns)	B (eV)	H (eV)
0.39	0.00060	49	0.0011	0.1187
(0.25–0.53)	(0.00050–0.00070)	(42–56)	(0.0010–0.0013)	(0.0187–0.0187)

Table 7.7: Fitting parameters for the evolution of the RMSD of the near-IR TA between 0.95 eV to 1.38 eV, shown in Fig. 7.17. The data was fitted to the sum of two exponential decays, $Ae^{-t/\tau_a} + Be^{-t/\tau_b}$ plus a Heaviside function of amplitude H. Error bounds are presented as the 68% confidence interval when all parameters were simultaneously optimized.

signal, that is, the TA in the presence of N_2O divided by the TA when there is no quencher, this ratio being normalized at time zero. The fraction of signal remaining is plotted as a function of probe delay in Figure 7.22. In the figure it can be seen that around 60% of the near-IR signal, as in the other three liquids, is quenched with a ∼0.5 ps time constant. On the other hand the quenching of the VIS TA behaves very differently: $[Py^+_{1,4}][NTf^-_2]$ exhibits a sub-ps component with a significant weight of about 40%, whereas in the other three liquids the effect of the N_2O on the VIS TA was very minor.

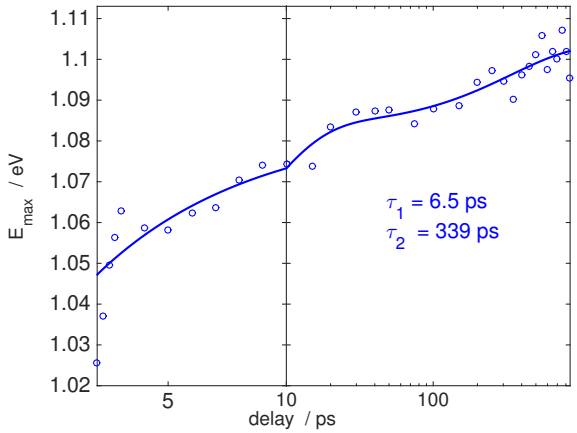

Figure 7.16: Evolution of the maximum in the near-IR TA as a function of delay time. The data is fitted to the sum of a time independent offset and a two exponential rises. Note that the time axis is linear from 2 to 50 ps and logarithmic from 50 to 850 ps. The fitting parameters are listed in Table 7.6.

Spectral Region	τ_a (ps)	A	τ_b (ns)	B
0.95–1.38 eV	0.65 (0.59–0.71)	0.56 (0.54–0.59)	3.5 (2.5–4.5)	0.40 (0.39–0.42)
2.07–2.58 eV	0.82 (0.72–0.92)	0.48 (0.45–0.51)	2.6 (2.1–3.1)	0.58 (0.57–0.59)

Table 7.8: Fitting parameters for the fraction of remaining near-IR TA and VIS presented in Fig. 7.22. The data was fitted to the sum of two exponential decays, $S(t) = Ae^{-t/\tau_a} + Be^{-t/\tau_b}$. Error bounds are presented as the 68% confidence interval when all parameters were simultaneously optimized.

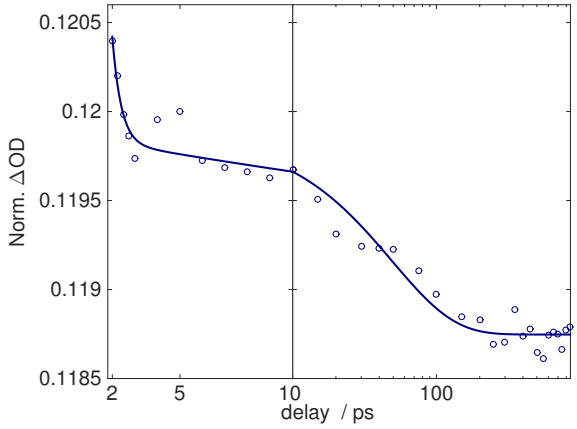

Figure 7.17: Time dependence of the width of the near-IR transient absorption band. Plotted is the standard deviation of the TA determined in the range 0.95 eV to 1.38 eV. The circles are the data and the solid lines are biexponential fits with the optimized fitting parameters listed in Table 7.7

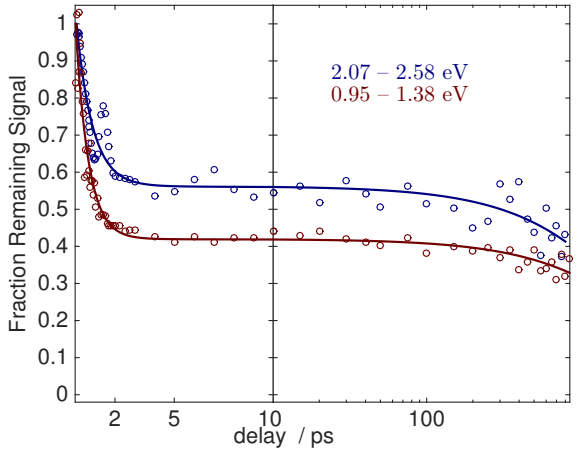

Figure 7.18: Fraction of the signal integrated over the near-IR probe region of 0.95–1.38 eV (maroon) and the visible region of 2.07–2.58 eV (blue) remaining when the RTILs are saturated with the electron scavenger N_2O. The solid lines are biexponential decay fits and optimized fitting parameters are listed in Table 7.9.

7.5 APPENDIX TO CHAPTER 5

The coincidence of the UV absorption spectra of Bu_4N^+ I^- and K^+I^- in MeOH, indicate that there is no contribution from the Bu_4N^+ ion to the absorption at 6.2 eV.

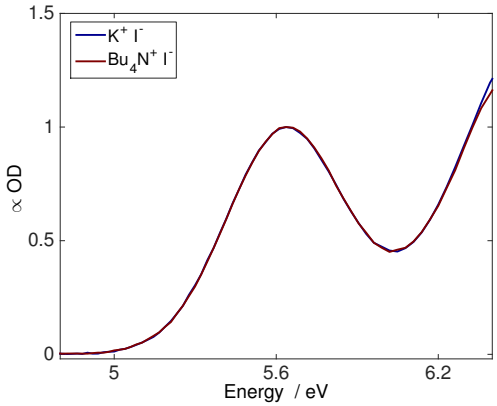

Figure 7.19: Normalized UV absorption spectrum of Bu_4N^+ I^- and K^+I^- in MeOH.

7.5.1 Fitting of RTIL I^- Solutions UV Absorption Spectra :

The absorption spectra of the $Bu_4N^+I^-$ solutions in the $[Py^+_{1,3}][NTf_2^-]$, $[Py^+_{1,6}][NTf_2^-]$ and $[Py^+_{1,10}][NTf_2^-]$ RTILs have been fitted to two gaussian functions with the a fixed separation of 0.93 eV between them plus the fixed UV absorption of the corresponding RTIL.

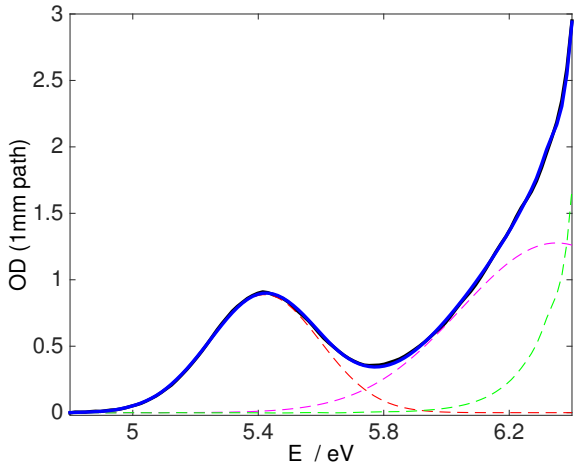

Figure 7.20: Fit of the UV Absorption Spectra of $Bu_4N^+I^-$ in $[Py^+_{1,3}][NTf^-_2]$. Dashed curves in red and magenta are the two gaussians. Green dashed line is the contribution from the $[Py^+_{1,3}][NTf^-_2]$ IL. The solid blue line is the resulting fit, and the solid black line is the absorption spectrum of the I^- solution.

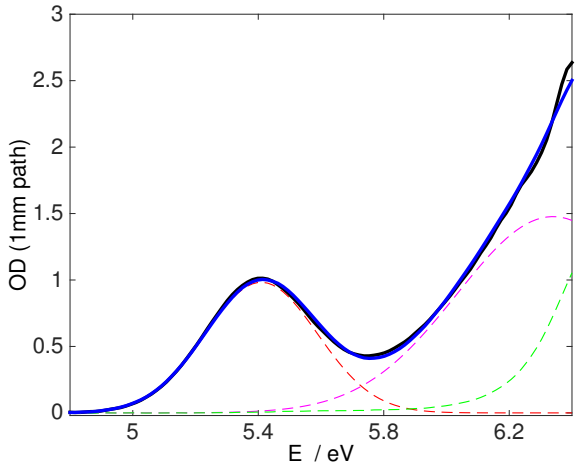

Figure 7.21: Fit of the UV Absorption Spectra of $Bu_4N^+I^-$ in $[Py^+_{1,6}][NTf^-_2]$. Dashed curves in red and magenta are the two gaussians. Green dashed line is the contribution from the $[Py^+_{1,6}][NTf^-_2]$ IL. The solid blue line is the resulting fit, and the solid black line is the absorption spectrum of the I^- solution.

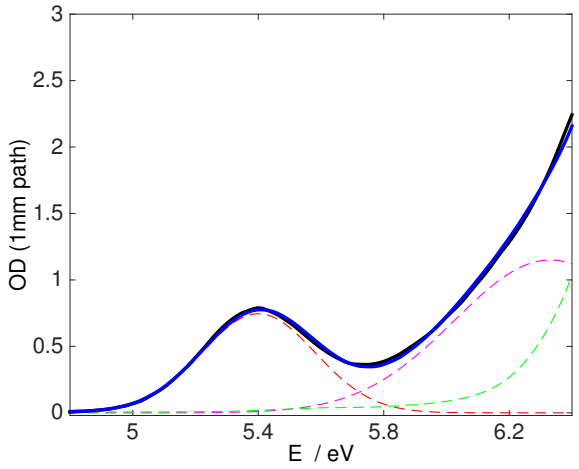

Figure 7.22: Fit of the UV Absorption Spectra of $Bu_4N^+I^-$ in $[Py^+_{1,10}][NTf_2^-]$. Dashed curves in red and magenta are the two gaussians. Green dashed line is the contribution from the $[Py^+_{1,10}][NTf_2^-]$ IL. The solid blue line is the resulting fit, and the solid black line is the absorption spectrum of the I^- solution.

RTIL	A_1	M_1 (eV)	$FWHM_1$ (eV)	A_2	M_2 (eV)	$FWHM_2$ (eV)
$[Py^+_{1,3}][NTf_2^-]$	0.886	5.421	0.416	1.277	5.421 + 0.93	0.722
$[Py^+_{1,6}][NTf_2^-]$	0.928	5.410	0.422	1.477	5.410 + 0.93	0.719
$[Py^+_{1,10}][NTf_2^-]$	0.746	5.400	0.427	1.150	5.400 + 0.93	0.716

Table 7.9: Optimized parameters to the fits of the Absorption Spectra of the RTIL I^- solutions. The two gaussian peaks are constrained to a separation of 0.93 eV, which is the energy difference between the ground sate and the spin-orbit excited state. Amplitude, Maximum and FWHM of the gaussian components are denoted by A, M and fwhm, respectively.

7.5.2 Single color traces for the three I^- solutions:

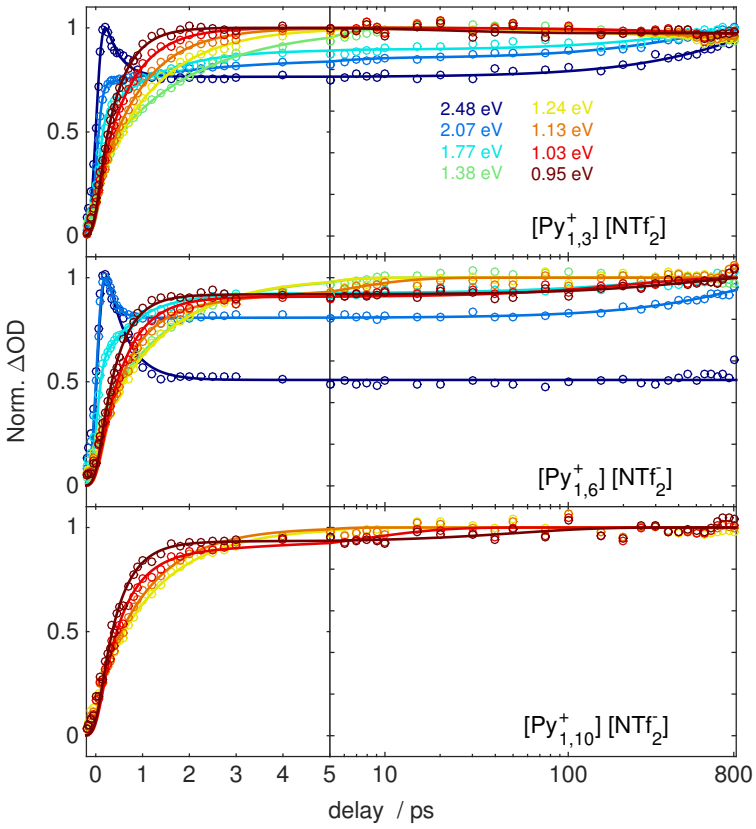

Figure 7.23: Kinetic traces at different colors for the three IL I^- solutions. The data is fit to either a 2 or 3 sequential step scheme.

Probe (eV)	τ_1 (ps)	w_B	τ_2 (ps)	w_C	τ_3 (ps)	w_D
2.48	0.00	1.2	0.30	0.759	1373	1.155
	(-1.12 – 1.12)	(-0.5 – 3.0)	(0.28 – 0.32)	(0.756 – 0.763)	(402 –2344)	(0.934 – 1.375)
2.07	0.004	0.718	2.5	0.845	590	1.04
	(-0.002 – 0.011)	(0.714 – 0.722)	(2.2 – 2.7)	(0.842 – 0.848)	(446 –734)	(1.01 – 1.06)
1.77	0.035	0.52	1.17	0.848	560	0.976
	(0.029 – 0.042)	(0.51 – 0.54)	(1.08– 1.27)	(0.842 – 0.853)	(181 –939)	(0.925 – 1.027)
1.38	0.111	0.37	1.93	0.970	162	0.943
	(0.030 – 0.193)	(0.29 – 0.46)	(1.52 – 2.35)	(0.940 – 0.999)	(-560 –885.)	(0.914 – 0.971)
1.24	0.00	0.21	1.24	0.945	262	0.888
	(-0.21 – 0.21)	(0.09 – 0.340)	(1.20 – 1.29)	(0.940 – 0.951)	(78 –446)	(0.873 – 0.904)
1.13	0.03	0.21	0.93	0.936	620	0.867
	(-0.02 – 0.09)	(0.15 – 0.26)	(0.89 – 0.96)	(0.932 – 0.941)	(-64 –1305)	(0.822 – 0.913)
1.03	0.05	0.23	0.67	0.930	643	0.8925
	(0.00 – 0.10)	(0.16 – 0.31)	(0.64 – 0.70)	(0.926 – 0.934)	(-724 –2010)	(0.843 – 0.942)
0.95	0.02	0.19	0.455	0.965	26	0.937
	(-0.10 – 0.14)	(-0.07– 0.44)	(0.425 – 0.486)	(0.958 – 0.972)	(2.2 –51)	(0.933 – 0.942)

Table 7.10: Optimized fitting parameters for the single color traces in $[Py^+_{1,3}][NTf^-_2]$ to a three sequential step kinetic scheme. Values in parenthesis show the 68% confidence intervals.

Probe (eV)	τ_1(ps)	w_B	τ_2(ps)	w_C	τ_3 (ps)	w_D
2.48	0.04	1.29	0.44	0.493		
	(0.02 – 0.05)	(1.24 – 1.33)	(0.40 – 0.48)	(0.490 – 0.496)		
2.07	0.03	1.45	0.169	0.803	1295	1.087
	(0.01 – 0.04)	(1.35 – 1.54)	(0.144 – 0.193)	(0.801 – 0.805)	(567 – 2022)	(0.963 – 1.212)
1.77	0.00	0.457	0.798	0.770	255	0.834
	(-0.035 – 0.035)	(0.443 – 0.471)	(0.751 – 0.845)	(0.767 – 0.773)	(170 – 340)	(0.827 – 0.842)
1.38	0.10	0.32	1.48	0.937		
	(0.07 – 0.12)	(0.39 – 0.34)	(1.42 – 1.53)	(0.934 – 0.939)		
1.24	0.08	0.25	1.40	0.89		
	(0.040 – 0.129)	(0.211 – 0.290)	(1.331 – 1.473)	(0.889 – 0.897)		
1.13	0.58	0.74	5.1	0.887		
	(0.54 – 0.61)	(0.72 – 0.77)	(3.7 – 6.4)	(0.883 – 0.892)		
1.03	0.56	0.83	214	0.912		
	(0.55 – 0.58)	(0.82 – 0.83)	(130 – 297)	(0.904 – 0.925)		
0.95	0.42	0.84	521	0.936		
	(0.41 – 0.43)	(0.84 – 0.84)	(145 – 896)	(0.899 – 0.975)		

Table 7.11: Optimized fitting parameters for the single color traces in $[Py^+_{1,6}][NTf^-_2]$ to a two or a three sequential step kinetic scheme. Values in parenthesis show the 68% confidence intervals

Probe (eV)	τ_1 (ps)	w_B	τ_2 (ps)	w_C
1.24	0.02	0.19	1.30	0.875
	(-0.35 – 0.39)	(-0.04 – 0.43)	(1.12 – 1.47)	(0.865 – 0.889)
1.13	0.05	0.193	1.09	0.878
	(-0.17 – 0.28)	(-0.01 – 0.398)	(0.92 – 1.27)	(0.866 – 0.890)
1.03	0.52	0.788	7.7	0.91
	(0.44 – 0.59)	(0.735 – 0.842)	(0.34 – 15.1)	(0.894 – 0.926)
0.95	0.44	0.846	54	0.910
	(0.42 – 0.46)	(0.836 – 0.856)	(15 – 93)	(0.900 – 0.918)

Table 7.12: Optimized fitting parameters for the single color traces in $[Py^{+}_{1,10}][NTf^{-}_{2}]$ to a two sequential step kinetic scheme. Values in parenthesis show the 68% confidence intervals.

7.6 I^- PHOTODETACHMENT AND ELECTRON COOLING IN $[Py^+_{1,4}][NTf^-_2]$

Similarly to the case of the neat RTILs, we have found that the dynamics following 6.2 eV photodetachment from I^- in the $[Py^+_{1,4}][NTf^-_2]$IL does not follow the trend exhibited by the other three liquids, and thus we present the data separately.

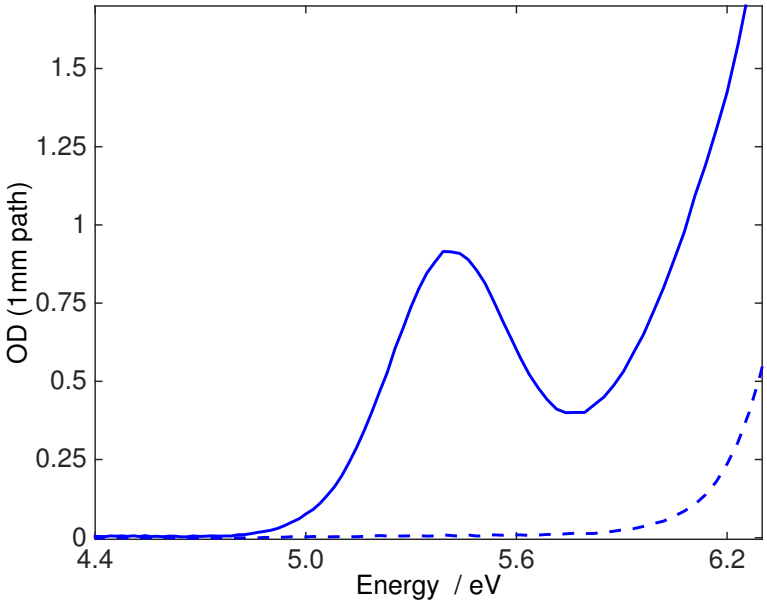

Figure 7.24: Absorption spectrum of Bu_4N^+ I^- in $[Py^+_{1,4}][NTf^-_2]$ and of neat $[Py^+_{1,4}][NTf^-_2]$.

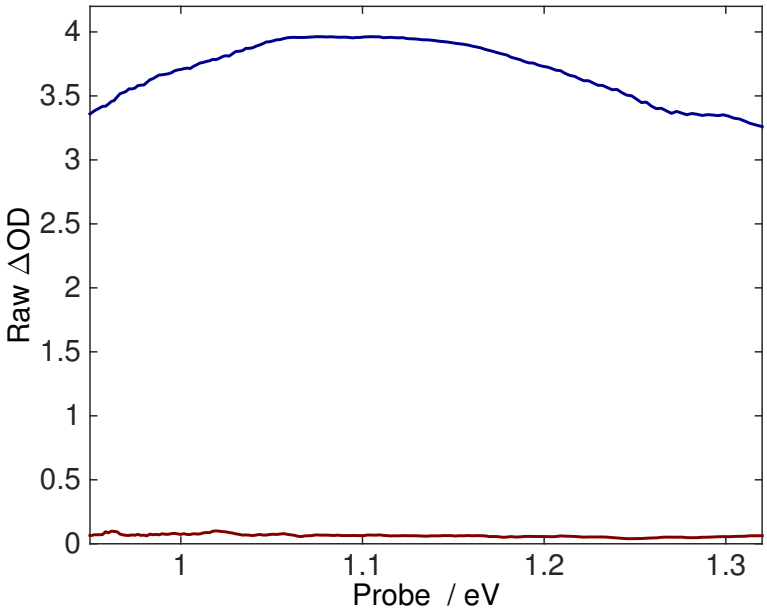

Figure 7.25: Comparison of the near-IR transient absorptions at 10 ps between Bu_4N^+ I^- in $[Py^+_{1,4}][NTf^-_2]$ and neat $[Py^+_{1,4}][NTf^-_2]$, both with a pulse energy of 105 nJ.

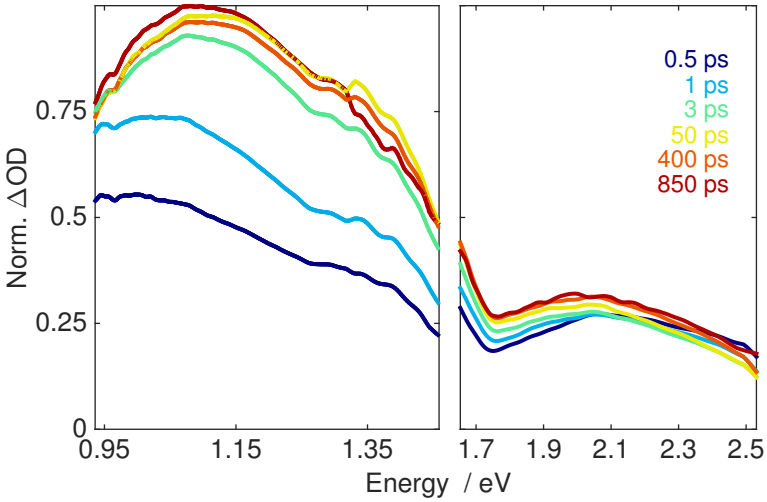

Figure 7.26: Transient absorptions in the near-IR and VIS regions produced by the 6.2 eV excitation of Bu_4N^+ I^- in $[Py^+_{1,4}][NTf^-_2]$.

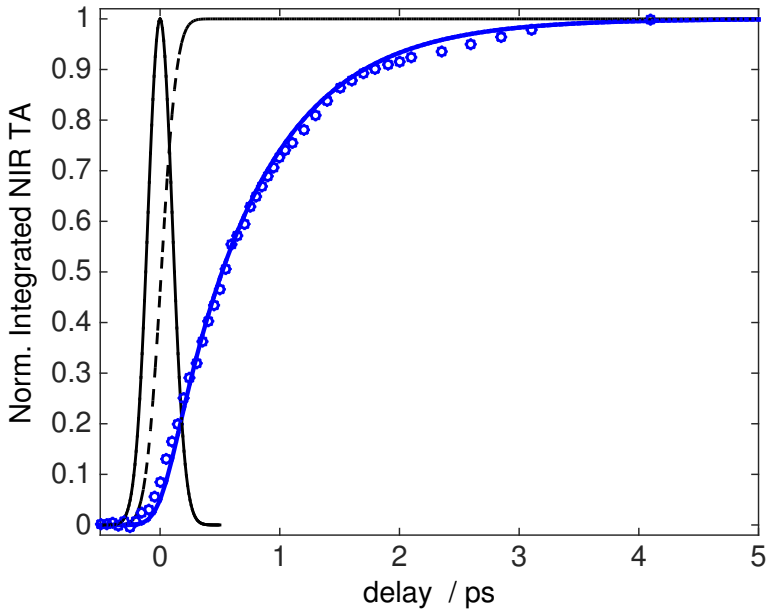

Figure 7.27: Rise of near-IR signal integrated between 0.97–1.27 eV for Bu_4N^+ I^- in $[Py^+_{1,4}][NTf^-_2]$ after 6.2 eV excitation. The Trace is fit to a single exponential rise up to 5 ps, which is convoluted over the IRF, shown in solid black. The dashed thin black line is the convolution of a step function over the IRF.

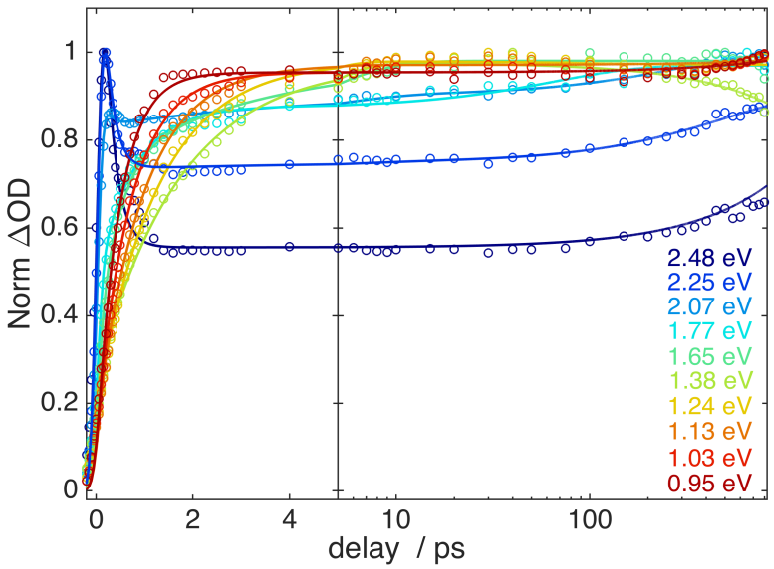

Figure 7.28: Single color kinetic traces for Bu_4N^+ I^- in $[Py^+_{1,4}][NTf^-_2]$ after 6.2 eV excitation. The data is fit to either a 2 or 3 sequential step scheme

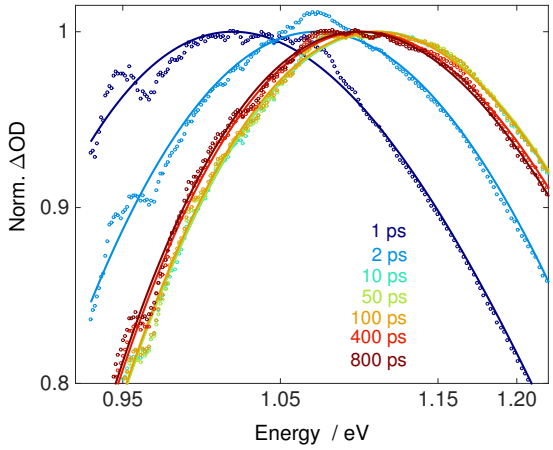

Figure 7.29: Normalized transient absorptions in the near-IR following the 6.2 eV excitation of each of the I solution in $[Py^{+}_{1,4}][NTf^{-}_{2}]$. The circles are experimental data and the solid lines are a 3rd order polynomial fit to the TA.

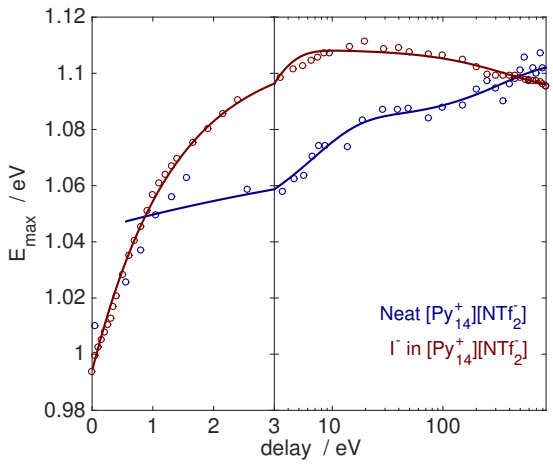

Figure 7.30: Evolution of E_{max} from the cubic fits to the near-IR TA for the I^{-} solution in $[Py^{+}_{1,4}][NTf^{-}_{2}]$ (red), and from the neat $[Py^{+}_{1,4}][NTf^{-}_{2}]$ liquid (blue) for comparison.